A NEUTRON SCATTERING INVESTIGATION OF URANIUM SELENIDE

by

© KAREN M. HUGHES

A Thesis
Submitted to the Faculty of Graduate Studies
in Partial Fulfilment of the Requirements
for the Degree
Doctor of Philosophy

McMaster University
September 1988

A NEUTRON SCATTERING INVESTIGATION OF URANIUM SELENIDE

DOCTOR OF PHILOSOPHY (1988) (Physics)

McMASTER UNIVERSITY
Hamilton, Ontario

TITLE: A Neutron Scattering Investigation of Uranium Selenide

AUTHOR: Karen M. Hughes, M.Sc. (McMaster University)

SUPERVISOR: Professor M.F. Collins

NUMBER OF PAGES: xii, 138

ABSTRACT

US, USe, and UTe form a series of rocksalt structure ferromagnets which exhibit unusual magnetic properties. At high temperatures all three compounds are paramagnetic, and exhibit local-moment-like behaviour. At low temperatures, however, only UTe exhibits an excitation spectrum which is characteristic of a local moment system. In US a broad continuum of magnetic response more akin to what is observed in an itinerant magnet is found. In this work, we focus on the intermediate member of the series, USe.

We have performed a detailed inelastic neutron scattering study of the excitations in the low temperature ferromagnetic phase of USe. A magnetic excitation branch is observed which arises from an extremely large zone centre anisotropy gap (≈ 10 THz) and disperses quadratically at small q. The spectrum is unusual in a number of respects. At the zone centre, the excitation appears as a well-defined peak in the inelastic spectrum but with an intrinsic width (≈ 3 THz). At larger q, the scattering weakens and broadens appreciably. Measurements on a single domain sample have shown that the scattering is unpolarized, i.e. it contains (approximately) equal amounts of transverse and longitudinal response.

We have attempted to describe, as far as possible, the behaviour of the chalcogenides using a localized electron model of the uranium ion. The Hund's rule ground state of the uranium ion is perturbed by a Hamiltonian which includes the effect of a cubic crystal field, exchange and quadrupolar interaction, and magnetoelastic coupling. With this model it is possible to reproduce a number of the magnetic and elastic observables in the UX compounds.

Finally, the ferromagnetic phase transition has been examined using critical neutron scattering techniques. The temperature dependence of the inverse correlation length and static susceptibility have been investigated and found to exhibit the characteristic power law behaviour of a critical phase transition. The critical exponents extracted from this measurement agree reasonably well with those of the three-dimensional Heisenberg model. The order parameter, however, varies in an unusual way: the onset of long range order occurs roughly 5 K above the critical temperature. This behaviour may be linked to the presence of large quadrupolar and magnetoelastic effects in the system.

ACKNOWLEDGEMENTS

I would like to thank my research supervisor Malcolm Collins, for his assistance, his support, and his friendship during the years of this work. This same thanks I would extend to Tom Holden and Bill Buyers of NSSP Branch, Chalk River.

Many thanks to Mel Potter, Don Tennant, Harold Nieman, Gord Tapp, Ron Donaberger, Alan Hewitt, and Peter Moss, for their much needed and extremely capable technical assistance.

I would also like to extend my warmest thanks to the NSSP branch and to the many people who, in my mind, will always be a part of that group; Eric Svensson, Brian Powell, Peter Martel, John Root, Zin Tun, Gerald Dolling, Soo Kim, Annemarie VanDine, Hong Lin, Rose Morelli, Rose Mokra, Mike Hogan, Peter Gerlach, Martin Dove, Paul du Plessis, Jenny Jackman, Ron Deal, Bruce Torrie, Doug Hallman, Jan Genossar, and Robin Armstrong.

Special thanks to Bruce Gaulin.

I would like to thank Annemarie VanDine for her patience and expertise in preparing this thesis.

My thanks to Atomic Energy of Canada Limited for use of their equipment and facilities.

I would like to acknowledge financial assistance from McMaster University and from the Natural Sciences and Engineering Research Council of Canada.

TABLE OF CONTENTS

Page

Chapter 1: Introduction

1.1 General Introduction 1

1.2 UX Compounds 3

1.3 Electronic Ground State 4

1.4 UX Spin Dyanamics 8

1.5 Outline of this Study 9

Chapter 2: Neutron Scattering

2.1 Triple-Axis Spectrometry 11

2.2 Resolution Function 14

Chapter 3: Neutron Scattering Cross Section

3.1 Magnetic Scattering Cross Section 18

3.2 Magnetic Bragg Scattering 21

3.3 Inelastic Magnetic Scattering 21

3.4 Polarization of the Scattering Cross Section 22

3.5 Phonon Scattering 23

Chapter 4: Magnetic Excitations in the Ordered Phase

4.1 Spin Dynamics of Ferromagnets 26

4.2 Details of the Experiment 27

4.3 Zone Centre Response 31

4.4 Dispersion 33

4.5 Calibration 37

4.6 Calculation of $\langle M^2 \rangle$ 42

Page

Chapter 5: Spin Wave Polarization Measurement

5.1 Details of the Experiment 47

5.2 Polarization of the Magnetic Scattering 48

Chapter 6: Analytic Description of the UX Compounds

6.1 Localized Model 58

6.2 The Hamiltonian 58

6.3 The Magnetic Susceptibility in the Paramagnetic Phase 61

6.4 The Quadrupolar Susceptibility in the Paramagnetic Phase 63

6.5 Low Temperature Ordered Phase 64

6.6 f^3 Ground State 65

6.7 f-d Model 71

Chapter 7: Magnetic Critical Scattering in USe

7.1 Critical Phase Transitions 76

7.2 Critical Behaviour of the UX Compounds 79

7.3 Critical Scattering in the Paramagnetic Phase 79

7.4 Critical Behaviour in the Ordered Phase 81

7.5 Details of the Experiment 82

7.6 Resolution Correction 83

7.7 Determination of T_c 87

7.8 Isotropic Nature of the Scattering 90

7.9 Temperature Dependence of the Critical Scattering 92

7.10 Critical Exponents 96

7.11 The Quasi-Elastic Approximation 101

7.12 Order Parameter 101

Page

Chapter 8: Summary

8.1 Excitations in the Ferromagnetic Phase 108

8.2 Local Moment Model 109

8.3 Critical Scattering 110

Bibliography

Appendix A: Hamiltonian of the Localized Model 117

Appendix B: Magnetic Excitations in the Localized Model 125

Appendix C: Scaling and Universality 128

Appendix D: Critical Neutron Scattering 135

LIST OF FIGURES

Page

2.1 Neutron triple-axis spectrometer 13

2.2 Reciprocal space of an fcc lattice in the (hhl) plane 15

3.1 Magnetic form factor of uranium 20

4.1 Rocking curves of nuclear Bragg reflections in the single crystal sample of USe 28

4.2 Typical data set with measured background 30

4.3 Inelastic response of the (220) and (440) zone centres 32

4.4 Inelastic zone centre response of the uranium chalcogenides 34

4.5 (a) Wave-vector dependence of the inelastic response in USe 35

(b) 36

4.6 Dispersion curve of magnetic excitations in USe in the (ζζζ) direction 38

4.7 Typical phonon groups 41

4.8 Wave-vector dependence of the damped harmonic oscillator parameters 44

5.1 Formation of a single domain sample in the presence of an external magnetic field as seen through the temperature dependence of the (111) and ($11\bar{1}$) Bragg peaks 49

5.2 The geometry of the polarization measurement 50

5.3 Typical data set with measured background 52

Page

5.4 Inelastic response at the (220) zone centre compared with the equivalent measurement from the previous experiment 53

5.5 Constant-Q scans at the zone centres (222) and $(22\bar{2})$ in a single domain sample 54

5.6 Constant-Q scans at the zone centres (222) and $(22\bar{2})$ in a multidomain configuration. 56

6.1 Energy splitting of the $\Gamma_8^{(2)}$ quartet by the mean exchange field 67

6.2 Energy splitting of the $\Gamma_8^{(2)}$ quarter by the mean quadrupolar field 68

6.3 Fit of the f-d electronic damping model to the zone centre response in USe 74

7.1 Geometry of the critical scattering measurements 84

7.2 The measured resolution ellipse in the scattering plane 86

7.3 The intensity of the (111) Bragg peak as a function of temperature in the critical regime. 88

7.4 The intensity of the critical scattering (at wave vectors slightly offset form q=0) in the critical regime 89

7.5 Isotropic critical scattering at 179.6 K 91

7.6 (a) Evolution of the critical scattering (along (111)T) as a function of temperature 93

(b) 94

7.7 Temperature dependence of the static susceptibility and inverse correlation length in the critical regime 95

Page

7.8 Log-Log plots of static susceptibility and inverse correlation length as a function of reduced temperature for $T_c = 169.5$ K 97

7.9 Log-Log plots of static susceptibility and inverse correlation length as a function of reduced temperature for $T_c = 170.5$ K 98

7.10 Critical exponents ν, γ, and β as a function of critical temperature 100

7.11 Wave-vector dependence of the inelastic scattering at 182 K 102

7.12 q=0 response at 176 K and 178 K 103

7.13 Fit to the order parameter assuming a distribution of critical temperatures 107

LIST OF TABLES

Page

1.1 Magnetic properties of UX compounds 6

4.1 Phonon cross sections and intensities used in the calibration of the magnetic scattering 42

6.1 Comparison of the UX observables to those predicted by the localized electron model 69

7.1 Static susceptibility and inverse correlation length at 179.6 K showing the isotropic nature of the scattering 92

CHAPTER 1: INTRODUCTION

1.1 General Introduction

Uranium, and its 4f equivalent cerium, are the first magnetic members of the actinide and lanthanide series respectively. They have provided a series of new and fascinating magnetic systems, the distinguishing feature of which seems to be that the f electrons, which are responsible for their magnetic character, reside in narrow bands at, or near, the Fermi energy (E_F). This underlying structure in the magnetic electron system might be described as intermediate between those of the other well-known magnetic metal systems: the rare-earths and the transition metals. For the most part, the heavy rare-earths are characterized as local moment systems: the magnetic 4f-electrons are well localized at each site, effectively screened from their surroundings by the outer d-electron shells. They form a highly correlated spin state within each ion and interact only indirectly with neighbouring ions via an RKKY interaction through the conduction electrons. This is usually not true of cerium or uranium systems. The f-shell contains a small number of electrons, less tightly bound to the atom in the sense that their wavefunctions extend outside the central core. The f-electron system is then extremely sensitive to its local environment, and is capable of interacting directly with neighbouring ions and conduction electrons. In the transition metals, where the spatial extent of the magnetic electron orbitals is greater still, this interaction leads to the formation of broad 3d bands (several eV wide), and the concept of itinerant magnetism. In uranium and cerium systems, however, on-site spin correlations still play an important role and the ensuing description of the f-electron state is in terms of narrow bands or at times, extremely narrow resonance states.

There are examples of uranium systems in which the localized f-electron picture seems a valid description: UO_2 and UPd_3, for example. However, some of the more novel physical behaviour exhibited by uranium systems arises because the proximity of the f-electron level to the Fermi level makes it possible for the f electrons to 'hop' on and off the site, (or, equivalently, in and out of the conduction band). This is the simple physical picture of a so-called 'mixed valence' system of which cerium is a well-known example. A second and more subtle manifestation of the f-electron-conduction-electron interaction occurs in the heavy-fermion systems. The term 'heavy fermion' arises from the unusually large value of the (linear) electronic specific heat coefficient, γ, which may be interpreted as a large conduction electron effective mass. (In UBe_{13}, for example, the effective mass is approximately 200 times the conventional electron mass (Ott et al, 1983)). Despite their local-moment-like appearance at high temperatures, the heavy fermion systems do not condense into 'ordinary' low temperature magnetic ground states. U_2Zn_{17}, for example, exhibits a Curie-Weiss law susceptibility at high temperatures with an effective paramagnetic moment (μ_{eff}) of about 3 μ_B (Ott et al, 1984); it orders antiferromagnetically at ≈ 10 K but with a strongly suppressed moment of only ≈ 0.8 μ_B (Cox et al, 1986). $CeCu_6$ (μ_{eff} ≈ 2.7) fails to order magnetically, exhibiting instead a large Pauli-like susceptibility at the lowest temperatures (Stewart et al, 1984a; Pop et al, 1974). The low temperature ground state of UPt_3 (μ_{eff} ≈ 2.6) is superconducting (Schneider and Laubschat, 1981; Stewart et al, 1984b).

1.2 UX Compounds

This work focusses on a series of magnetic uranium systems which exhibit the characteristic duality of localized and non-localized electron behaviour. The series consists of materials of the form UX where X is a member of the group 6 (chalcogenide) elements, specifically S, Se, and Te. A second, parallel series of compounds is formed by the group 5 (pnictide) elements, N, P, As, and Sb. These compounds have a rock-salt structure: an fcc lattice with a two atom basis consisting of a uranium atom at (000) and an X atom at (1/2,1/2,1/2). All are paramagnetic at room temperature and magnetically ordered at low temperatures: the chalcogenides order ferromagnetically and the pnictides antiferromagnetically.

The phase transition in the chalcogenides was first posited from an anomaly in the specific heat measurements of USe and US (Takahashi, 1965, and Westrum, 1968). The magnetic nature of the phase transition became apparent from measurements on a powder sample by Chechernikov et al (1968). These measurements demonstrated an increase in the bulk magnetization consistent with the onset of ferromagnetism, and approximately Curie-Weiss law behaviour of the susceptibility in the paramagnetic phase.

The magnetization axis for the ferromagnetic ordering is <111>. Single crystal measurements on US (Tillwick and du Plessis, 1976), USe (Busch and Vogt, 1978) and UTe (Vogt, 1980) show that an extremely strong anisotropy confines the spins to this easy axis. The anisotropy is estimated as 3000 kOe in US (du Plessis, 1986) and 1000 kOe in UTe.

The ferromagnetic transition is accompanied by a large rhombohedral distortion along the easy axis. Ultrasonic and strain measurements (du Plessis and Tillwick, 1979, Nuenschwander et al, 1986) show that as the critical temperature (T_c) is approached, there is a softening in the bulk elastic constants. Below T_c, Marples (1970) has measured the magnitude of the distortion as a function of temperature in US and USe. At 4 K the distortion is largest in US and smallest in UTe.

1.3 Electronic Ground State

The electronic ground state of the uranium ion in most compounds is unknown. Only in two cases, UO_2 (Frazer et al, 1965, Cowley and Dolling, 1968) and UPd_3 (Buyers et al, 1980) is there evidence for a specific ground state configuration (a localized $5f^2$ state in both). In a simple ionic bonding picture, the ground state electronic configuration of UX would result from the uranium atom donating electrons, as needed, to complete the valence shell of the ligand X atom. A uranium ion configuration of $5f^3$ is predicted in the pnictides, and $5f^3 6d^1$ in the chalcogenides. Since the uranium ion would be left with the same electronic ground state in each of the chalcogenides (or pnictides), it might be expected that the magnetic behaviour of these compounds would be very similar, with differences ascribed to changes in the size of the X site. This is in fact observed. Table 1.1 summarizes the static magnetic properties of the UX series. The similarity among the chalcogenides is apparent. The situation in the pnictides is more complicated because of the different antiferromagnetic ordered structures. There is a definite correlation, within each group, between the magnetic properties and the lattice constant. As the lattice constant increases, the ordering temperature decreases in the chalcogenides and increases in the pnictides. Furthermore, the largest moments occur in the compounds with the largest X sites, and the smallest moments, in those with the smallest X site.

The suppression of magnetic character with decreasing inter-atomic distance is not unusual in cerium and uranium systems. It was first recognized by Hill (1970) that there was a strong correlation between the lattice parameter and the low temperature ground state of uranium systems: a large U-U separation led to a magnetic ground state and small U-U separation, to a metallic (superconducting) ground state. An example of the effect of decreasing inter-atomic distance on f-electron behaviour can be found in cerium metal (Coqblin, 1971). The nominal electronic ground state of cerium is $4f^1$, corresponding to a valence of 3^+. At standard temperature and pressure, cerium is a paramagnet with a moment of $\approx 2.5\mu_B$. At ≈ 7 kbar however, cerium undergoes a first order transition from its γ-phase to its α-phase in which the structure remains fcc but the lattice parameter decreases by ≈ 6%. α-cerium is a Pauli paramagnet with an 'intermediate' valence of $\approx 3.5^+$.

Table 1.1 The static magnetic properties of the UX compounds.

UX	lattice parameter (Å)	ordered structure	ordering temp (K)	paramagnetic moment (μ_B)	ordered moment (μ_B)
US	5.49	F <111>	180.	2.25	1.70
USe	5.74	F <111>	172.	2.50	2.0
UTe	6.18	F <111>	102.	2.60	2.25
UN	4.89	AF type I	49.5	2.50	0.75
UAs	5.78	AF 2q	126.	3.40	1.95
USb	6.18	AF 3q	217.	3.85	2.82

At roughly 50 kbar, cerium undergoes another phase transition to the hexagonal α'-phase which has a valence of 4^+, (i.e. a non-magnetic $4f^0$ configuration) with a low temperature superconducting ground state.

Certain features of the underlying band structure of the UX compounds have emerged. Rudigier et al (1985) have performed low temperature specific heat measurements on single crystal UX compounds and observed values of γ which are approximately 4 to 10 times larger than those obtained in the isostructural, but non-magnetic, LaX or ThX compounds. This is attributed to the presence of an f-electron density of states at the Fermi energy. The systematic variation of γ suggests that the density of f-electron states at the Fermi level decreases in the chalcogenides and increases in the pnictides, with increasing lattice parameter.

For the most part, photoemission and optical measurements seem to support this result (see for example Baer, 1980; Greuter et al, 1980; Shoenes, 1980). Based on optical measurements Shoenes (1980) has proposed an electronic structure of the UX compounds which consists of a narrow (≈ 1 eV) f-electron density of states just above E_F overlapped by a much broader d-electron band (of width ≈ 6 eV), and well-separated from the ligand p-band (which is primarily responsible for bonding). The f-d interaction produces a dip in the d-density of states in the vicinity of the maximum in the f-density of states giving rise to a peak in the occupied d-electron density just below E_F. Between the pnictides and the chalcogenides the main difference is in the position of the p-band which is ≈ 3 eV below E_F in the pnictides and ≈ 4 eV below in the chalcogenides. Within each group, there is an overall narrowing of the band structure as the lattice constant increases. This picture is consistent with the photoemission measurements on US and UN (Erbudak and Keller, 1979; Norton et al, 1980) and with the calculations of Brooks and Glotzel (1980) which specifically consider the effect of f-p hybridization on the f-electron bandwidth. However, the photoemission measurements of Riehl et al (1982) suggest that there are significant differences between the pnictide and chalcogenide band structures around E_F. Measurements on UTe suggest that the 5f level is 0.75 eV below the Fermi level, leading to a quasi-localized 3-δ f-electron state.

Spin polarized photoemission measurements indicate that in the chalcogenides the d-electron moment opposes the f-electron moment (Erbudak et al, 1979). This is consistent with the observation of Wedgwood and Kuznietz (1972) that the ordered moment observed in magnetization is always smaller than the (primarily) f-electron moment observed in neutron scattering measurements.

1.4 UX Spin Dynamics

The spin dynamics in the low temperature ordered phase have been investigated by inelastic neutron scattering. 'Conventional' spin wave excitations, that is sharp resolution-limited peaks in the inelastic spectrum, are only observed in the compounds with the largest lattice constants, UTe and USb. In US, UN, and UAs, no well-defined peaks appear, and only broad continuums of inelastic magnetic scattering exist, even at temperatures well below the magnetic phase transition.

In US and UN, the response is centered at finite frequency, while in UAs, the continuum is centered around zero frequency.

Even in USb and UTe, the response is not entirely conventional. In USb, a second 'optic' branch of magnetic character is observed, in which the excitations are broad and not well-defined in energy. Underlying the scattering from these two branches is again an extended continuum of magnetic response. In UTe, the spin wave branch observed by Buyers et al (1980) shows a rather large zone centre anisotropy gap, and quadratic dispersion. The excitations however, are only visible at small q and cannot be followed to the zone boundary. The search for continuum scattering has not been carried out in UTe.

1.5 Outline of this Study

This work is an investigation of the magnetic behaviour of USe, the intermediate member of the chalcogenide series. In Chapters 4 and 5, inelastic neutron scattering measurements on a single crystal sample in the low temperature ferromagnetic phase are presented. Measurements performed on a multidomain sample establish the magnetic origin of the observed excitations and examine the wave-vector dependence. The polarization of the response is determined in a second set of measurements performed on a single domain sample.

The low temperature response is characterized as being 'intermediate' between that of US and UTe, in the sense that well-defined, but not resolution-limited, peaks are observed in the energy spectrum at small q. Well away from the zone centre, only a broad continuum of magnetic scattering is observed. The single domain experiment shows that, at the zone centre at least, the scattering is unpolarized.

Although it is clear that the dynamic response cannot be described within a simple local moment picture, Jackman (1983) has had considerable success in describing, quantitatively, the static magnetic properties of the chalcogenide compounds within such a model. In Chapter 6 Jackman's calculation, which considers crystal field and exchange effects, is extended to include magnetoelastic and quadrupolar interactions. With this model it is possible to reproduce the static magnetic properties as well as certain features of the bulk elastic and dynamic magnetic response. An electronic damping model is discussed in connection with the broadened response.

Chapter 7 is a study of the magnetic phase transition in USe. Critical neutron scattering techniques have been used to probe the temperature dependence of the static susceptibility and the correlation length in the critical regime. These are found to be consistent with the power law forms predicted by scaling. The behaviour of the order parameter is found to be unusual in that the onset of long range order occurs above the apparent critical temperature. The possible origin of this effect is discussed.

CHAPTER 2: NEUTRON SCATTERING

Neutron scattering is a very powerful technique for studying condensed matter, and in particular, for studying magnetic properties. Like X-rays, thermal neutrons have wavelengths comparable to interatomic distances and so can be used to probe the structure of matter on that scale. Unlike X-rays, neutrons are very penetrating and so can be used to sample the bulk and not just the surface properties of a material. Furthermore, thermal neutron energies are comparable to lattice excitation energies, and in the process of scattering, measurable amounts of energy can be exchanged between the neutron and the solid. Finally, because a neutron has a magnetic moment, it can interact with magnetic constituents of matter and provide information about magnetic structure and excitations. It is useful to begin with a brief discussion of the principles involved in neutron scattering from a single crystal.

2.1 Triple-Axis Spectrometry

A neutron scattering event consists of a neutron with some wave vector, $\vec{k}$, and energy, E_0, impinging on a sample, exchanging energy and/or momentum with the sample and as a result scattering from the crystal with a new wave vector, $\vec{k}'$, and energy, E'. Such an event is characterized, by two things:

(1) The energy transfer to (or from) the sample, $\Delta E = E_0 - E'$

(2) The wave vector (momentum) transfer, $\vec{Q} = \vec{k} - \vec{k}'$,

determined by the wavelength and direction of incoming/outgoing neutron and the crystal orientation.

These can be determined experimentally using a neutron triple-axis spectrometer.

A schematic of a triple-axis spectrometer is shown in Fig. 2.1. The "white" reactor beam falls onto a monochromator (M), a crystal of known lattice spacing (d_M) and orientation (θ_M), which Bragg reflects neutrons of a specific wavelength, $\lambda = 2d_M \sin\theta_M$, onto the sample. The sample (S) is mounted on a rotating table with its orientation in the scattering plane specified by the angle Ψ. Neutrons scattered from the sample in a particular direction, ϕ, fall onto the analyzer (A), a second monochromating crystal characterized by d_A and θ_A, which Bragg reflects neutrons into the detector (D). It is simple to show that a given configuration of the spectrometer (i.e. θ_M, θ_A, ϕ, Ψ) maps on to a particular scattering event (i.e. E_0, E', $\vec{k}$, $\vec{k}'$).

A systematic way of surveying the energy and wave-vector dependence of the scattering is the constant-Q scan. In such a scan, $\vec{k}$ and $\vec{k}'$ are varied, but only in such a way that $\vec{k} - \vec{k}'$ is not. This allows the energy transfer, ΔE, to be varied, for a fixed wave vector, $\vec{Q}$. This is most easily seen by considering the geometry of the constant-Q scan in the crystal's reciprocal-space.

When dealing with a cubic structure, it is convenient to orient the crystal with a $(1\bar{1}0)$ vector perpendicular to the scattering plane,

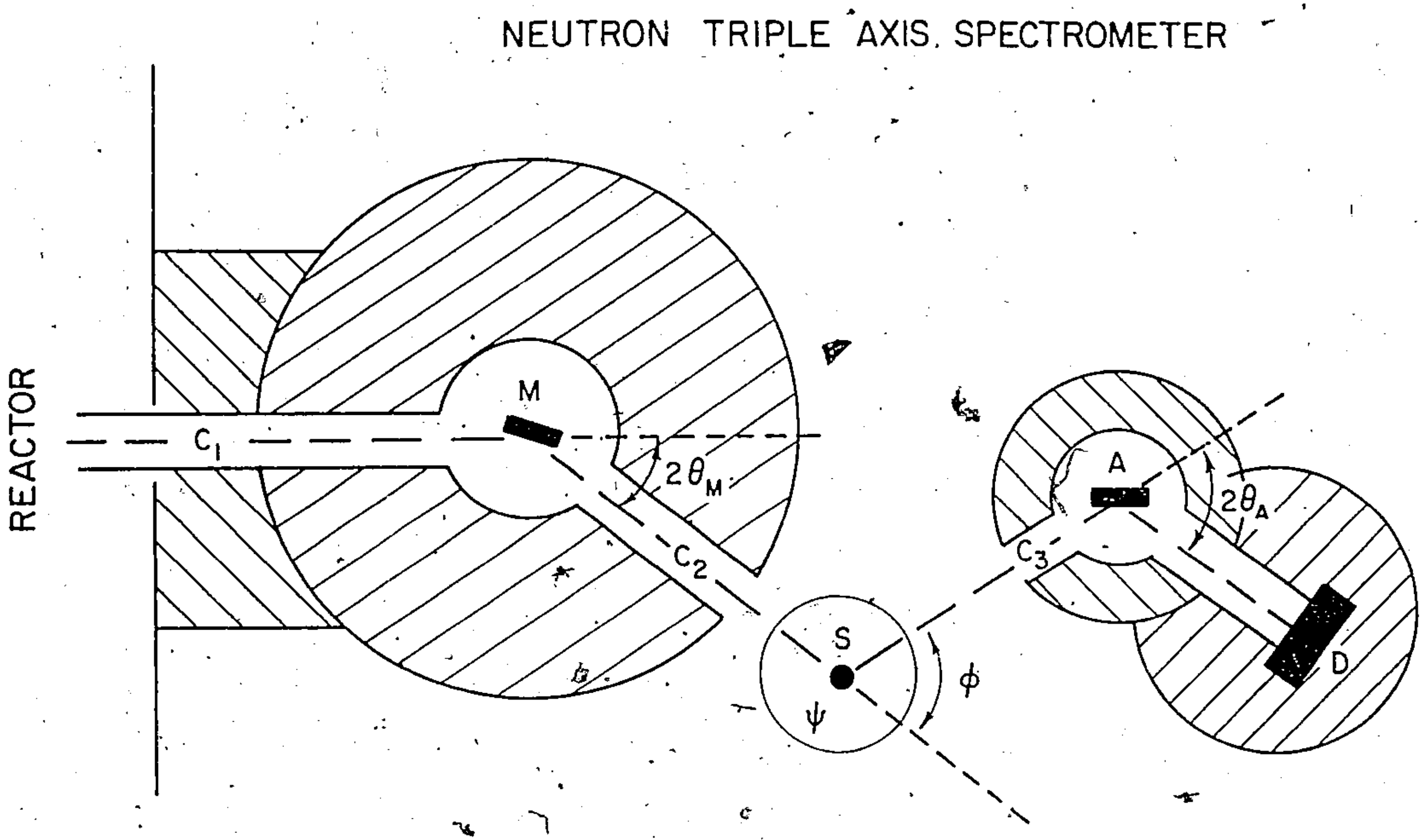

Fig. 2.1 A neutron triple axis spectrometer. Neutrons from the reactor fall onto the monochromator (M) and are Bragg reflected onto the sample (S). Neutrons scattered at an angle ϕ fall onto the analyzer (A) and are Bragg reflected into the detector (D).

since the scattering plane then contains the crystal's three axes of highest symmetry ie. (100), (110), (111). Figure 2.2 shows this plane for an fcc real space lattice (relevant for the UX compounds). It can be seen that the zone centers lie on a face centered rectangular lattice separated by $4\pi/a$ in the (001) direction, and $\sqrt{2}(4\pi/a)$ in the (hh0) direction. The zone boundary, as shown, is a hexagon. The scattering vector, $\vec{Q}$, is the (111) zone boundary (2.5, 2.5, 3.5). The incident and final neutron energies are determined by the lengths of $\vec{k}$ and $\vec{k}'$ respectively. The $\vec{k}$ and $\vec{k}'$ vectors shown correspond to $\Delta E > 0$.

A two-axis spectrometer is a somewhat simpler configuration in which the analyzer is removed (and the angle $2\theta_A$ set to zero). In this case, all neutrons scattered in the direction ϕ are detected, independent of their scattered energy.

Counting is normally done relative to a 'monitor' count. The 'monitor' is a low efficiency fission counter situated between the monochromator and the sample. The sample count is halted after a specified number of counts at the monitor so as to normalize the counting time to a set number of incident neutrons.

The more technical aspects of neutron scattering are discussed in some detail by Bacon (1975).

2.2 Resolution Function

Experimentally, $\vec{Q}$ and ω are never perfectly well-defined. Because the scattering elements have finite mosaic spreads and because collimation tolerates some angular divergence in $\vec{k}$ and $\vec{k}'$, the spectro-

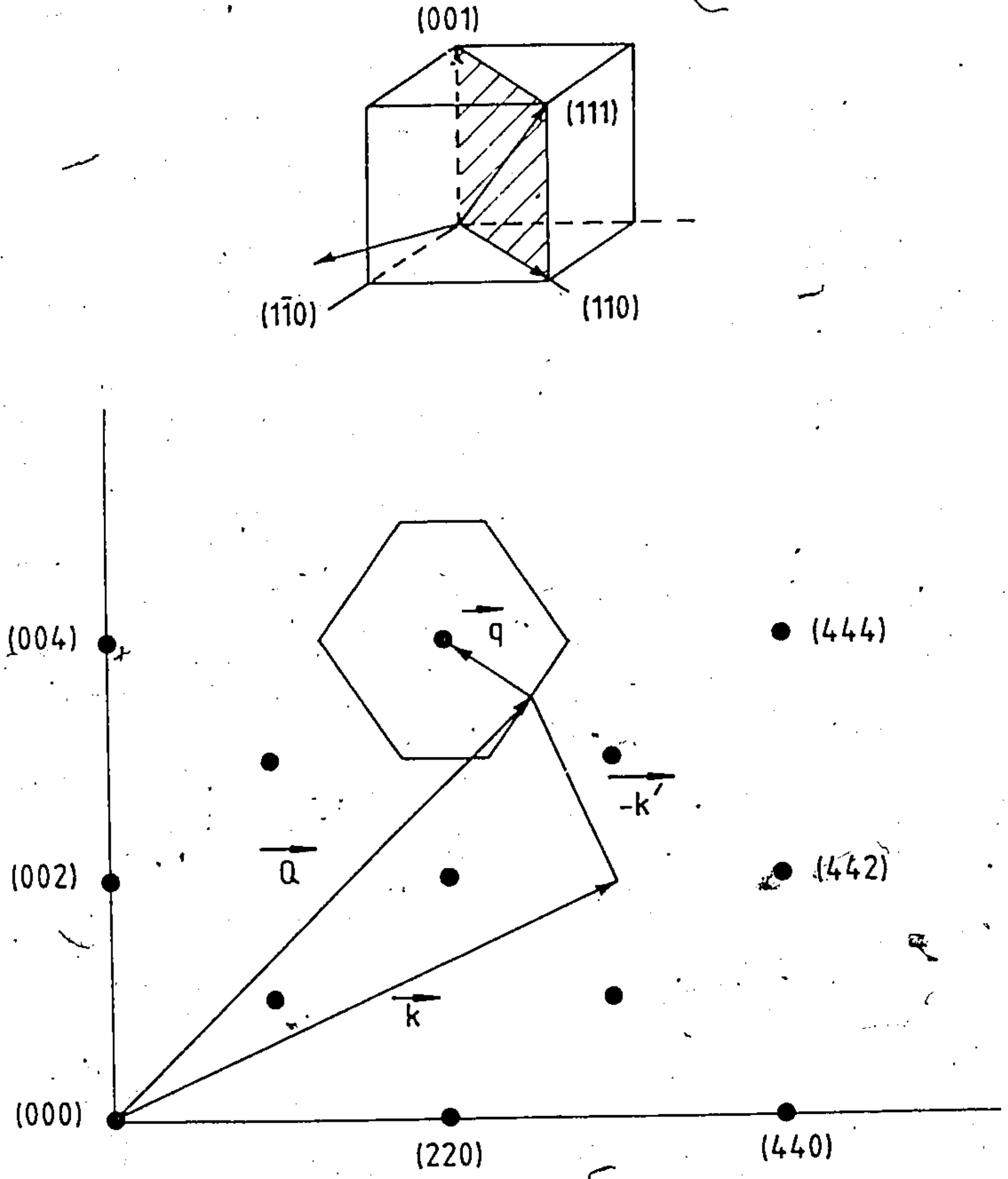

Fig. 2.2 The reciprocal space of an fcc lattice in the (hhl) plane. The zone centres lie on an fcc rectangular lattice. Shown is a typical scattering geometry at a wave vector transfer, Q, of (2.5, 2.5, 3.5). q is the reduced wave vector.

meter will always be sensitive to some range of wave vector and energy transfer around the most probable values. The uncertainties in $\vec{Q}$ and ω are described by the spectrometer resolution function, $R(\vec{Q}_o + \Delta\vec{Q},\ \omega_o + \Delta\omega)$, which measures the probability of the spectrometer registering an event at $(\vec{Q}_o + \Delta\vec{Q},\ \omega_o + \Delta\omega)$, when it is meant to measure an event at $(\vec{Q}_o,\ \omega_o)$.

$R(\vec{Q},\omega)$ is given by

$$R(\vec{Q},\omega) = \int P(\vec{Q},\omega)\ d\vec{k}\ d\vec{k}' \qquad [2.1]$$

where $P(\vec{Q},\omega)$ is the probability of measuring an event at $(\vec{Q},\omega)$ originating from a particular set of $\vec{k}$ and $\vec{k}'$. $P(\vec{Q},\omega)$ is obtained by assuming that the collimators and mosaic spreads produce Gaussian distributions of angular divergences. (For example, the probability of there being a mosaic block at an angle α away from the central block varies as $e^{-(\frac{\alpha}{\eta})^2}$ where η is the mosaic spread of the scattering element). $R(\vec{Q},\omega)$ is then the sum over all paths $(\vec{k},\vec{k}')$ to the point $(\vec{Q},\omega)$.

$R(\vec{Q}_o + \Delta Q, \omega_o + \Delta\omega)$ is functionally described in terms of a resolution ellipse. In general the resolution ellipse is the surface, in 4-dimensional $\vec{Q}$-ω space, which satisfies

$$R(\vec{Q}_o + \Delta\vec{Q}, \omega_o + \Delta\omega) = \frac{1}{2} R(\vec{Q}_o, \omega_o) \qquad [2.2]$$

that is, it is the set of $(\Delta\vec{Q}, \Delta\omega)$ for which the probability of an event is half the probability of the most likely event. For a two-axis measurement, where there is no energy analysis on the scattered side, the surface exists only in Q-space.

The measured intensity of the scattering, $I(\vec{Q}_o,\omega_o)$, is determined by convoluting the intrinsic sample scattering function, $S(\vec{Q},\omega)$, with the resolution function, i.e.

$$I(\vec{Q}_o,\omega_o) = \int d\vec{Q}\, d\omega\, S(\vec{Q}_o + \Delta\vec{Q}, \omega_o + \Delta\omega)\, R(\vec{Q}_o + \Delta\vec{Q}, \omega_o + \Delta\omega) \qquad [2.3]$$

Notice that if $S(\vec{Q},\omega)$ is a δ-function, then the integration returns the resolution function. In principle, a Bragg peak is a δ-function, and so can be used to directly probe the resolution function in the neighbourhood of a reciprocal lattice vector.

Detailed reviews of the formalism required in calculating the resolution function are given by Cooper and Nathans (1967) and Bjerrum Moller and Nielsen (1970).

CHAPTER 3: NEUTRON SCATTERING CROSS SECTION

There are a number of processes that can cause a neutron to be scattered. Bragg reflection is an example of elastic scattering where the scattered neutron has the same kinetic energy as the incident neutron. Neutrons can also be scattered inelastically, in the process of creating or annihilating quanta of energy (such as a phonon) in the scattering system. Because of its magnetic moment, a neutron can also be scattered by nuclear and electronic magnetic moments; here the inelastic scattering involves energy from magnetic excitations such as spin waves. The primary concern of this thesis is the scattering of magnetic origin.

3.1 Magnetic Scattering Cross Section

Consider a system of local moments, $\vec{J}$, on a Bravais lattice. The magnetic scattering cross section for an event at wave vector $\vec{Q}$ and energy $\hbar\omega$, is given by

$$\frac{d^2\sigma}{d\Omega dE'} = \frac{Nk'}{k} \left(\frac{\gamma e^2}{m_e c^2}\right)^2 \left(\tfrac{1}{2}g\right)^2 f^2(Q) e^{-2W(Q)} \sum_{\alpha\beta}(\delta_{\alpha\beta} - \hat{Q}_\alpha \hat{Q}_\beta) \frac{1}{\hbar} S_{\alpha\beta}(\vec{Q},\omega) \qquad [3.1]$$

where

$$S_{\alpha\beta}(\vec{Q},\omega) = \sum_{\vec{\ell}} e^{i\vec{Q}\cdot\vec{\ell}} \frac{1}{2\pi} \int_{-\infty}^{\infty} dt\, e^{-i\omega t} \langle J^\alpha_{\vec{0}}(0)\, J^\beta_{\vec{\ell}}(t)\rangle \qquad [3.2]$$

and γ = neutron gyromagnetic ratio

e = electron charge

m_e = electron mass

c = speed of light

g = Lande splitting factor

(Marshall and Lovesey, 1971, page 234). The important term is the scattering function $S_{\alpha\beta}(Q,\omega)$. $J^{\beta}_{\vec{\ell}}(t)$ is the β component of the angular momentum at site $\vec{\ell}$, at time t. The cross section is essentially the space and time Fourier transform of the two-spin correlation function, $\langle J^{\alpha}_{\vec{0}}(0)J^{\beta}_{\vec{\ell}}(t)\rangle$.

$\hat{Q}_{\alpha}$ is the component of $\vec{Q}/|Q|$ along the axis $\hat{\alpha}$. $(\delta_{\alpha\beta} - \hat{Q}_{\alpha}\hat{Q}_{\beta})$ is strictly a geometric factor which limits the cross section to examining the components of spin perpendicular to $\vec{Q}$. This term is important in determining the magnitude and polarization of the scattering (Sec. 3.4)

$f^2(Q)$ is the magnetic form factor. It is the Fourier transform of the spatial distribution of the magnetic electrons at the magnetic site (normalized to unity at Q=0). A plot of $f^2(Q)$ versus Q for uranium appears in Fig. 3.1. It can be seen that the form factor falls off sharply with increasing Q so that the magnetic cross section is largest at small Q.

$e^{-2W(Q)}$ is the Debye-Waller factor. This factor accounts for the fact that the scattering nuclei are not pinned to the lattice sites, but vibrate around their equilibrium positions. This results in a decrease of the coherent scattering intensity. For a crystal with cubic symmetry,

$$2W(Q) = \frac{1}{3} Q^2 \langle u^2 \rangle \qquad [3.3]$$

where $\langle u^2 \rangle$ is the mean square displacement of the atom. The displacement is temperature dependent; its magnitude can be determined experimentally from the intensity of nuclear Bragg peaks.

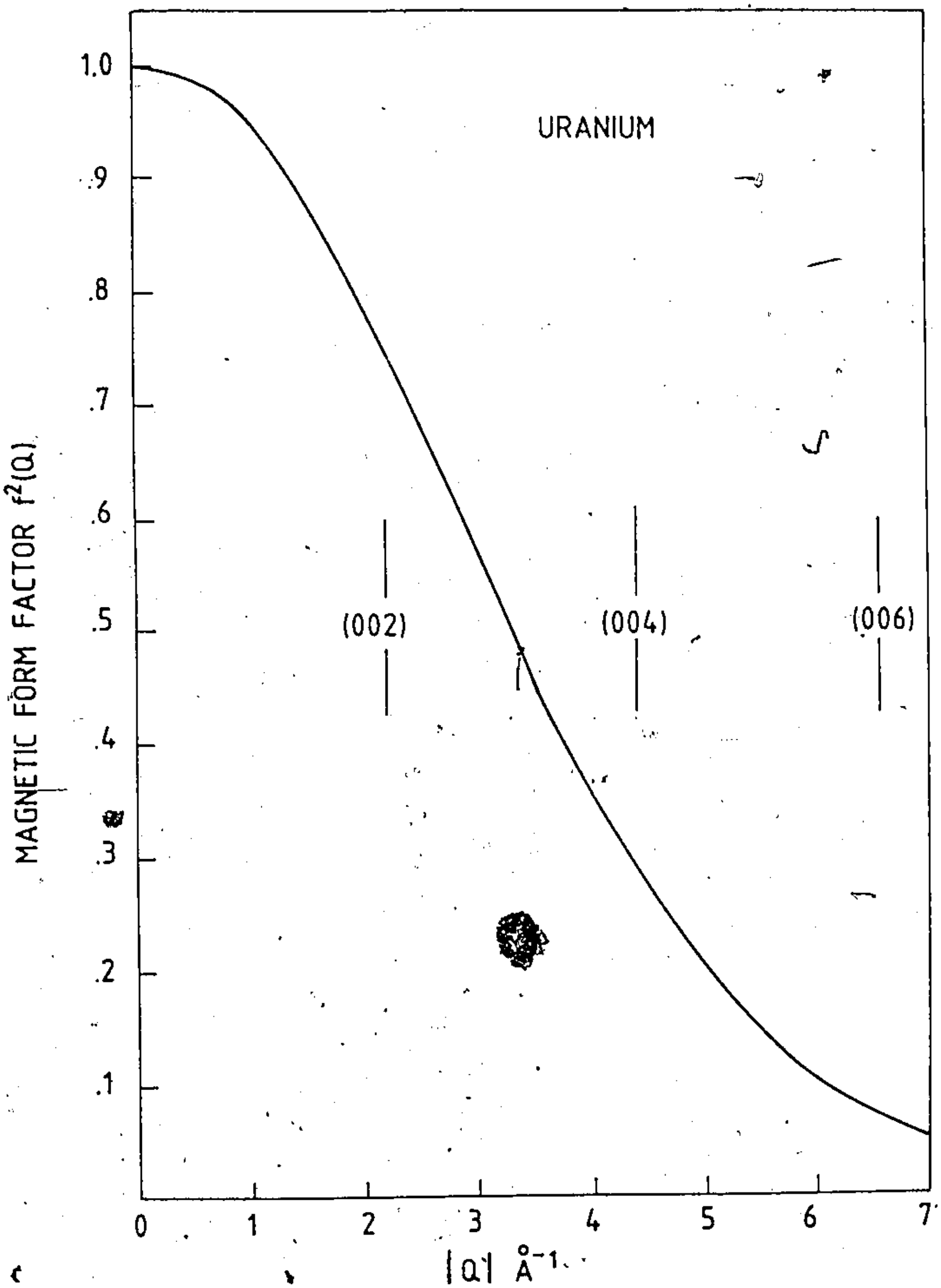

Fig. 3.1 The magnetic form factor of uranium (compiled from the measurements of Wedgwood (1972), Curry (1965), and Lander et al. (1976)).

3.2 Magnetic Bragg Scattering

The cross section for magnetic Bragg scattering is obtained from Eq. [3.1] by considering the time averaged correlation function, i.e.

$$\langle J^{\alpha}_{\vec{0}}(0)\; J^{\beta}_{\vec{\ell}}(t)\rangle \rightarrow \langle J^{\alpha}_{\vec{0}}\rangle\,\langle J^{\beta}_{\vec{\ell}}\rangle \qquad [3.4]$$

The temporal Fourier transform reduces to a δ-function in ω which can be eliminated by integration over energy. In the case of a ferromagnet with ordering direction z,

$$\begin{aligned} &\langle J^{x}\rangle = \langle J^{y}\rangle = 0 \\ \text{and} \quad &\langle J^{z}_{\vec{\ell}}\rangle = \langle J^{z}_{\vec{0}}\rangle = \langle J^{z}\rangle \end{aligned} \qquad [3.5]$$

The elastic scattering cross section reduces to

$$\frac{d\sigma}{d\Omega} = \frac{Nk'}{k}\left(\frac{\gamma e^{2}}{m_{e}c^{2}}\right)^{2}\left(\tfrac{1}{2}g\right)^{2} f^{2}(Q)\, e^{-2W(Q)}\,(1-Q_{z}^{2})\,\langle J^{z}\rangle^{2}\left\{\frac{(2\pi)^{3}}{V}\sum_{\vec{\Gamma}}\delta(\vec{Q}-\vec{\Gamma})\right\} \qquad [3.6]$$

where $\vec{\Gamma}$ is a magnetic reciprocal lattice vector. In a ferromagnet, the magnetic reciprocal lattice coincides with the nuclear reciprocal lattice, that is, both the nuclear and magnetic Bragg peaks occur at $q = 0$.

Notice that owing to the geometric factor, magnetic Bragg scattering cannot be observed at any point $\vec{\Gamma}$ which is along the magnetization direction, z.

3.3 Inelastic Magnetic Scattering Cross Section

In order to examine the inelastic magnetic cross section, it is convenient to rewrite Eq. [3.1] in terms of the generalized susceptibility, $\chi(\vec{q},\omega)$. This generalized susceptibility gives the response of the system to an applied magnetic field of spatial wave vector $\vec{q}$ and frequency ω. It is the quantity of physical importance in the system, with the real part (χ') giving the in-phase response and the imaginary part (χ'') giving the out-of-phase response. $\chi''_{\alpha\beta}(\vec{q},\omega)$ is related to $S_{\alpha\beta}(\vec{q},\omega)$ by

$$S_{\alpha\beta}(\vec{q},\omega) = \frac{1}{\pi}\ \frac{\hbar}{(g\mu_B)^2}\ \frac{1}{(1-e^{-\beta\hbar\omega})}\ \chi''_{\alpha\beta}(\vec{q},\omega) \qquad [3.7]$$

Substituting into Eq. [3.1], the cross section becomes

$$\frac{d^2\sigma}{d\Omega dE'} = \frac{Nk'}{k}\left(\frac{\gamma e^2}{2m_e c^2}\right)^2 \frac{1}{\pi\mu_B^2}\ f^2(Q)e^{-2W(Q)}\ \frac{1}{(1-e^{-\beta\hbar\omega})}\ \sum_{\alpha\beta}(\delta_{\alpha\beta} - \hat{Q}_\alpha\hat{Q}_\beta)\ \chi''_{\alpha\beta}(\vec{q},\omega) \qquad [3.8]$$

For a system in which J^z is conserved, (eg. Heisenberg ferromagnet) only terms in which $\alpha = \beta$ survive, and, assuming that the transverse components are equal, i.e. $\chi''_{xx} = \chi''_{yy}$, Eq. [3.4] can be rewritten as

$$\frac{d^2\sigma}{d\Omega dE'} = \frac{Nk'}{k}\left(\frac{\gamma e^2}{2m_e c^2}\right)^2 \frac{1}{\pi\mu_B^2}\ f^2(Q)e^{-2W(Q)} \times \qquad [3.9]$$

$$\frac{1}{(1-e^{-\beta\hbar\omega})}\ [(1 - \hat{Q}_z^2)\ \chi''_{zz}(\vec{q},\omega) + (1 + \hat{Q}_z^2)\ \chi''_{xx}(\vec{q},\omega)]$$

3.4 Polarization Dependence of the Scattering Cross Section

It is possible, under some circumstances, to distinguish between scattering which arises from the longitudinal component of the dynamic susceptibility, χ''_{zz}, and that which arises from the transverse component, χ''_{xx}. The separation relies on the observation that the susceptibilities are a function of reduced wave vector, $\vec{q}$, whereas the geometric factors in the cross section are a function of the wave vector transfer, $\vec{Q}$. Thus if two wave vectors, $\vec{Q}_1$ and $\vec{Q}_2$, correspond to the same $\vec{q}$, the susceptibilities will be the same at both wave vectors, but their relative weights in the cross section need not be.

Consider, for example, a sample with a single ferromagnetic domain. (The magnetization axis is taken to be $\hat{z}$.) If $\vec{Q}$ is parallel to the magnetization direction ($\hat{Q}_z = 1$), only the transverse component appears in the cross section, i.e.

$$\frac{d^2\sigma}{d\Omega dE'} \propto 2\chi''_{xx}(\vec{q},\omega) \qquad [3.10]$$

If $\vec{Q}$ is perpendicular to the magnetization direction ($\hat{Q}_z = 0$), both transverse and longitudinal components will appear with equal weight, i.e.

$$\frac{d^2\sigma}{d\Omega dE'} \propto \chi''_{zz}(\vec{q},\omega) + \chi''_{xx}(\vec{q},\omega) \qquad [3.11]$$

This type of polarization analysis is not possible in a multidomain sample where the magnetization axis is not unique and the cross section must be domain averaged. For the uranium chalcogenides, with a <111> easy axis, there are 4 equivalent directions, and in the multidomain sample the cross section becomes

$$\frac{d^2\sigma}{d\Omega dE'} \propto \frac{1}{3}\,(\chi''_{zz}(\vec{q},\omega) + 2\,\chi''_{xx}(\vec{q},\omega)) \qquad [3.12]$$

Notice that the weight of transverse to longitudinal response is fixed and depends on $\vec{q}$ rather than $\vec{Q}$.

3.5 Phonon Scattering Cross Section

Although the magnetic scattering is of primary interest in this work, there are other processes, particularly one and two-phonon processes, which can contribute substantially to the scattering. The coherent scattering cross section for the creation of a phonon with (reduced) wave vector $\vec{q}$, from phonon branch j, is given by

$$\left(\frac{d^2\sigma}{d\Omega dE'}\right)_{qj} = \frac{Nk'}{k} \left| \sum_{\ell} \frac{b_\ell}{\sqrt{m_\ell}} \vec{Q}\cdot\vec{e}_\ell(\vec{q},j)\, e^{i\vec{\Gamma}\cdot\vec{r}_\ell}\, e^{-W_\ell(Q)} \right|^2 \frac{\hbar}{2\omega_{qj}} \{1 + n_{qj}\}$$

$$\times\ \delta(\hbar\omega_{qj} - \Delta E)\ \delta(\vec{Q} - \vec{q} - \vec{\Gamma}) \qquad [3.13]$$

$\hbar\omega_{qj}$ is the energy associated with phonon $\vec{q}j$, and $\{1 + n_{qj}\}$ is the population factor.

The main body of the expression is the bracketed term. The subscript, ℓ, refers to an atom in the basis (here a uranium or a selenium atom). m_ℓ is its mass; r_ℓ its position, b_ℓ its scattering length and $\vec{e}_\ell(\vec{q},j)$ the eigenvector for the phonon $\vec{q}j$. The wave vector transfer, $\vec{Q}$, appears dotted into the eigenvector. $\vec{\Gamma}$ is the nearest reciprocal lattice vector to $\vec{Q}$ such that $\vec{\Gamma} - \vec{Q} = \vec{q}$. As before, $e^{-2W_\ell(Q)}$ is the Debye-Waller factor.

It can be seen from Eq. [3.13] that a one-phonon event appears in the cross section as a δ-function at energy $\hbar\omega_{qj}$. In the neutron data, because of the finite resolution, it will appear as a peak centered on ω_{qj}.

It will be remembered that an important part of the Q-dependence in the magnetic cross section comes from $f^2(Q)$ (the magnetic form factor) and this results in a rapid decrease in cross section as $|Q|$ increases. It can be seen from Eq. [3.13] that the phonon cross section essentially varies as Q^2 so that the phonon cross section increases with increasing $|Q|$. This contrast in behaviour will be useful later on when it becomes necessary to separate nuclear from magnetic scattering.

The exact expression for multiphonon scattering is cumbersome. (See, for example, Marshall and Lovesey, 1971, page 94). It is expected that the multiphonon contribution takes the form of a continuum, broadly peaked at zero energy transfer, and that since most of the events will be two-phonon (as opposed to less likely three or more phonon) events, it will have a Q-dependence which goes like Q^4.

CHAPTER 4: MAGNETIC EXCITATIONS IN THE ORDERED PHASE

4.1 Spin Dynamics of Ferromagnets

Magnetic excitations in ferromagnets have been well studied in two limits. The first is the limit in which the electrons responsible for the magnetic behaviour are well localized at each magnetic site. The other is the limit where the magnetic electrons occupy bands with energy near the Fermi energy and so must be considered itinerant to some extent.

The prototype local moment system is the spin-only Heisenberg ferromagnet. The paramagnetic ground state of an ion with spin S is (2S+1)-fold degenerate, but in the ferromagnetic ordered state, the degeneracy is broken by the mean exchange field. The excitation spectrum results from (magnetic dipole) transitions between these mean-field-split single ion levels. A collective excitation (or spin wave) results from the coupling between the excitations on adjacent sites. Because these modes originate from transitions between well-defined energy states, they appear in the susceptibility as a series of delta functions in $\vec{q}$ and ω. At small q the dispersion is quadratic: $E = E_0 + Dq^2$. Here, E_0 is the zone centre anisotropy gap and D is the stiffness constant, proportional to the coupling between the spins.

The simplest model of itinerant magnetism considers a single exchange split electron band which overlaps the Fermi surface. In this model there are, in principle, two types of excitations. At long wavelengths and low energies, it is possible to have collective excitations such as those observed in the local moment systems (Izuyama, Kim and Kubo, 1963). At shorter wavelengths this spin wave branch is expected to merge with a broader spectrum of single electron spin-flip excitations known as Stoner modes. Inelastic neutron scattering measurements of the excitations in transition metal magnets such as Fe and Ni agree, at least qualitatively, with the predictions of this model: well-defined spin wave excitations near the zone centre decay into an inelastic continuum of scattering as q increases (see, for example, Mook 1967, Cooke 1972).

In this chapter, neutron scattering measurements of the spin dynamics in the low temperature ordered phase of USe are described. These measurements, performed on a multidomain sample, establish the magnetic character of the observed excitations and map out their dispersion. Chapter 5 describes measurements made on a single domain sample from which the polarization of the excitations is determined.

4.2 Details of the Experiment

The sample is a small single crystal of USe in the form of a plate (roughly 1 cm on a side) with a total volume of about 0.3 cm^3. (For details of growth and characterization see du Plessis et al, 1982). Sample rocking curves at the reciprocal lattice points (222) and (333) are shown in Fig. 4.1. Calibration of the spectrometer using an aluminum powder suggests a crystal mosaic of less than 0.2°. The sample was mounted in a He cryostat and maintained at a temperature of 4 K throughout these measurements.

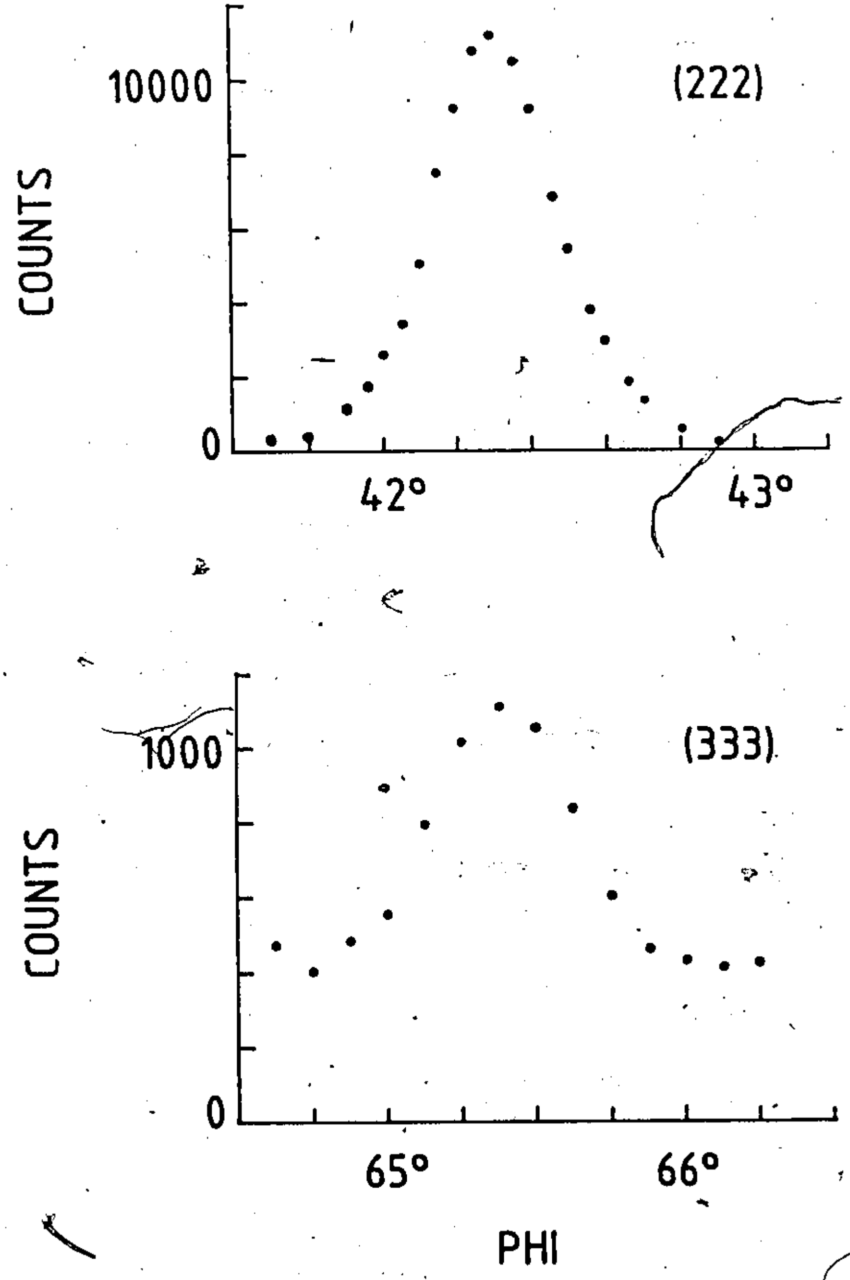

Fig. 4.1 Rocking curves of the nuclear Bragg reflections (222) and (333) in the single crystal sample of USe.

This experiment was carried out on the C5 triple axis spectrometer at the NRU reactor, Chalk River, using a beryllium (002) monochromator and a pyrolytic graphite (002) analyzer. These had mosaics of 0.33° and 0.39° respectively. Collimation before and after the sample gave angular divergences of 0.70° and 0.67° respectively.

Data was collected in the form of constant-Q scans at a fixed scattered-neutron energy of 10 THz. (1 THz = 4.0 mev). This permitted the use of a pyrolytic graphite filter in front of the analyser to reduce higher order contamination.

A fast neutron background measurement was obtained at each point by rotating the analyzer (about 0.5°) so that it was no longer Bragg scattering neutrons into the detector. The scattering from the aluminum sample holder, cryostat, etc. were measured in a separate set of runs by mounting a blank (a duplicate but empty sample holder) in place of the sample.

Figure 4.2 shows a typical data set together with its measured (smoothed) fast neutron background including both blank and fast neutron components. The scattering from the blank is in the form of a weak peak centred at about 5 THz, and is more pronounced at large Q. Its position is consistent with the peak in the aluminum phonon density of states (Gilat and Nicklow, 1966). The high energy 'tail' arises from the increase in the fast neutron background due to the long counting times and smaller scattering angles at large energy transfers.

The measurements were concentrated in the (220) Brillouin zone. (The (111) or (002) zones might seem preferable since $f^2(Q)$ is larger and the phonon contribution smaller; however, at these smaller wave

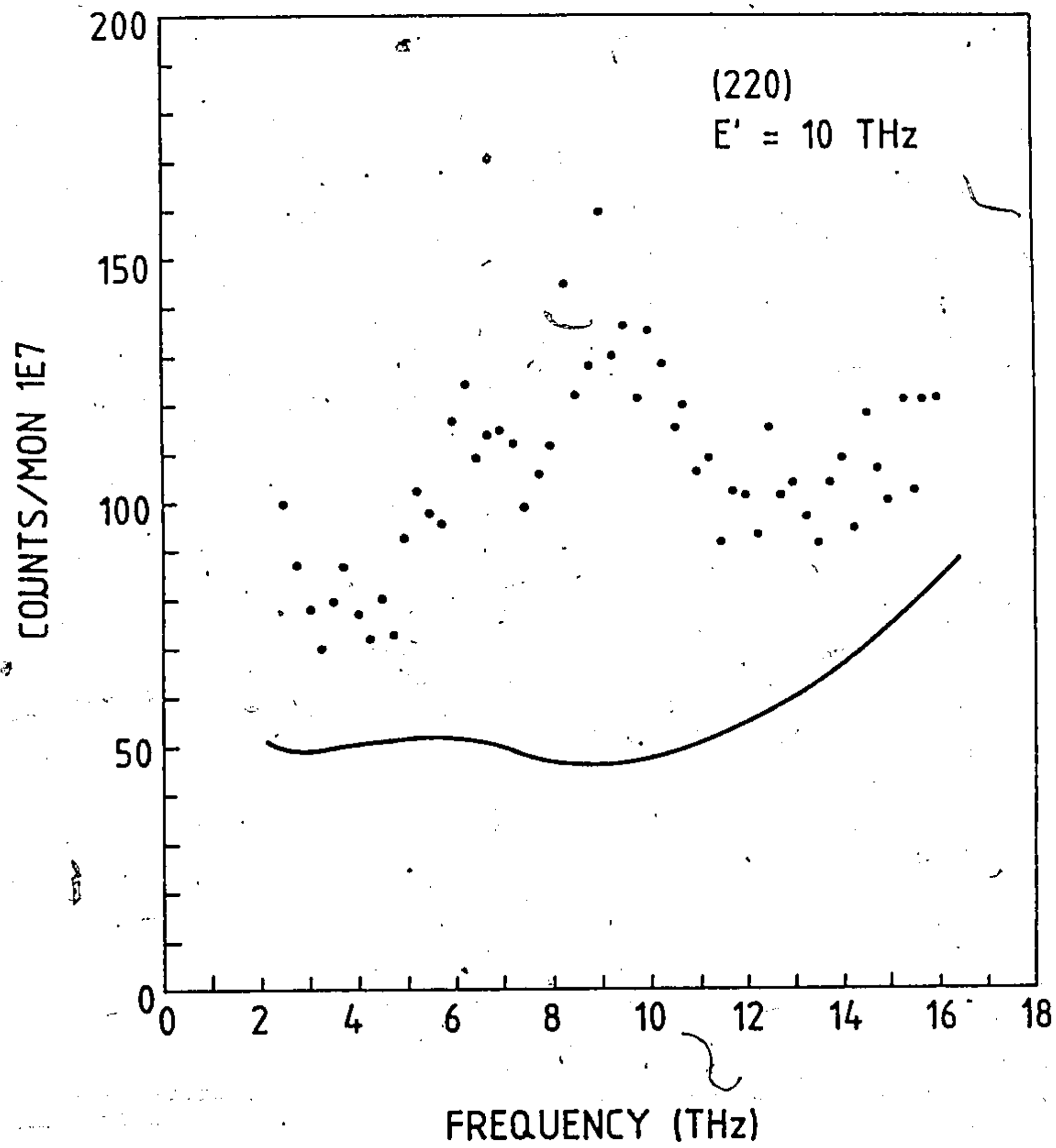

Fig. 4.2 Constant-Q scan of the zone centre (220). The dots are the measured data points. The solid line is the measured (smoothed) background including both the blank and fast neutron components.

vectors, the maximum attainable energy transfer is severely limited by kinematic restrictions). The energy and wave-vector dependence of the scattering were measured in a series of constant-Q scans between the (220) zone centre and the zone boundary at (2.5, 2.5, 2.5), up to energy transfers of 16 THz. Measurements were also made at the corresponding wave vectors in the (440) Brillouin zone in order to distinguish between magnetic and phonon contributions.

4.3 Zone Centre Response

The sample scattering at the zone centres (220) and (440), corrected for the background contribution, are shown in Fig. 4.3. The peak at 6.3 THz, prominent in the (440) data, is identified as the zone centre optic phonon: its position is consistent with previous phonon measurements in USe (Jackman et al, 1986) and the ratio of its intensity between (440) and (220) is roughly consistent with the Q^2 dependence expected for a coherent one-phonon process (Sec. 3.5). The broader feature at 9 THz, clearly visible only at (220), is magnetic in origin. The magnetic form factor reduces the magnetic scattering contribution at (440) by a factor of about 6 compared with (220), completely obscuring the magnetic peak at the larger wave vector.

Assuming that the scattering, away from the one-phonon peak, is comprised of only a magnetic and a multiphonon part, it is possible to separate their contributions. As discussed in Sec. 3.5, the dominant multiphonon process is expected to have a Q^4 dependence, whereas the magnetic contribution varies as $f^2(Q)$. Analysis of the data based on this argument indicates that 98% of the intensity at (220) is magnetic in origin.

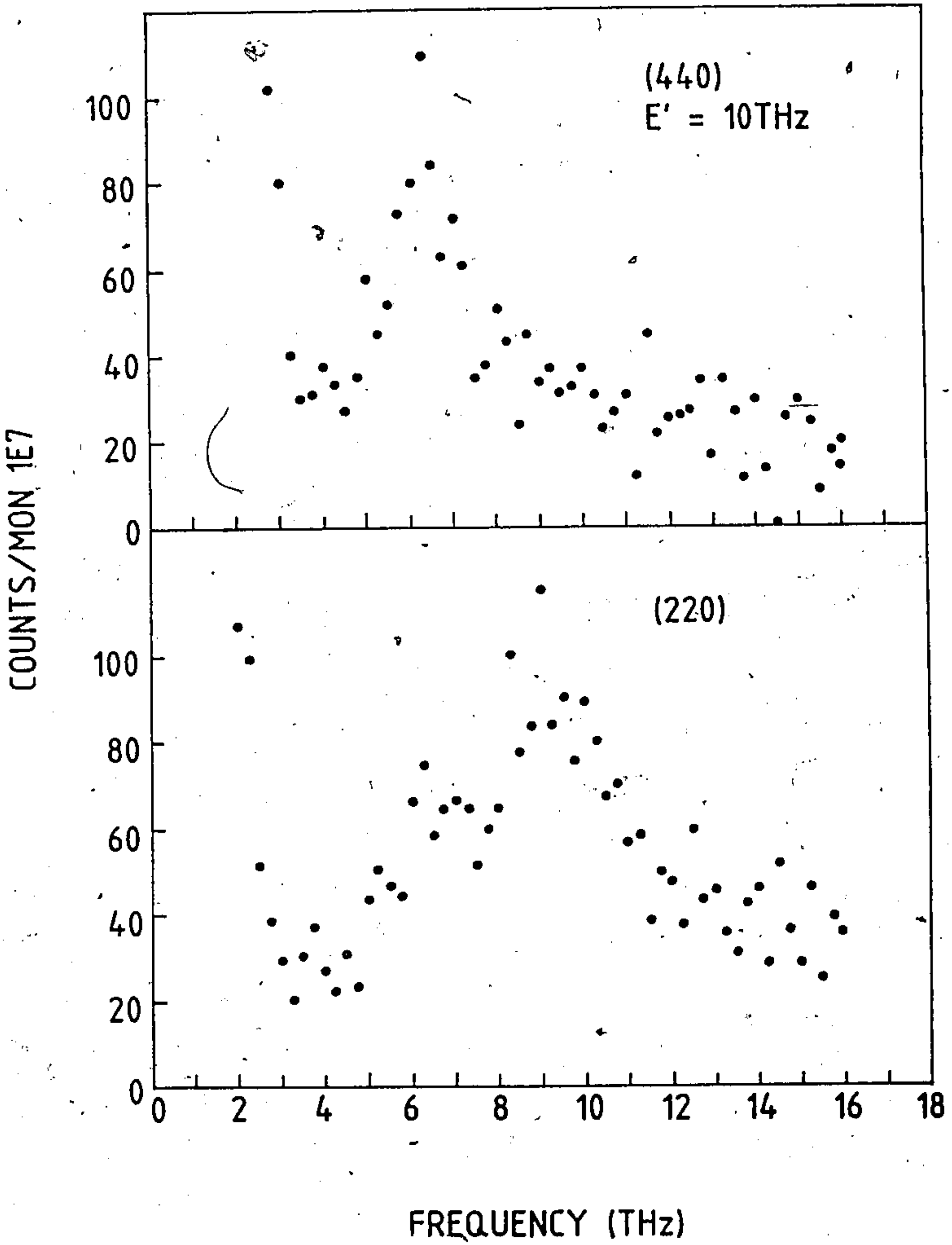

Fig. 4.3 Constant-Q scans of the zone centres (220) and (440) (with background scattering subtracted). The peak at 6 THz is an optic phonon; the broader feature at 9 THz is magnetic in origin.

Qualitatively, the zone centre magnetic scattering is well described as a broad peak centred at about 9.0 THz, and extending over a very wide frequency range, up to at least 16 THz. In fact, the response is intrinsically broad. The instrumental linewidth (for a flat branch) at the optic phonon frequency at (440) is 1.3 THz. This is entirely consistent with the observed width. The calculated resolution broadening at the magnetic peak position at (220) is 1.5 THz for a flat branch, and 1.4 THz for a branch with dispersion. (The form of the dispersion will follow). The observed width is at least three times that.

This intrinsically broad response is perhaps not unexpected. In Fig. 4.4, an example of the q = 0 response in each of the three compounds is shown. The US data is taken from Buyers (1985) and the UTe result from Holden and Buyers (unpublished). (Notice that the energy axis has been shifted in the UTe data.) In each case the resolution of the spectrometer is shown by a horizontal bar. In UTe, the magnetic excitation appears as a sharp, resolution-limited peak in the spectrum whereas in US only a broad continuum of magnetic scattering, much wider than the resolution, is observed. USe exhibits behaviour intermediate between US and UTe.

4.4 Dispersion

The inelastic response at wave vectors away from the zone centre, in the (111) direction, are shown in Figs. 4.5 (a) and (b). The optic phonon intensity increases across the zone in a manner consistent with the one-phonon cross section: the dashed lines are the calculated intensities based on the eigenvectors obtained from a rigid-ion model analysis of Jackman et al (1986). (The precise calibration procedure is outlined in Sec. 4.5.)

Fig. 4.4
Zone-centre response of the uranium chalcogenides. (The UTe data is from Holden and Buyers (unpublished) and the US data from Jackman 1983). Horizontal bars indicate spectrometer resolution. In UTe, a sharp, resolution-limited excitation is observed while in US only a broad inelastic continuum of scattering exists. USe exhibits intermediate behaviour. The right-hand scale shows the dynamic susceptibility in absolute units.

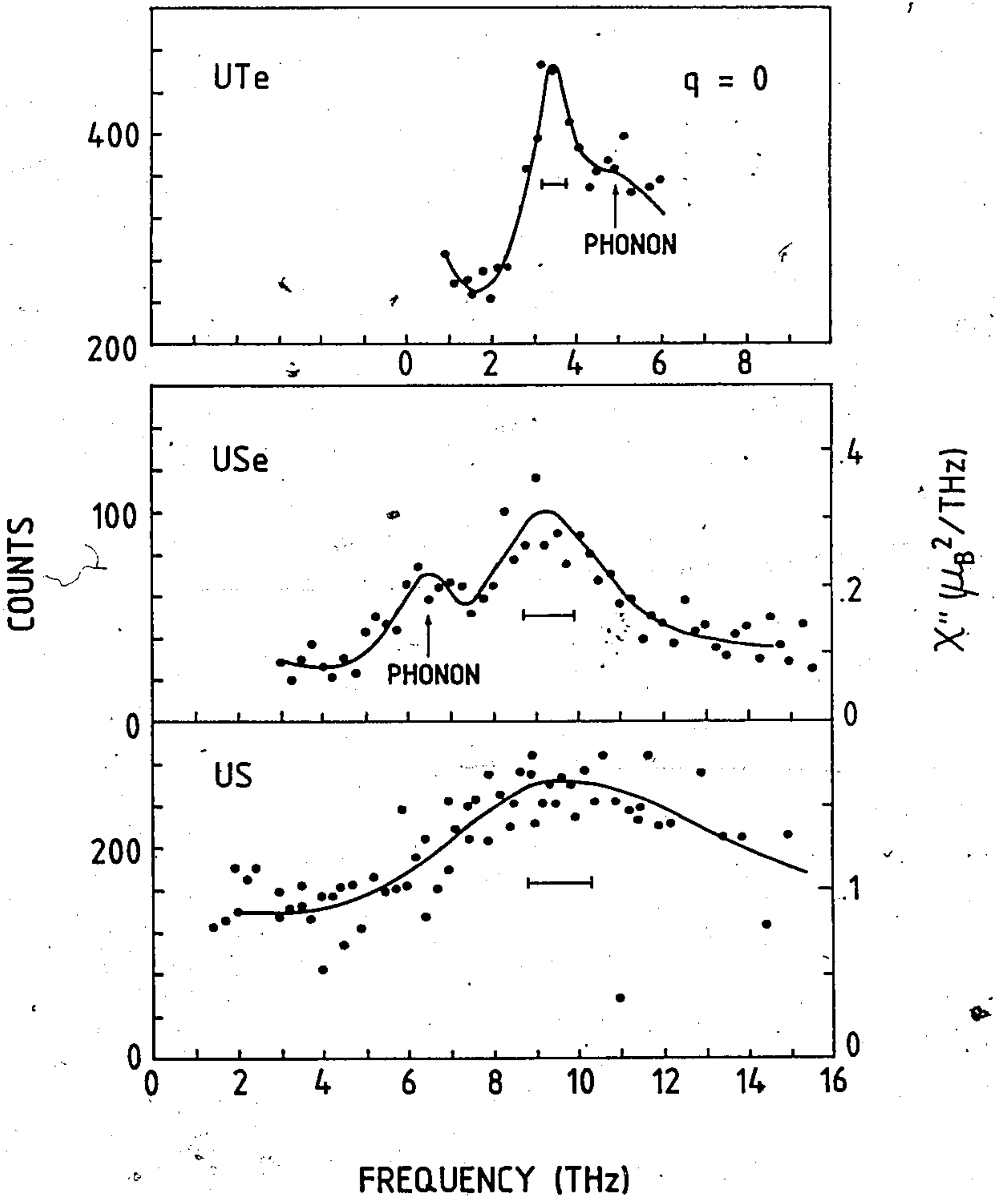
UTe
q = 0
400
200
0
2
4
6
8
PHONON
USe
100
0
PHONON
.4
.2
0
X'' (μ_B^2/THz)
COUNTS
US
200
0
.1
0
0
2
4
6
8
10
12
14
16
FREQUENCY (THz)

Fig. 4.5 (a), (b)
Wave-vector dependence of the inelastic response in USe. The measurements were made in the (220) Brillouin zone along the (ζζζ) direction. The dashed line shows the rigid-ion model calculation of the optic phonon intensity. The solid line is a fit of the magnetic intensity to a damped harmonic oscillator function (Eq.[4.11]). The scale on the right-hand side shows the dynamic susceptibility in absolute units.

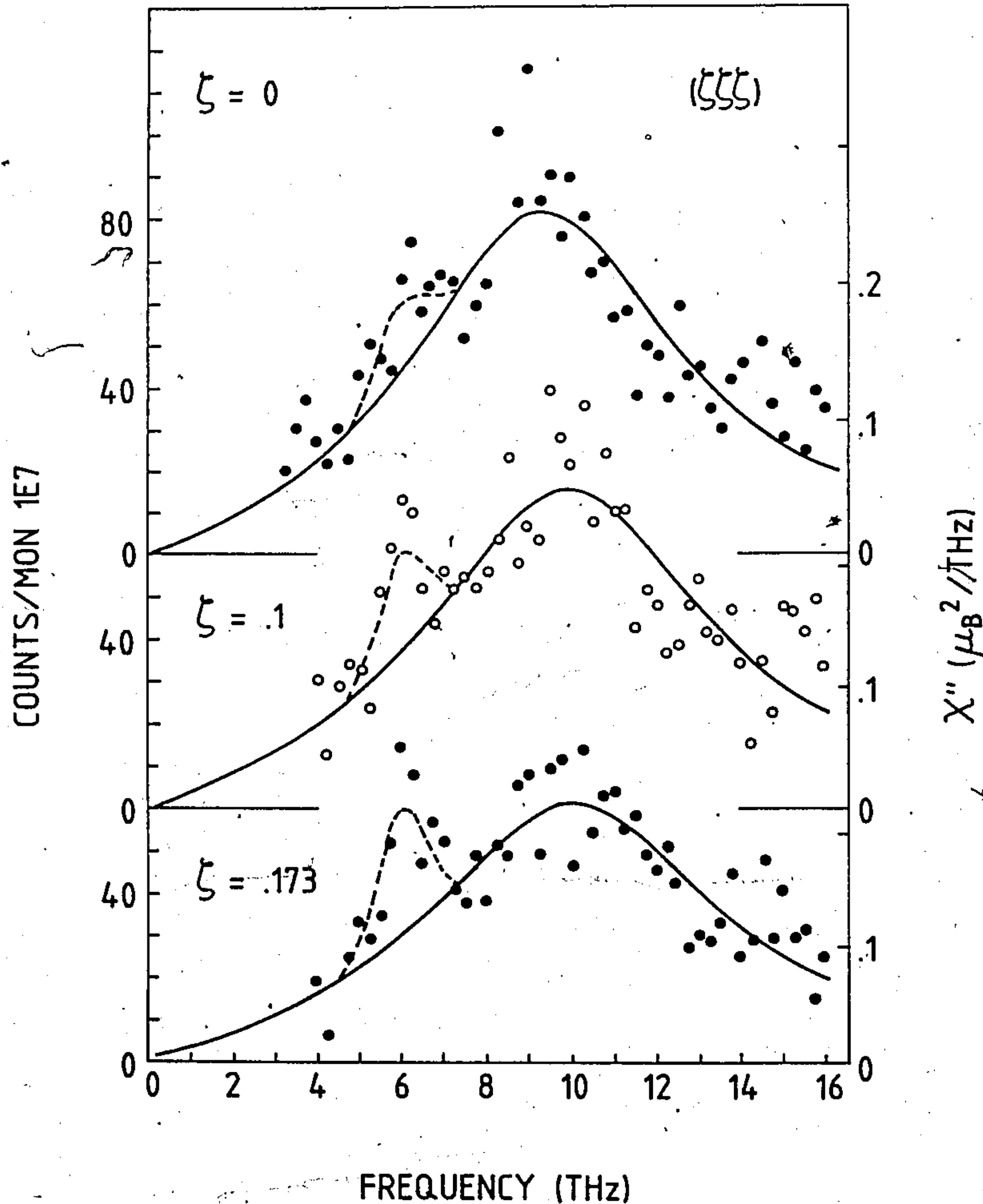
ζ = 0
($\zeta\zeta\zeta$)
ζ = .1
ζ = .173
COUNTS/MON 1E7
80
40
0
40
0
40
0
X'' ($\mu_B^2/\hbar$THz)
.2
.1
0
.1
0
.1
0
0
2
4
6
8
10
12
14
16
FREQUENCY (THz)

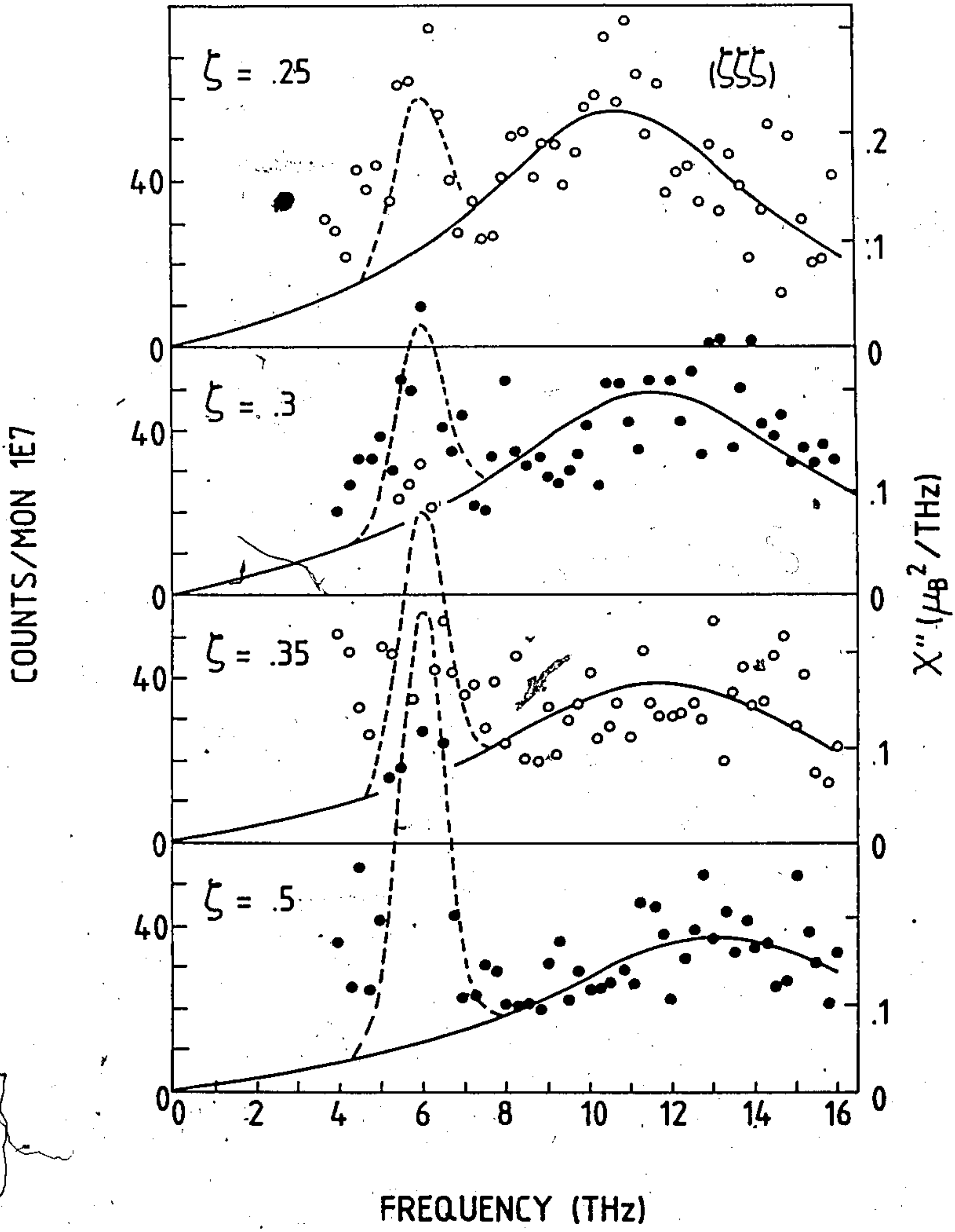
ζ = .25
(ζζζ)
ζ = .3
ζ = .35
ζ = .5
40
0
.2
.1
0
COUNTS/MON 1E7
X''(μB²/THz)
0
2
4
6
8
10
12
14
16
FREQUENCY (THz)

Again, data taken at corresponding wave vectors in the (440) Brillouin zone confirm that the scattering at energies greater than 6 THz is magnetic. The solid lines are fits to the magnetic intensity of a damped harmonic oscillator function. (See Sec. 4.6). At small q, the peak in the magnetic response is fairly well defined. The counting statistics limit the interpretation, but as q increases the peak energy increases while the peak broadens and weakens in intensity. A plot of peak position against the wave-vector coordinate in the (111) direction is shown in Fig. 4.6. The dashed line is a fit to a quadratic dispersion law, where the stiffness constant, D, is estimated to be 7.0 ± 2 THz-$Å^2$.

It is evident that the observed excitations in USe and US can not be described by either the strictly local or strictly itinerant limits since even at q = 0 the response is intrinsically broad. However in Chapter 6 it is shown that many of the magnetic properties of the UX systems can be described by assigning to the U ion a localized f^3 electronic configuration. If this is the case, a model of a local moment system in which the magnetic excitations are externally damped might be appropriate.

4.5 Calibration

A more quantitative analysis can be made by converting the scattering intensity to a dynamic susceptibility in absolute units. In this section the calibration procedure is outlined. In the following section, the measured dynamic susceptibility is used to estimate $\langle M^2 \rangle$, the square moment at a site, by the total moment sum rule.

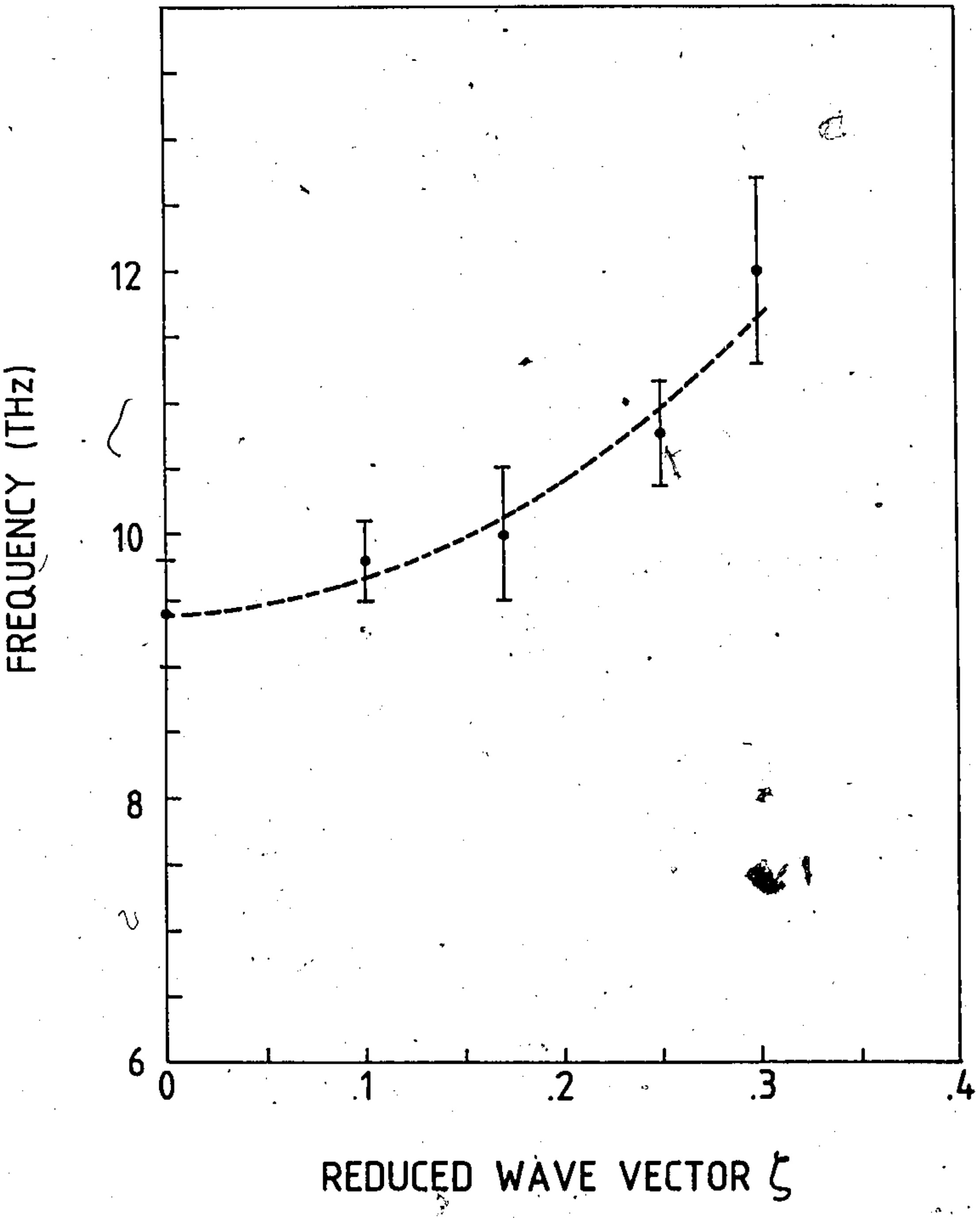

Fig. 4.6 Measured dispersion of the magnetic excitations in USe in the ($\zeta\zeta\zeta$) direction. The dashed line is a fit to a quadratic dispersion law with a stiffness constant, D, of about 7 THz-Å^2.

The cross section for inelastic magnetic scattering (Eq. [3.9]) may be written as

$$\left(\frac{d^2\sigma}{d\Omega dE'}\right)_{\vec{Q},\omega} = \frac{Nk'}{k} F(Q,\omega)\ \chi''(\vec{q},\omega) \qquad [4.1]$$

where $F(Q,\omega)$ contains all of the known constants, together with the form factor, the Debye-Waller factor and the detailed balance factor. χ'' for the multidomain configuration is given by

$$\chi''(\vec{q},\omega) = \frac{1}{3}\left(\chi''_{zz}(\vec{q},\omega) + 2\ \chi''_{xx}(\vec{q},\omega)\right) \qquad [4.2]$$

In order to put the measurements on an absolute scale it is necessary to define the relationship between $T(\vec{Q},\omega)$, the intensity of the magnetic scattering, and the cross section. Since $T(\vec{Q},\omega)$ is the actual number of counted neutrons, it must depend of the incident neutron flux, Φ, the counting time, t, and the efficiency of the analyzer (which goes like $k'^3\cos\theta_A$), i.e.

$$T(\vec{Q},\omega) \propto \Phi t k'^3 \cos\theta_A \left(\frac{d^2\sigma}{d\Omega dE'}\right)_{\vec{Q},\omega} \qquad [4.3]$$

Experimentally, Φ and t are incorporated into the monitor count rate, M. The fission detector has an efficiency for detecting neutrons that goes like 1/k so that

$$t \propto \frac{kM}{\Phi} \qquad [4.4]$$

Substituting into Eq. [4.3], $T(Q,\omega)$ becomes

$$T(\vec{Q},\omega) \propto MNk'^4 \cos\theta_A\ F(Q,\omega)\ \chi''(\vec{q},\omega) \qquad [4.5]$$

Notice that k, the wave vector of the incident neutron, no longer appears. The remaining coefficient is a constant since E' is fixed, so that

$$T(\vec{Q},\omega) = CF(Q,\omega)\ \chi''(\vec{q},\omega) \qquad [4.6]$$

where C is a constant which must be determined experimentally.

C can be estimated using one-phonon data. To see this, consider the one-phonon cross section, Eq. [3.13], rewritten in the compact form

$$\left(\frac{d^2\sigma}{d\Omega dE'}\right)_{\vec{Q},\omega} = \frac{Nk'}{k}\,P(\vec{Q},\omega) \qquad [4.7]$$

It is no different in form than Eq. [4.1] for the magnetic scattering, and it follows that $I(\vec{Q},\omega)$, the measured intensity of the one-phonon scattering, is related to $P(\vec{Q},\omega)$ by

$$I(\vec{Q},\omega) = CP(\vec{Q},\omega) \qquad [4.8]$$

where C is the same constant as in Eq. [4.6]. The important point here is that C is the only unknown in Eq. [4.8]: $P(\vec{Q},\omega)$ can be calculated using the eigenvectors obtained from rigid-ion model calculations of Jackman et al (1986), and $I(\vec{Q},\omega)$ is the (integrated) intensity of the phonon, determined directly from the experiment.

Examples of the phonon groups used in the calibration are shown in Fig. 4.7. The solid line is a Gaussian fit to the peak using the linewidth determined by the resolution function. The integrated intensities, together with their calculated cross sections are listed in Table 4.1

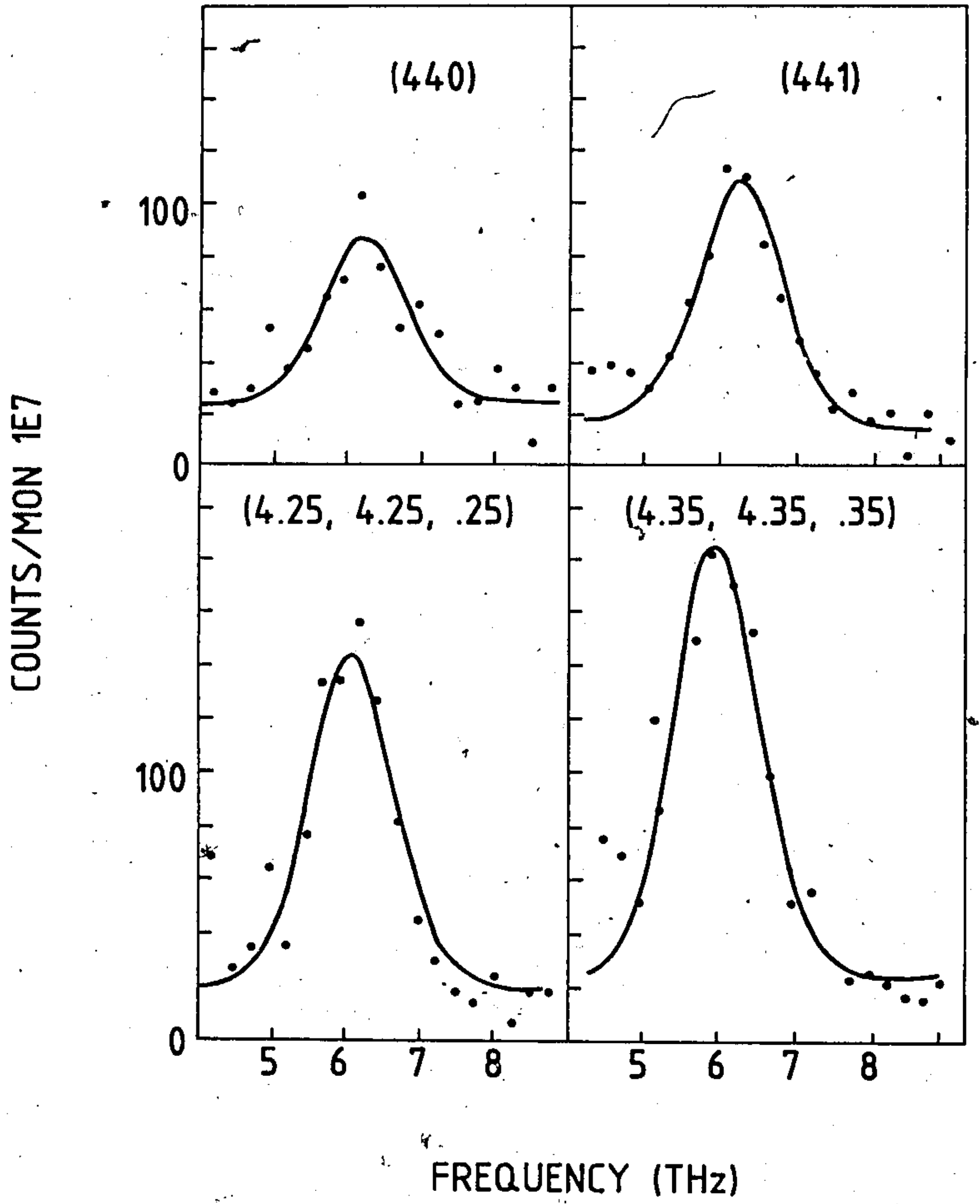

Fig. 4.7 Typical phonon groups used in the calibration of the scattering intensity.

Table 4.1. Phonon cross sections and intensities. The calibration constant is the ratio of intensity to cross section.

Phonon Wave Vector	Calculated Cross Section barn($\times 10^3$)	Integrated Intensity Cts-THz	Calibration Constant Cts-THz-barn^{-1} ($\times 10^3$)
(4.0 , 4.0 , 0.0)	7.0	87±10	12.4±1
(4.10, 4.10, 0.10)	8.0	129	16.1
(4.25, 4.25, 0.25)	12.0	160	13.3
(4.30, 4.30, 0.30)	14.5	182	12.6
(4.35, 4.35, 0.35)	17.7	226±40	12.8±2
(4.0 , 4.0 , 1.0)	10.9	127	11.7
(2.5 , 2.5 , 0.50)	10.4	102	9.8

The average value of C is $(12.7 \pm 2) \times 10^3$ Cts-THz-barn^{-1} for the monitor count 1E7.

The scale on the right hand side of Figs. 4.4 and 4.5 give the dynamic susceptibility (Eq. [4.2]) in units of $\mu_B{}^2$/THz. The calibration for the US data was performed by Jackman (1983).

4.6 Calculation of $\langle M^2 \rangle$

It was shown by Buyers and Holden (1983) that the square moment at a magnetic site, $\langle M^2 \rangle$, is related to the scattering function, $S(\vec{q},\omega)$, by

$$\langle M^2 \rangle = \frac{1}{N} \sum_{\vec{q}} \int_0^\infty d\omega \sum_{\alpha} g_\alpha^2 \, S_{\alpha\alpha}(\vec{q},\omega) \, (1 + e^{-\beta\hbar\omega}) \qquad [4.9]$$

where the sum over $\vec{q}$ extends over a Brillouin zone. Replacing $S(\vec{q},\omega)$ by the dynamic susceptibility, $\chi''(\vec{q},\omega)$, Eq. [4.9] becomes

$$\langle M^2 \rangle = \frac{3}{N} \, \frac{1}{\pi} \sum_{\vec{q}} \int_0^\infty d\omega . \frac{1}{3} \left(\chi''_{zz}(\vec{q},\omega) + 2\chi''_{xx}(\vec{q},\omega)\right) \mathrm{COTH}\left(\frac{\beta\hbar\omega}{2}\right) \qquad [4.10]$$

(χ'' is an antisymmetric function and so must go to zero as $\omega \to 0$. Thus despite the divergence in the COTH term at $\omega = 0$, the integrand is always finite). The sum rule is limited to local moment systems and need not apply to systems in which the moment at a site is not conserved (as in valence fluctuators).

Because the available data covers only a finite frequency range at discrete values of q, it is necessary to interpolate the argument of the integral. To facilitate this, the magnetic contribution to the scattering was compared to a number of functional forms. The best fits were achieved with a damped harmonic oscillator function

$$\chi''(\vec{q},\omega) = \frac{A\omega}{(\omega^2-\omega_0^2)^2 + (\Gamma\omega)^2} \qquad [4.11]$$

where A, ω_0 and Γ are functions of q. Jackman (1983) performed a similar analysis on the scattering in the low temperature ferromagnetic phase of US and found that in order to achieve a good description of the scattering at low energies (<6 THz) a second quasi-elastic component to the spectrum was required. In USe the magnetic scattering in this energy range is completely obscured by the one-phonon scattering: the function (Eq. [4.11]) assumes that χ'' is (approximately) linear in frequency in this range. The fitted parameters A, ω_0 and Γ are plotted as a function of q in (the three lower panels of) Fig. 4.8.

Apart from the COTH term, which contributes only at small ω, the integral over ω can be performed analytically. (The correction can be calculated numerically and is less than 1%) The result of the energy integration at each q is shown in the top panel of Fig. 4.8. The

Fig. 4.8
Wave-vector dependence of the damped harmonic oscillator parameters A, ω_0, and Γ (Eq. [4.11]). The top panel shows the (energy) integrated intensity of the dynamic susceptibility.

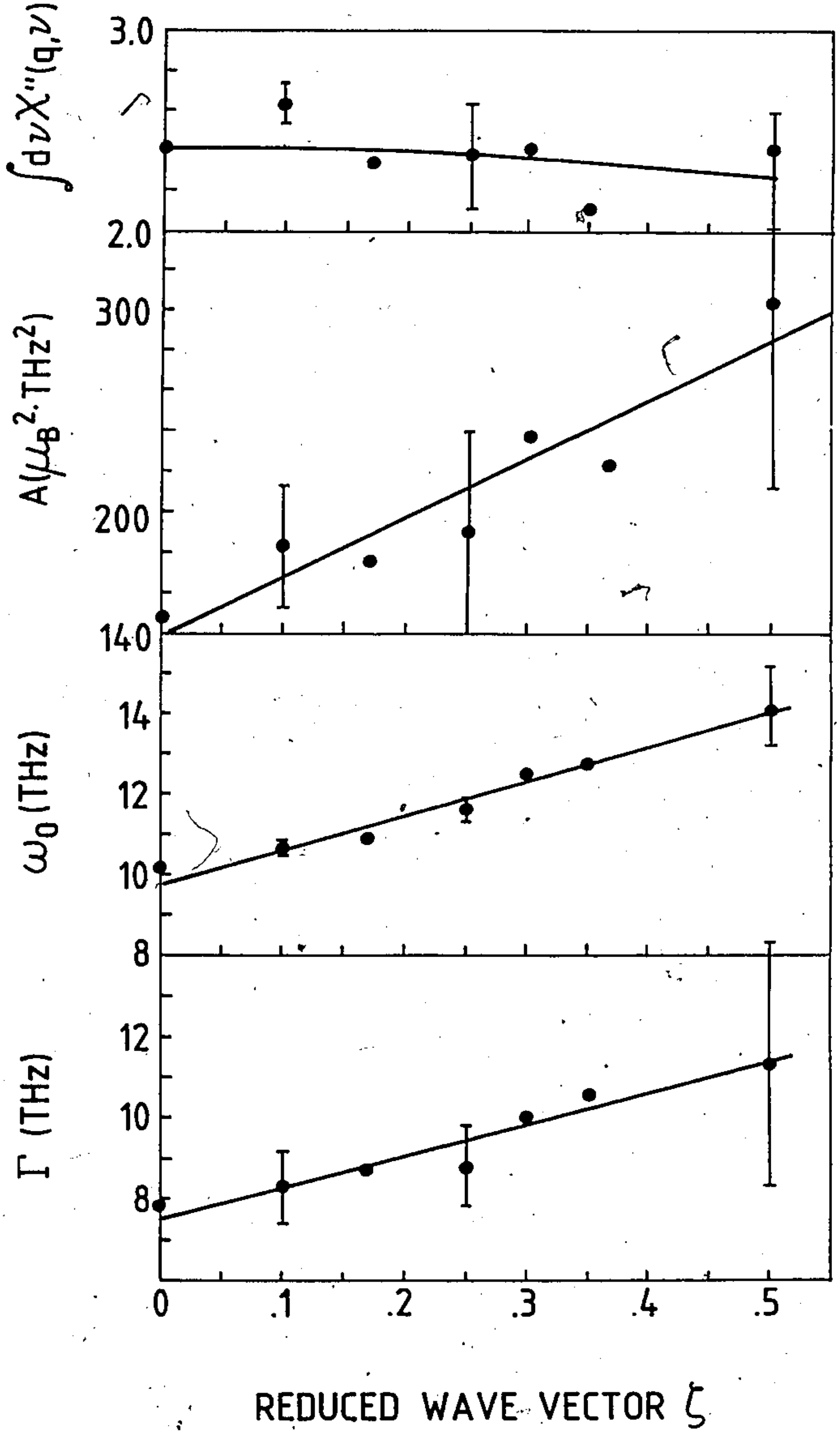

∫dν χ''(q,ν)
3.0
2.0
A(μ_B^2·THz^2)
300
200
140
ω_0 (THz)
14
12
10
8
Γ (THz)
12
10
8
0
.1
.2
.3
.4
.5
REDUCED WAVE VECTOR ζ

uncertainties are estimated from the uncertainties in the fitted parameters, taking into account their correlations (for example, at fixed ω_0, $\Delta A/\Delta\Gamma > 0$). At q=0, the contribution to the integral from the accessible energy range (up to 16 THz) is 85% of the total (that is, 15% of the total comes from the extrapolated region of energies greater than 16 THz). At q = (0.5, 0.5, 0.5), it is 60%. The solid line is obtained by assuming that A, ω_0 and Γ vary linearly with q (the solid lines in the lower panels).

The sum over the Brillouin zone is performed by assuming that the scattering is isotropic in q. The summation is replaced by an integral and the upper limit of q determined by approximating the Brillouin zone by a sphere of radius q_{zb} which has the same volume as the Brillouin zone, i.e.

$$\frac{1}{N}\sum_{\vec{q}} \rightarrow \frac{V}{(2\pi)^3}\int_0^{q_{zb}} dq\, 4\pi q^2 \qquad [4.12]$$

where V is the volume of the primitive unit cell in real space ($a^3/4$) and q_{zb} is given by

$$\frac{4}{3}\pi q_{zb}^3 = \frac{(8\pi)^3}{(a^3/4)} \qquad [4.13]$$

Equation [4.10] becomes

$$\langle M^2\rangle = \frac{3}{2}\frac{V}{\pi^3}\int_0^{q_{zb}} dq\, q^2\, \chi''(q) \qquad [4.14]$$

The square moment estimated in this way is 2.3 ± 0.3 μ_B^2. (The largest numerical uncertainty in the calculation is in the value of the calibration constant which is of order 15%.) Taking into account the contribution of the ordered moment (2.0 μ_B), we estimate a square moment/site of 6.3 ± 0.3 μ_B^2. For comparison, $\langle M^2 \rangle$ is ≈ 13 μ_B^2 for an f^2 or f^3 local moment ground state, and ≈ 6 μ_B^2 for an f^1 state.

In the local moment picture, such a reduced moment could arise even in an f^2 or f^3 electron configuration in the presence of a crystal field splitting. If only the lowest crystal field state were populated in the temperature range of the measurements, then the entire f^2 or f^3 moment would not be accessible. Such a model is discussed in Chapter 6.

CHAPTER 5: SPIN-WAVE POLARIZATION MEASUREMENT

A spin wave, in the classical sense, is a transverse excitation. However, in the most general case of a system with both spin and orbital angular momentum contributions in a crystalline environment, it is possible to have longitudinal excitations as well. In the antiferromagnetic pnictinde compound, UN, the polarization of the magnetic scattering has been measured and is known to be longitudinal (Holden, 1984).

The experiment described in the previous chapter was carried out on a multidomain sample. As discussed in Sec. 3.4, it is impossible to determine ~~the~~ polarization of the magnetic excitation from these observations. In this chapter, the results of measurements made on a single domain sample are presented.

5.1 Details of the Measurement

The measurements were carried out on the N5 triple axis spectrometer at the NRU reactor, Chalk River. The monochromator was beryllium (002), mosaic spread of 0.33°, and the analyzer pyrolytic graphite (002), mosaic spread of 0.35° The collimation before and after the sample was 0.75° and 1.02° respectively.

The measurements were made in constant-Q mode with a fixed E' of 10 THz. The fast neutron background and the background from the sample holder, cryostat, etc. were measured as described previously (Sec. 4.2).

A single ordered domain was produced by cooling the sample through its ferromagnetic ordering temperature in a magnetic field of 2T with the field parallel to the <111> direction. Magnetic Bragg scattering can not be observed at any Bragg point, $\vec{\Gamma}$, which is along the ordering direction (Sec. 3.2). As a result the weak nuclear Bragg reflections (111) and (11$\bar{1}$) could be used to monitor the formation of the magnetic domains: the magnetic scattering from a domain with magnetization axis along <111> can be observed at (11$\bar{1}$) but not (111). Similarly, if a domain forms with an axis other than <111>, magnetic scattering will appear at (111).

Figure 5.1 shows the variation in intensity of the (111) and (11$\bar{1}$) Bragg peaks for the field-cooled sample. The intensity at (111) was virtually constant as the temperature was lowered, while the (11$\bar{1}$) intensity increased by a factor of about 30 between 180 K and 4 K. This indicates the formation of a single domain aligned along <111>. The magnetic field was maintained at all times during this part of the experiment and the reflections checked periodically to ensure that the sample had not depolarized.

Some of the measurements made in the single domain sample were repeated in a multidomain configuration obtained by cooling the sample through the phase transition in the absence of an aligning field. In this case, there was no difference between the Bragg peak intensities at (111) and (11$\bar{1}$).

5.2 Polarization of the Magnetic Scattering

The strategy for the polarization measurement is shown in Fig. 5.2 The magnetization axis of the single domain is parallel to the

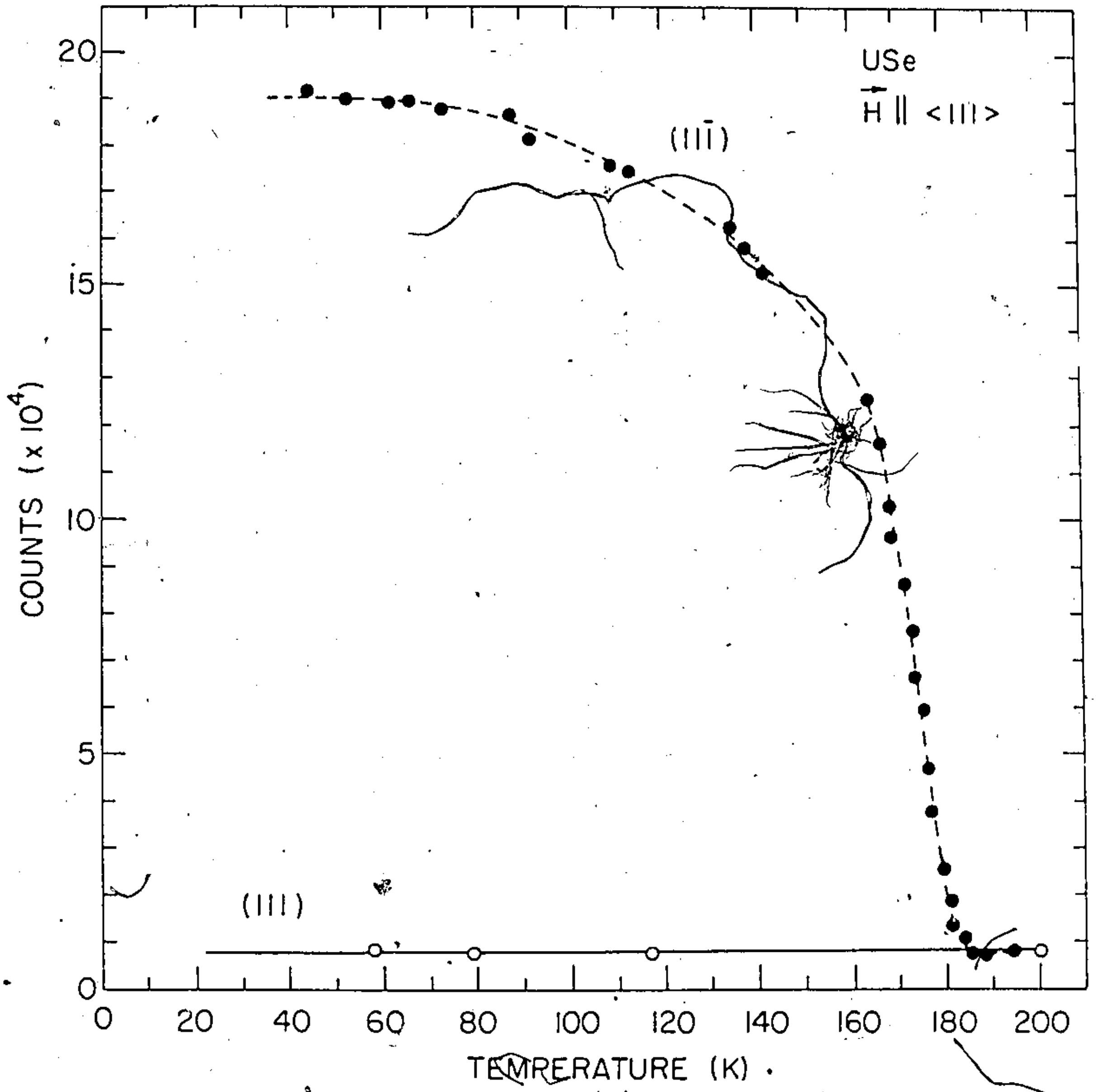

Fig. 5.1 Temperature dependence of the (111) and $(11\bar{1})$ Bragg peaks as the sample is cooled through the ferromagnetic phase transition in an aligning field. No change in intensity is observed at (111) indicating the formation of a single domain along <111>.

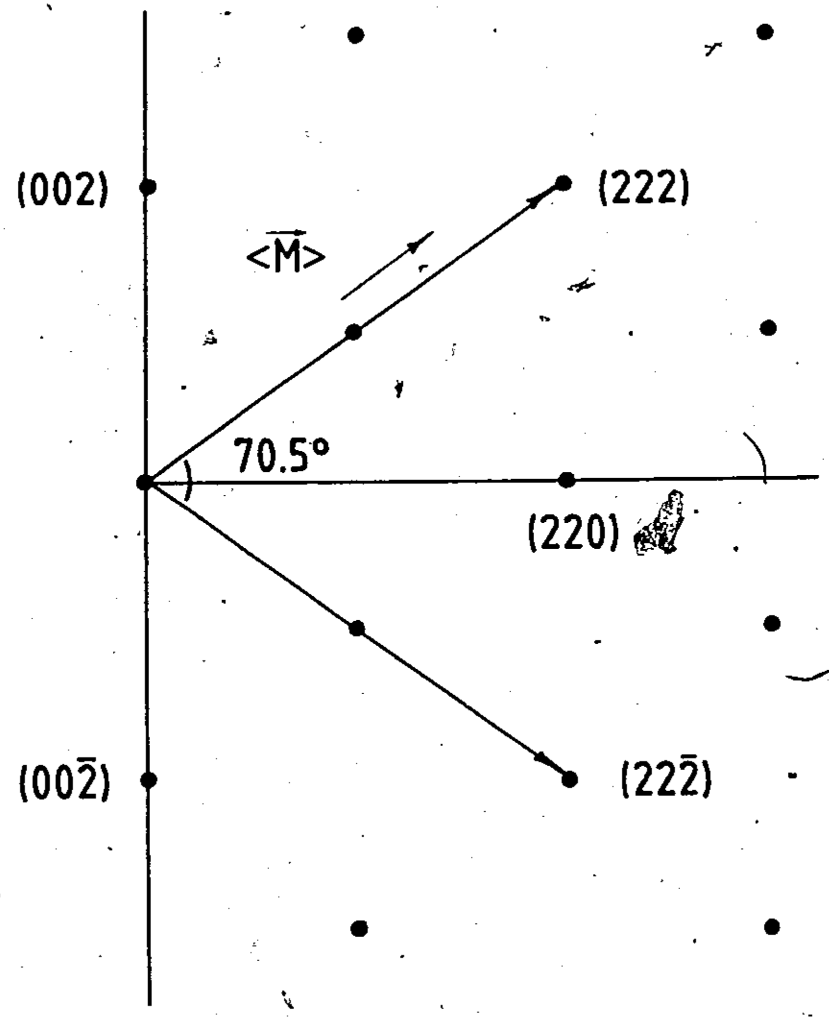

	$1-Q_z^2$	$1+Q_z^2$
(222)	0	2
$(22\bar{2})$	8/9	10/9

Fig. 5.2 The geometry of the polarization measurement. (222) is parallel to the magnetization direction while $(22\bar{2})$ is 70.5° away. The coefficients of the longitudinal and transverse response are shown in the table. (See Eq. [3.9]).

<111> direction. Consider only the zone centres (222) and $(22\bar{2})$. (222) is parallel to the magnetization axis, while $(22\bar{2})$ is at an angle of 70.5°. As a result, a purely longitudinal excitation would appear at $(22\bar{2})$ but not at (222). A purely transverse excitation would appear at both zone centres but with an intensity at $(22\bar{2})$ 56% of that at (222). (Sec. 3.4)

Figure 5.3 shows the results of measurements made at the zone centre (220) in a multidomain configuration, together with the measured (smoothed) background. The background includes both the blank and fast neutron components. The peak in the background at about 5 THz appears in all of the inelastic scans independent of Q. This is qualitatively the same feature observed in the previous measurements, but is much more intense. (It is in fact probably too intense to be attributed to simply Al density of states scattering since the Al cross section is almost entirely coherent.)

In Fig 5.4 the background-subtracted data is shown together with measurements made at the same wave vector in the previous experiment (where the background contribution to the scattering was not as significant). The intensities have been normalized for this plot. The results are quite consistent.

The data (with background subtracted) for the zone centres (222) and $(22\bar{2})$ in the single domain sample are shown in Fig. 5.5. (The solid lines are only guides to the eye, and the same guide is drawn through both sets of data). The fact that the magnetic excitation appears at (222) means that its polarization is at least partially transverse. It cannot be purely transverse, however, since the intensity at $(22\bar{2})$ does

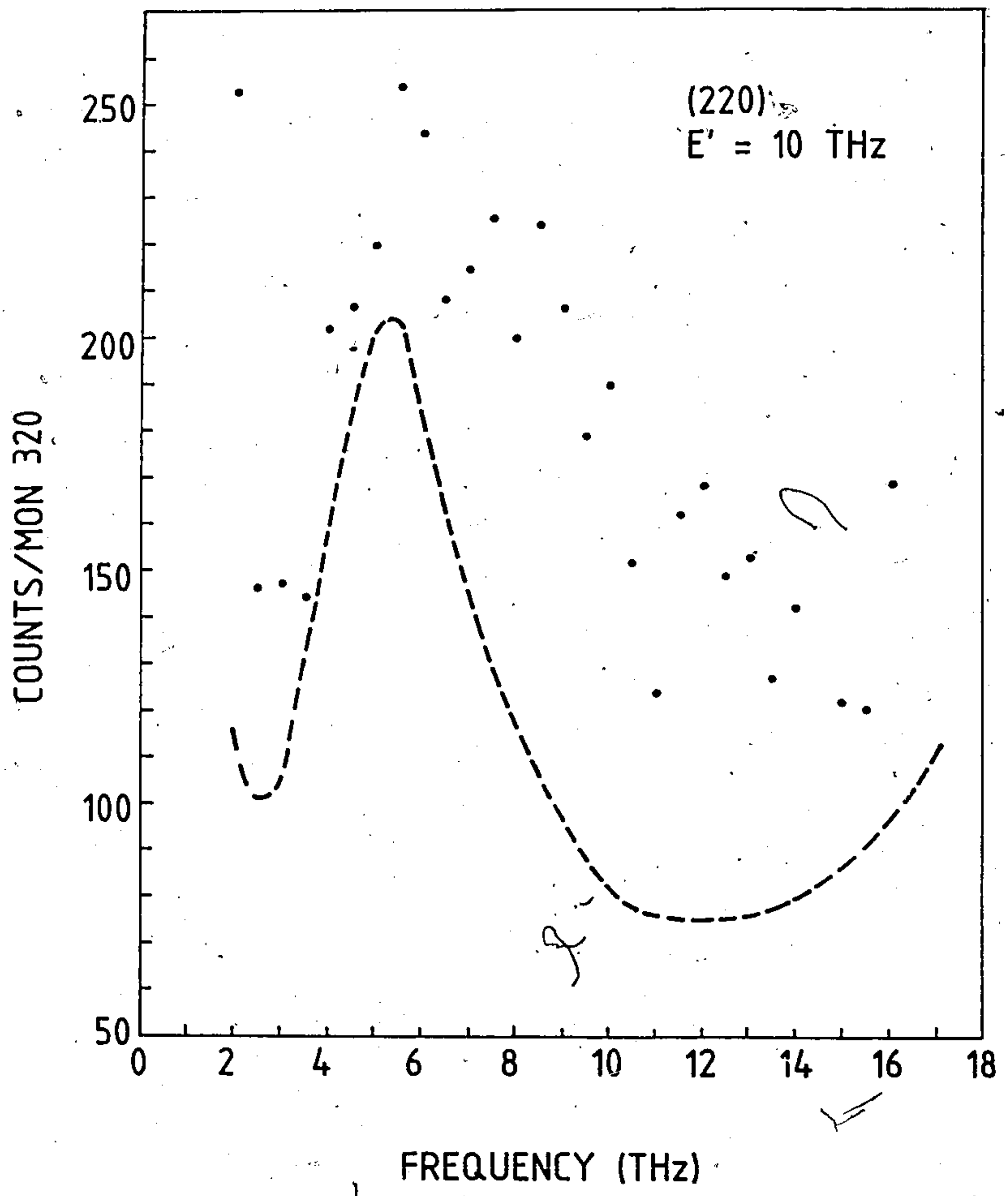

Fig. 5.3 Constan[illegible]an at (220) together with its measured backgr[illegible]

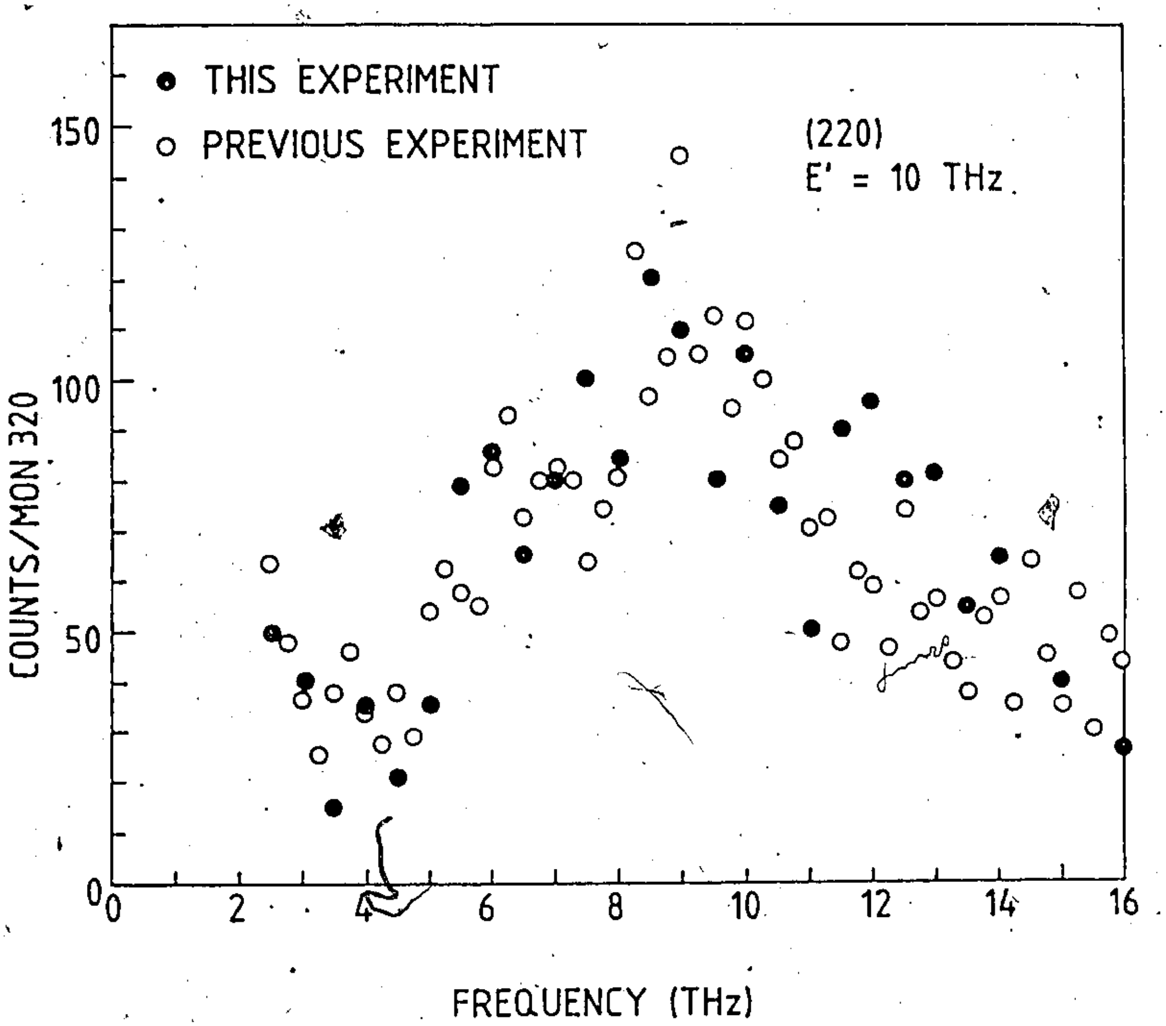

Fig. 5.4 Constant-Q scan at (220) with background subtracted (solid dots). This result is consistent with the measurement of Chapter 4 (open circles).

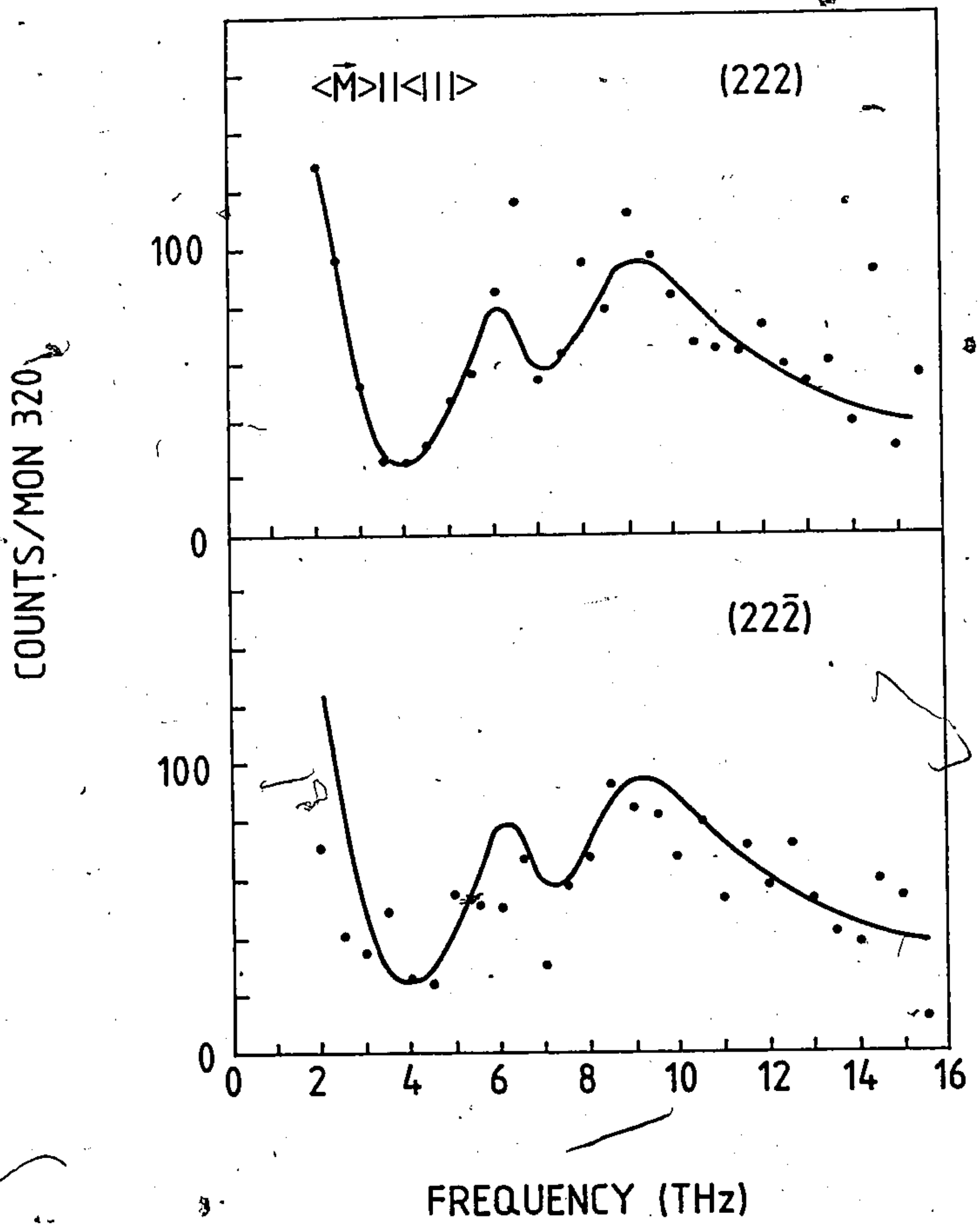

Fig. 5.5 Constant-Q scans at equivalent zone centres (222) and (22$\bar{2}$) in the single domain sample. The solid line is a guide to the eye and the same guide is drawn through both scans.

not decrease to the value of 56% expected for transverse scattering alone. The ratio of the measured (integrated) intensities at $(22\bar{2})$ to (222) is 0.96 ± 0.15 which leads to a ratio of longitudinal to transverse susceptibilities of 0.91 ± 0.33. (See the table accompanying Fig. 5.2). Within the uncertainty of the measurement, the longitudinal and transverse susceptibilities are equal.

This conclusion is further confirmed by the absence of any significant difference between measurements made on the single domain sample and those made on the multidomain sample. Data taken in the multidomain configuration at (222) and $(22\bar{2})$ are shown in Fig. 5.6. The solid curve is the same as that used for the single domain results.

In UN the low temperature excitation spectrum consists of a broad continuum of of inelastic scattering, which has been shown to be of longitudinal polarization (Holden, 1984). f-d fluctuations, in the sense of a U ion emitting and reabsorbing a conduction electron of the same spin, could give rise to longitudinal scattering since the process is spin conserving. This valence fluctuations type behaviour would also account for the exceedingly small moment ($\approx 0.8\ \mu_B$) observed in UN.

It should be pointed out that the measurements do not unambiguously define the polarization of the excitation. Rather, they define the polarization of the scattering. If the scattering were to arise from transitions to a set of closely spaced levels, some with transverse, and some with longitudinal polarization, then the scattering may appear unpolarized whereas the underlying excitations have definite polarizations.

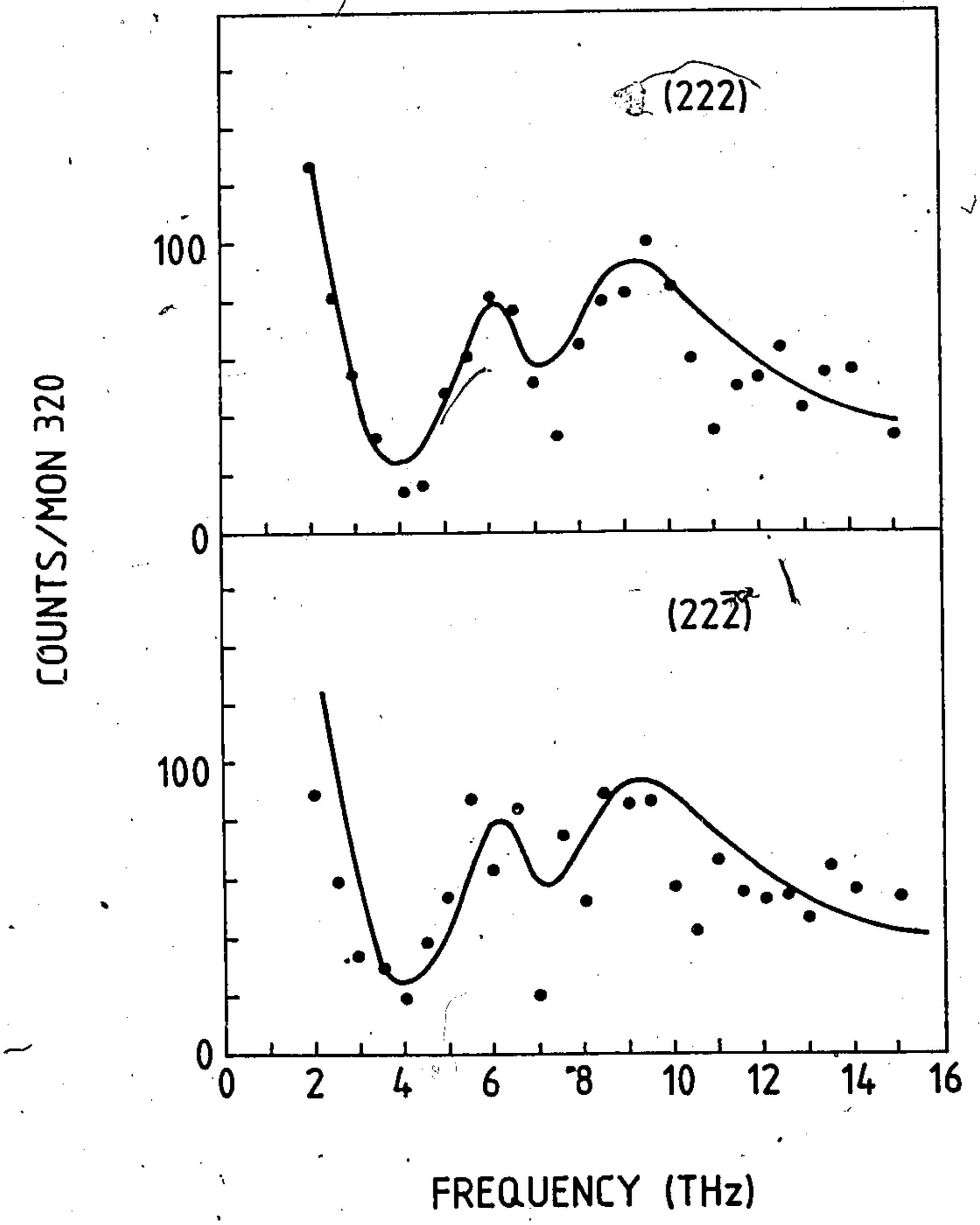

Fig. 5.6 Constant-Q scans at equivalent zone centres (222) and (22$\bar{2}$) in a multidomain configuration. The same solid line is drawn through both Figs. 5.5 and 5.6.

In Chapt. 6 it is shown that a local moment model can give a good description of the static magnetic properties as well as predict the energy scale of the excitations. However, it predicts only excitations with transverse polarization. To be a useful description, such a model must be augmented by a mechanism which produces not only broadening but "depolarization" of the excitation.

CHAPTER 6: ANALYTIC DESCRIPTION OF THE UX COMPOUNDS

6.1 Localized Model

Jackman (1983) found that the static magnetic properties of the uranium chalcogenides could be well described if the uranium ion was treated as a local moment system in the presence of a cubic crystal field. In both the f^2 and f^3 Hund's rule ground states it was possible to identify crystal field and exchange parameters which reproduced the observed paramagnetic susceptibility and the moment in the ordered phase. However the low temperature dynamic response, in particular, the large zone centre anisotropy gap could not be accounted for.

The ferromagnetic ordering in the chalcogenides is accompanied by a large rhombohedral distortion of the cubic lattice. As such, it might be expected that coupling between magnetic moments and bulk elastic strain is an important feature of these systems. In this chapter the local moment analysis is extended to include magnetoelastic coupling and quadrupolar interactions. The treatment given here is very similar to that of Morin et al (1980) in their study of quadrupolar effects in TmZn.

6.2 The Hamiltonian

There are five separate contributions to the model Hamiltonian and these are briefly described below. The "spin", S, refers to the total angular momentum and not simply the spin component.

(1) H_{CF} is the cubic crystal field Hamiltonian. In the presence of the crystal field the (2S + 1)-fold degeneracy of the Hund's rule

ground state may be partly lifted, in a manner consistent with the site symmetry of the ion. The detailed calculation of the cubic crystal field potential is reviewed by Hutchings (1964). In its "operator equivalent" form (Stevens, 1952: Stevens and Bleaney, 1953), with respect to a (001) axis, the crystal field Hamiltonian is

$$H_{CF} = B_4(O_4^0 + 5O_4^4) + B_6(O_6^0 - 21O_6^6) \qquad [6.1]$$

where the O_n^m are combinations of the simple dipole operators, S^+, S^-, S^z. (For precise definitions, see Hutchings, 1964).

It is convenient to replace B_4 and B_6 with the parameters x and W, defined by

$$B_4F_4 = xW \quad \text{and} \quad B_6F_6 = W(1 - |x|) \qquad -1 < x < 1 \qquad [6.2]$$

(F_4 and F_6 are constants whose magnitude depend on S). The parameter x then determines the configuration of the single-ion levels, while W determines the energy scale of their splitting. The eigenvectors and eigenvalues of the Hamiltonian were obtained by Lea, Leask and Wolf (1962) for all values of $S \leq 8$, and over all values of x.

(2) H_{EX} is the Heisenberg exchange Hamiltonian given by

$$H_{EX} = -\sum_{ij} J_{ij}\vec{S}_i \cdot \vec{S}_j \qquad [6.3]$$

where $\vec{S}_i$ is the spin of the ith atom and J_{ij} is the exchange constant. The exchange constant measures the strength of the interaction and determines its sense; if J>0, the interaction is ferromagnetic, whereas if J<0, the interaction is antiferromagnetic.

(3) H_Q is the quadrupole-quadrupole interaction Hamiltonian. It arises from an interaction which is biquadratic in the spin coupling i.e. $(\vec{S}_i \cdot \vec{S}_j)^2$. The most general form of the quadrupole exchange Hamiltonian in a cubic lattice is (Sivardiere, 1975)

$$H_Q = -\frac{1}{12}\sum_{ij} K_1(ij)\,[O_2^0(i)\,O_2^0(j) + 3O_2^2(i)\,O_2^2(j)] + 3[P_{xy}(i)\,P_{xy}(j) + P_{yz}(i)\,P_{yz}(j) + P_{zx}(i)\,P_{zx}(j)] \qquad [6.4]$$

where O_n^m and P_{ij} are the quadrupole operators (defined in Appendix A.2) and the K_{ij} are the quadrupole exchange energies.

(4) H_{ME} is the magnetoelastic coupling. The rhombohedral distortion in the ferromagnetic phase changes the site symmetry of the uranium ion and requires the introduction of off-cubic crystal field terms. The general form of the coupling (for a strained cubic structure) is

$$H_{ME} = -\frac{\sqrt{3}}{6}\,B_3(\varepsilon_1 O_2^0 + \sqrt{3}\,\varepsilon_2 O_2^2) - \frac{1}{2}\,B_5(e_{xy}P_{xy} + e_{yz}P_{yz} + e_{zx}P_{zx}) \qquad [6.5]$$

where ε_{ij} and e_{ij} are components of the strain tensor (defined in Appendix A.1).

(5) E_{EL} is the bulk elastic energy of a strained cubic lattice, which for a general strain is

$$E_{EL} = \frac{1}{2}\left(\frac{c_{11} + 2c_{12}}{3}\right)\varepsilon_0^2 + (c_{11} - c_{12})(\varepsilon_1^2 + \varepsilon_2^2) + 2c_{44}(e_{xy}^2 + e_{yz}^2 + e_{zx}^2) \qquad [6.6]$$

where the c_{ij} are the elastic constants.

In order to carry out the calculation, the Hamiltonian of the system is first reduced to a single-ion Hamiltonian in which the effects of neighbouring spins and quadrupoles are treated in the mean field (MF) approximation. It is assumed that only nearest neighbour interactions are important. The Hamiltonian is further simplified by including only the strains that have the symmetry of the distortion in the ordered phase. For a z axis along the <111> direction, which is both the ordering direction and the axis of symmetry of the distortion, the Hamiltonian contains a single component of the strain tensor, ε, and a single quadrupole operator, O_2^0. In its simplified form,

$$H^{MF} = H_{CF} - 2J\langle S^z\rangle S^z + J\langle S^z\rangle^2 - \left(\frac{\surd 3}{6} B\varepsilon + \frac{1}{6} K\langle O_2^0\rangle\right)O_2^0 + \frac{1}{12} K\langle O_2^0\rangle^2 + 2c_{44}\varepsilon^2 \tag{6.7}$$

The details of the derivation can be found in Appendix A.3.

The calculation consists of finding the set of parameters (x,W,J,B,K) which best reproduce the observed behaviour in the paramagnetic and ordered phases. Sections 6.3 and 6.4 describe the calculation of the paramagnetic and quadrupolar susceptibilities respectively. Section 6.5 considers the behaviour in the low temperature ferromagnetic phase.

6.3 The Magnetic Susceptibility in the Paramagnetic Phase

In this section only the magnetic dipole part of the mean-field Hamiltonian is considered. In the presence of an external magnetic field, H_e, the relevant Hamiltonian is

$$H = -2J\langle S^z\rangle S^z + J\langle S^z\rangle^2 - g\mu_B H_e S^z \tag{6.8}$$

This is more conveniently written

$$H = -g\mu_B(H_e + \lambda M)S^z + \frac{1}{2}\lambda M^2 \tag{6.9}$$

(where M is the magnetization, $g\mu_B\langle S^z\rangle$, and $\lambda = 2J/(g\mu_B)^2$), since in this form it is evident that the effective field acting on each spin is the sum of the external applied field and the mean field of the other spins.

The best single ion approximation to the free energy is

$$F = -\frac{1}{2}(g\mu_B)^2\,\chi_o(H_e + \lambda M)^2 + \frac{1}{2}\lambda M^2 \qquad [6.10]$$

where χ_o is the (static) single ion susceptibility, defined in Appendix B.2. The susceptibility of the interacting spin system is defined in the usual way

$$\chi = -\frac{d^2F}{dH_e^2} \qquad [6.11]$$

and is subject to the constraint that $dF/dM = 0$. This leads to the familiar mean field expression for the susceptibility

$$\chi = (g\mu_B)^2\,\frac{\chi_o}{1 - 2J\chi_o} \qquad [6.12]$$

For a set of degenerate states, the single ion susceptibility reduces to a Curie law (i.e. $\chi_o \propto 1/T$) and the susceptibility, Eq. [6.12], to the Curie-Weiss law.

Above the critical temperature (T_c), the unperturbed Hamiltonian contains only the crystal field terms since $\langle S^z\rangle = \langle O_2^0\rangle = \varepsilon = 0$. The single ion levels are determined solely by diagonalizing H_{CF}; the susceptibility is then calculated according to

Eq. [6.12]. The only relevant parameters are x, W, and J, and these must be chosen so as to reproduce the measured static susceptibility as a function of temperature.

6.4 The Quadrupolar Susceptibility in the Paramagnetic Phase

In the previous section, the response of the system to an external magnetic field was considered. A similar treatment can be used to obtain the response to an external strain field. In this case, only the strain and quadrupole parts of the Hamiltonian contribute, i.e.

$$H = -\left(\frac{\sqrt{3}}{6} B\varepsilon + \frac{1}{6} K \langle O_2^0\rangle\right) O_2^0 + \frac{1}{12} K \langle O_2^0\rangle^2 + 2c_{44}^o \varepsilon^2 \qquad [6.13]$$

(The significance of the change in notation, i.e. $c_{44} \rightarrow c_{44}^o$, will be explained shortly). This expression is very similar to Eq. [6.9]. In this case the strain, ε, plays the role of the external field, and the system responds with a net quadrupole moment, $\langle O_2^0\rangle$, so as to minimize the free energy. Again, the single-ion approximation to the free energy has the form

$$F = -\frac{1}{2} \chi_Q \left(\frac{\sqrt{3}}{6} B\varepsilon + \frac{1}{6} K\langle O_2^0\rangle\right)^2 + \frac{1}{12} K\langle O_2^0\rangle^2 + 2c_{44}^o \varepsilon^2 \qquad [6.14]$$

where χ_Q is the single ion quadrupolar susceptibility (defined in an analogous way to the single ion magnetic susceptibility χ_o)

$$\chi_Q = -\sum_{mn} \left|\langle m|O_2^0|n\rangle\right|^2 \frac{f_m - f_n}{\omega_m - \omega_n} \qquad [6.15]$$

The interacting 'susceptibility' in this case, χ_{EL}, is defined by

$$\chi_{EL} = \frac{d^2F}{d\varepsilon^2} \qquad [6.16]$$

From Eq. [6.14]:

$$\chi_{EL} = 4c_{44}^o \left(\frac{1-K_Q\chi_Q - K_{ME}\chi_Q}{1 - K_Q\chi_Q}\right) \qquad [6.17]$$

where $K_Q = \frac{K}{6}$ and $K_{ME} = \frac{B^2}{48c^o_{44}}$. Notice that in the absence of quadrupole effects (or at high temperatures), the free energy reduces to the strain energy alone, and χ_{EL} becomes

$$\chi_{EL} = 4\, c^o_{44} \qquad [6.18]$$

c^0_{44} in Eq. [6.13] is then interpreted as the high temperature value of the elastic constant and Eq. [6.17] rewritten as

$$c_{44}(T) = c^o_{44}\, \left(\frac{1-K_Q\chi_Q - K_{ME}\chi_Q}{1 - K_Q\chi_Q}\right) \qquad [6.19]$$

If the ground state is degenerate, then $\chi_Q = C/T$ (where C is a constant containing the sum over the matrix elements) and Eq. [6.19] can be expressed in the familiar form

$$c_{44}(T) = c^o_{44}\, \left(\frac{T - T_Q - T_{ME}}{T - T_Q}\right) \qquad [6.20]$$

where $T_Q = \frac{1}{6}$ KC and $T_{ME} = \frac{1}{48}\ \frac{B^2C}{C^o_{44}}$.

The behaviour of the c_{44} elastic constant near T_c has been measured in all three chalcogenides (in US, by du Plessis and Tillwick, 1979: in USe and UTe, by Neunschwander et al, 1986); the c_{44} elastic constant softens as the transition temperature is approached, in a manner consistent with Eq. [6.20]. The lattice quadrupole parameters, K, B and c^o_{44} (or alternatively, K_Q, K_{ME}, and c^o_{44}) must be chosen so as to reproduce the observed softening of $c_{44}(T)$.

6.5 Low Temperature Ordered Phase

In the ordered phase, $\langle S^z\rangle$, $\langle O^0_2\rangle$ and the strain, ε, are non-zero. By minimizing the energy with respect to the strain, the strain can be eliminated from the Hamiltonian, and replaced with

$$\varepsilon = \frac{\sqrt{3}}{24}\ \frac{B}{c_{44}}\ \langle O_2^0\rangle \qquad [6.21]$$

(Appendix A.3). The Hamiltonian becomes

$$H^{MF} = H_{CF} - 2J\langle S^z\rangle S^z - \left(\frac{1}{48}\ \frac{B^2}{c_{44}} + \frac{1}{6}K\right)\ \langle O_2^0\rangle\ O_2^0 \qquad [6.22]$$

(where the constant terms have been dropped for clarity). Assuming that at low temperatures the elastic constant, c_{44}, is approximately c^0_{44},

$$H^{MF} = H_{CF} - 2J\langle S^z\rangle S^z - (K_Q + K_{ME})\ \langle O_2^0\rangle\ O_2^0 \qquad [6.23]$$

Because $\langle S^z\rangle$ and $\langle O_2^0\rangle$ appear in the Hamiltonian, the eigenvectors and eigenvalues of the low temperature problem must be determined self-consistently.

The parameters J, K_Q, and K_{ME} must produce a set of single ion levels consistent with the ordered moment, $g\mu_B\langle S^z\rangle$, with the magnetic excitation spectrum (the calculation of which is described in Appendix B), and the magnitude of the distortion in the ordered phase. (Appendix A.4).

6.6 f^3 Ground State

The best description of the low temperature behaviour is obtained assuming an f^3 configuration. The Hund's rule ground state of an f^3 electronic configuration is ${}^4I_{9/2}$. In the presence of a cubic crystal field, the ten-fold degenerate ground state is split into $\Gamma_8^{(1)}$ and $\Gamma_8^{(2)}$

quartets and a Γ_6 doublet. The observed properties of the UX compounds are best reproduced for a $\Gamma_8^{(2)}$ quartet ground state isolated from the other multiplets by a large energy splitting.

The effect of applying mean exhange and quadrupolar fields (to the relevant $\Gamma_8^{(2)}$ quartet) is shown in Figs. 6.1 and 6.2, using the (x,W) parameters appropriate to USe. In the absence of quadrupolar interactions, the mean exchange field splits the quartet as shown in Fig. 6.1. The measured paramagnetic response and ordered moment are best fit for an exchange constant, $J \approx 0.47$, (corresponding to the mean field H_0). The low temperature excitation spectrum however is not reproduced. The dipole transition operators and transition matrix elements within the quartet are also shown on Fig. 6.1. The strongest matrix element couples the ground and first excited states. At H_0, their splitting, (which corresponds to the (111) zone boundary excitation energy) is only of order 5 THz.

Figure 6.2 shows the change in the single ion levels (at x, W, and H_0) in response to a quadrupolar field. The ordered moment in the ground state, [illegible] well as the transition matrix elements are virtually unaffected by the field. The splitting can then, essentially, be tuned to reproduce the gap in the excitation spectrum. In USe, the measured spectrum is best fit with the field, Q_0, shown in Fig 6.2.

Table 6.1 lists the observed magnetic properties of all three chalcogenide compounds as well as their calculated values obtained from fitting the (x, W, J, K_Q, K_{ME}) parameter set to the observations. In US and USe, the agreement is quite good: the static properties are

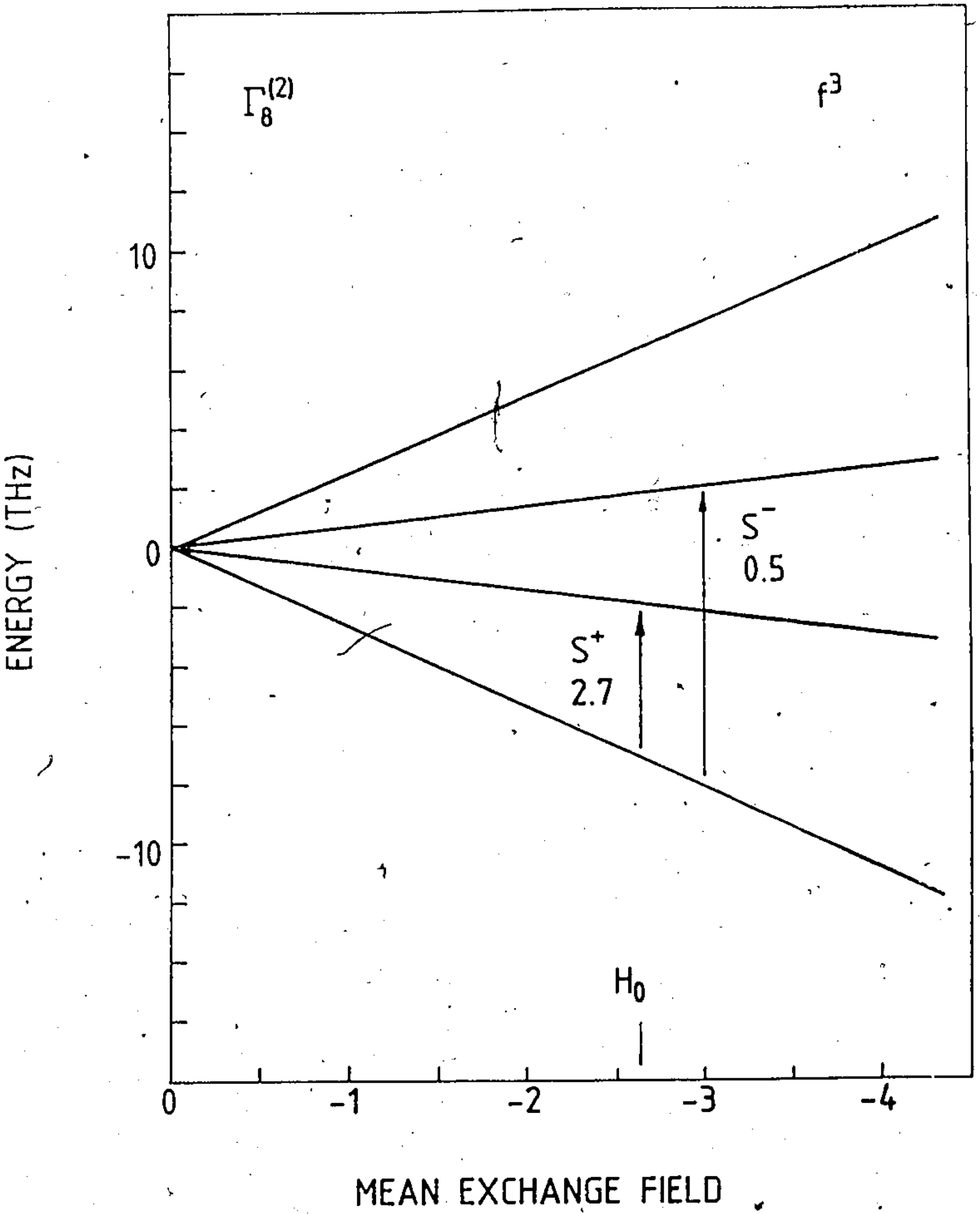

Fig. 6.1 Energy splitting of the $\Gamma_8^{(2)}$ quartet by the mean exchange field. The allowed transitions out of the ground state (and the associated transition matrix elements) are shown. H_0 is the value of the mean field which best reproduces the static properties of USe.

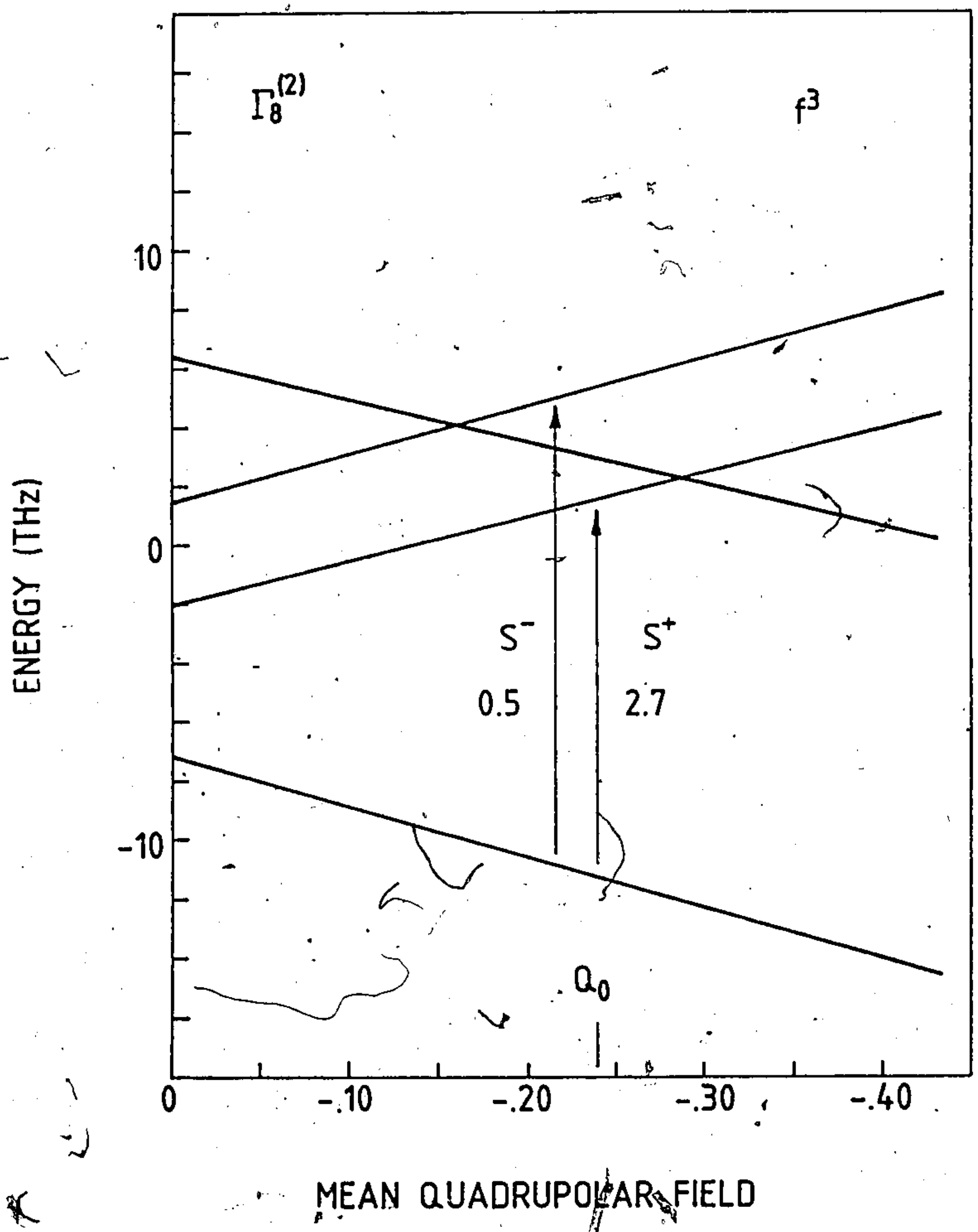

Fig. 6.2 Energy splitting of the (mean-field-split) $\Gamma_8^{(2)}$ quartet by the mean quadrupolar field. Q_o is the value of the mean quadrupolar field which best reproduces the observed anisotropy gap in USe.

Table 6.1 Comparison of the uranium chalcogenide observables to those predicted by the f^3 localized electron model. The model parameters for each fit are shown in the lower half of the table.

	US		USe		UTe	
	EXP	MODEL	EXP	MODEL	EXP	MODEL
T (K)	180.0±5.0	180.0	165.0±5.0	167.0	110.0±5.0	116.0
μ_{eff} (μ_B)	2.25±0.1	2.1	2.5±0.1	2.4	2.6±0.2	2.6
$\langle\mu\rangle$ (μ_B)	1.70±0.03	1.70	2.0±0.1	2.07	2.25±0.05	2.19
T_Q (K)	162.0±10.0	162.0	149.0±3.0	149.0	103.0±1.0	40.0
T_{ME} (K)	2.0±1.0	3.0	1.4±0.3	1.5	1.0±0.1	1.0
Δ_{60} (mrad)	8.0±2.0	6.0	6.0±2.0	4.0	5.0±1.0	3.0
$\omega_{q=0}$ (THz)	10.0±1.0	10.0	9.4±0.3	9.4	3.5±0.1	3.54
x	-0.526		-0.63		-0.66	
W	-10.4		-12.8		-50.0	
J_o (THz)	0.67		0.47		0.29	
K_Q (THz)	0.024		0.013		0.003	
K_{ME} (THz)	0.0003		0.00013		0.00008	
c^o_{44} (THz/f.u.)	1075.0		1059.0		1108.0	

well reproduced and the energy scale of the quadrupole interaction (reflected in T_Q) is consistent with the anisotropy energy needed to account for the large zone centre gap in the magnetic excitation spectrum. In UTe, however, although the magnetic properties can be fit quite well, the quadrupole interaction energy needed to describe the zone centre anistropy of the dispersion is considerably smaller than what would be anticipated from the elastic constant measurement.

Table 6.1 also shows the model parameters responsible for each fit. As expected from the variation of the critical temperatures, the exchange constant is largest in US and smallest in UTe. The quadrupolar interaction parameter varies in the same way, consistent with the zone centre anisotropies and magnitude of the distortion in the ordered phase.

The most unusual features of the USe excitation spectrum are that the excitations have intrinsic widths and are unpolarized. Neither of these features can be explained within the local moment framework. The former, at least, is to be expected; there is no inherent mechanism in such a model for producing a damped response. It is possible, of course, to introduce damping from an 'external' influence. A model involving coupling to the conduction electrons is discussed in the next section, and is shown, at least qualitatively, to describe the data. In this simple model however, the underlying polarization of the excitation is unchanged. From Fig. 6.2, it is clear that the f^3 model presented here predicts only transverse excitations.

6.7 f-d Model

In order to produce a damped response in the local moment system, it is necessary to couple the sharp excitations to a broader continuum of excitations, such as the continuum of conduction electron-hole states. A simple model of conduction electron damping was discussed by Buyers and Holden (1985). Within the approximations, the model produces an analytic form for the response function which can be directly compared with experiment.

The model assumes that the single-ion response of the f-electron system arises from transitions between the magnetic ground state and a single excited state, Δ. Each ion is coupled to its neighbours via a Heisenberg interaction and to the conduction d-electron spin through an interaction of the form $\vec{S} \cdot \vec{\sigma}$. The model Hamiltonian is then

$$H = \sum_{\vec{k}} E_{\vec{k}} c^{+}_{\vec{k}} c_{\vec{k}} + \sum_{i} \sum_{n} E_{ni} f^{+}_{ni} f_{ni} + J_{ff} \sum_{ij} \vec{S}_i \cdot \vec{S}_j + J_{df} \sum_{i} \vec{S}_i \cdot \vec{\sigma}_i \quad [6.24]$$

c^{+}_{k} and c_k are conduction electron creation and annihilation operators (respectively). The operator f^{+}_{ni} creates the single ion state $|n\rangle$ at site i. J_{ff} is the inter-ion coupling and J_{df} the on-site coupling to the conduction electron band.

The f-response and the d-response are described, respectively, by the Green's functions

$$G^{\alpha\beta}_{ij} \propto \theta(t) \langle [S^{\alpha}_{i}(t), S^{\beta}_{j}(0)] \rangle$$
$$D^{\alpha\beta}_{i} \propto \theta(t) \langle [\sigma^{\alpha}_{i}(t), S^{\beta}_{i}(0)] \rangle \quad [6.25]$$

where S^{α} designates one component of the spin operator (i.e., S^{+}, S^{-}, or S^{z}). It is possible to obtain the equations of motion for $G^{\alpha\beta}_{ij}$ and $D^{\alpha\beta}_{i}$

within the random phase approximation. The Fourier transformed results are

$$G^{\alpha\beta}(\vec{q},\omega) = g^{\alpha\beta}(\omega) + g^{\alpha\beta}(\omega)\; J_{ff}(\vec{q})\; G^{\alpha\beta}(\vec{q},\omega) + g^{\alpha\beta}(\omega)\; J_{df}(\vec{q})\; D^{\alpha\beta}(\vec{q},\omega) \qquad [6.26]$$

$$D^{\alpha\beta}(\vec{q},\omega) = d^{\alpha\beta}(\omega)\; J_{df}(\vec{q})\; G^{\alpha\beta}(\vec{q},\omega)$$

$g^{\alpha\beta}$ is the single-ion response function, i.e. the response function for the f-electron system in the absence of coupling to the other ions. For this simple two level system, it is given by

$$g^{\alpha\beta}(\omega) = \frac{\gamma^2}{\omega - \Delta} \qquad [6.27]$$

where γ is the matrix element for the transition. $d^{\alpha\beta}$ is the equivalent conduction electron function. It is assumed that the conduction electrons will show some broad response in energy that can be described by

$$d^{\alpha\beta}(\omega) = \frac{1}{i\omega - \Gamma} \qquad [6.28]$$

From Eqs. [6.26], it can be seen that the effect of the interaction with the conduction electrons is to renormalize the f-electron response such that

$$G^{\alpha\beta} = \frac{g^{\alpha\beta}}{1 - J_{ff}\, g^{\alpha\beta} - g^{\alpha\beta}\, J_{df}\, d^{\alpha\beta}} \qquad [6.29]$$

(where the q and ω indices have been omitted for convenience). The imaginary part of $G^{\alpha\beta}$ (i.e. the part which enters into the neutron scattering cross section) is then

$$\mathrm{Im}\, G^{\alpha\beta} = \frac{-\gamma^4 J_{df}^2 \dfrac{\omega}{\omega^2+\Gamma^2}}{\left(\omega - \Delta_q + \gamma^2 J_{df}^2 \dfrac{\Gamma}{\omega^2+\Gamma^2}\right)^2 + \left(\gamma^2 J_{df}^2 \dfrac{\omega}{\omega^2+\Gamma^2}\right)^2} \qquad [6.30]$$

where $\Delta_q = \Delta + \gamma^2 J_{ff}$. In calculating the response measured by neutron scattering, it is necessary to include the contributions from both $G^{\alpha\beta}$ and $G^{\beta\alpha}$. The solid line in Fig. 6.3 is a fit of the model to the USe zone centre response. The fit parameters are inset.

From Eq. [6.30], it can be seen that the single-ion excitation energy, Δ, is renormalized by both the f-f and the f-d exchange. Although there is no longer a δ-function response at Δ, a sharp response is possible in the limit of weak conduction electron coupling, i.e. $J_{df} \ll \Delta_q$. As the f-d exchange is increased, the peak near Δ_q broadens and decays into an apparent continuum of excitations. This is shown and specifically compared to the response in US by Buyers (1985). The model then has the scope to describe the range of dynamic behaviour observed in the UX compounds. It provides a physically appealing mechanism for the systematics of the damping consistent with band structure results which suggests that the f-d interaction increases as the lattice constant decreases. In UTe, where the coupling is least, the spin response is local-moment-like, whereas in US the f-d exchange is sufficiently large that pronounced damping effects are observed.

A number of calculations have been done for cerium systems in the limit of an almost localized 4f electron interacting weakly with a

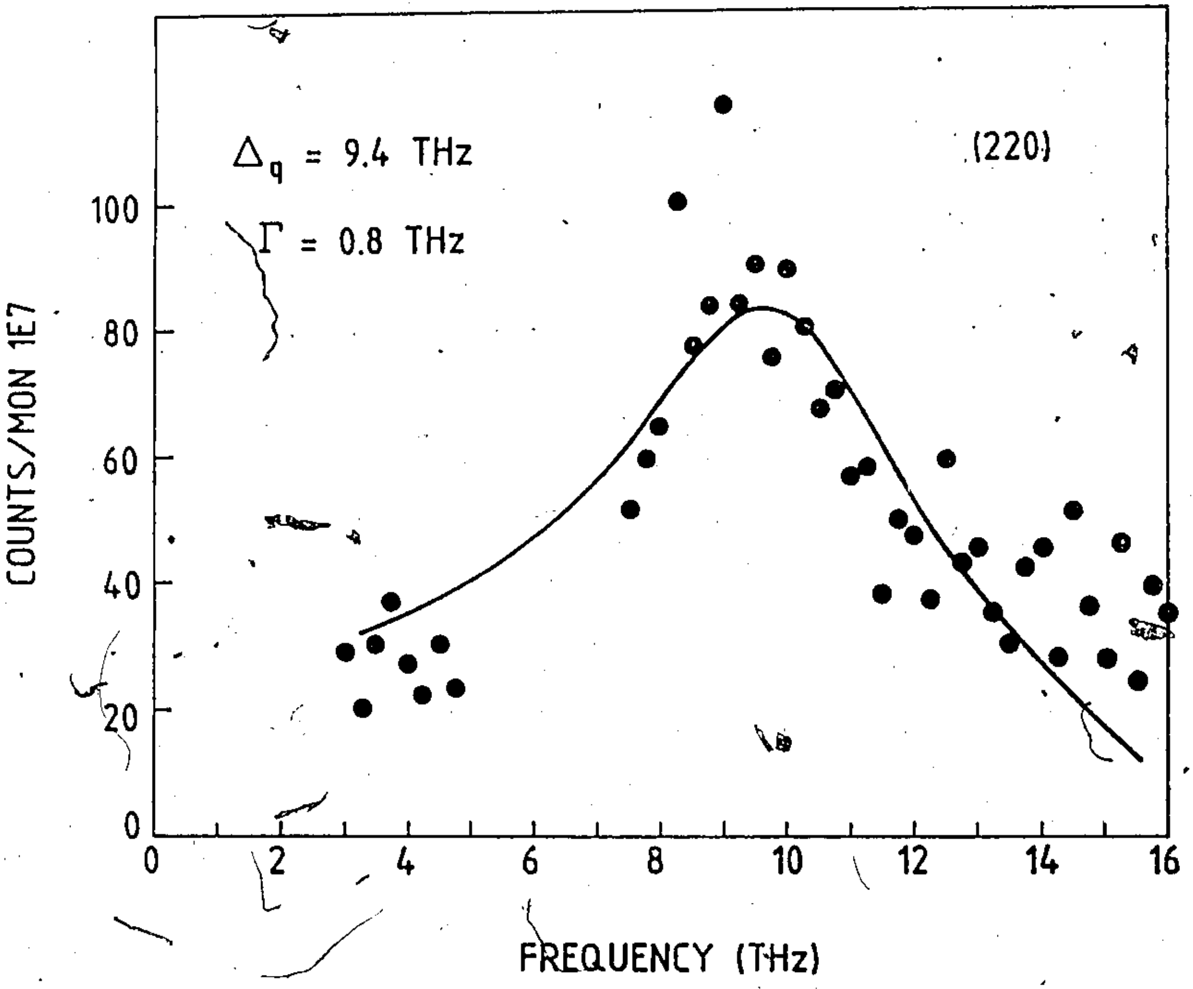

Fig. 6.3 Fit of the f-d electronic damping model (Eq. [6.30]) to the zone centre response in USe.

conduction electron band. Maekawa (1985) has calculated the effect of such an interaction on the single-ion dynamic susceptibility of Ce^{3+} in the context of the cubic Kondo system, $Ce_xLa_{1-x}Al_2$. The f-d mixing renormalizes the energies of the single ion crystal field levels and induces broadening. This leads to inelastic response in the dynamic susceptibility which has an intrinsic width.

Cooper et al (see Cooper, 1985 and references therein) have done extensive calculations in the cerium antiferromagnetics and shown the weak hybridization approach to be successful in describing their static magnetic properties. Most recently, Hu and Cooper (1988) have calculated the temperature dependent inelastic response in the low temperature antiferromagnetic phase of CeBi and CeSb, using the hybridization as the damping mechanism. They find a broadened response with significant renormalization of the undamped single ion levels.

It should be noted that Eq. [6.30] also gives rise to a sharp response in the limit of a large d-electron bandwidth, i.e. $\Gamma \gg \Lambda_q$. The fit of the USe zone centre data gives a bandwidth of the order of a few meV whereas a realistic bandwidth might be expected to be about an eV. The model then requires some structure in the d-electron density of states on the scale of the magnetic excitation energies. It was pointed out by Buyers (1985) that it is possible for f-d hybridization to induce structure on this scale in the case of valence fluctuating systems (Fedro, 1981). This is quite a different situation, however, than the localized weak hybridization models discussed here.

CHAPTER 7: MAGNETIC CRITICAL SCATTERING IN USe

7.1 Critical Phase Transitions

Many magnetic phase transitions, including the paramagnetic to ferromagnetic transition belong to the class of phase transitions known as 'critical' or 'continuous'. Much progress has been made in the last 20 years in understanding and describing the physics of the critical phase transition largely due to the advent of two concepts — universality and scaling. Universality asserts that the behaviour of a critical system is independent of the details of the interaction between its components and is the same for any systems which share a small number of common features which delineate their 'universality class'. Magnetic systems have thus played an important role in the study of continuous phase transitions: the simple form of the magnetic Hamiltonian has lent itself to theoretical investigation while the wide variety of magnetic systems available for study in different universality classes have proven a valuable testing ground for theoretical predictions.

A continuous phase transition is characterized, on a microscopic level, by having large fluctuating regions of one phase imbedded in the other at temperatures near to the critical temperature (T_c). Consider, for example, a paramagnetic to ferromagnetic phase transition. As the critical temperature is approached from above ($T > T_c$) the interaction energy between the spins becomes more and more important.

The spins stop behaving independently and large fluctuating regions of highly correlated spins form within the paramagnetic phase. Similarly as T_c is approached from below, patches of disordered spins begin to appear against the general background of long range order. In either case as T gets closer and closer to T_c, the extent of the fluctuating regions increases, and at T_c diverges.

On a macroscopic level, the phase transition is characterized by large changes in certain thermodynamic observables. The specific heat and susceptibility diverge as $T \to T_c$ and a net magnetization appears. It is experimentally observed that these quantities exhibit power law variations as a function of temperature in the critical regime.

The essential features of the transition are described by scaling theory. The mathematical foundation of scaling was laid by Widom (1965) and by Domb and Hunter (1965) and a physical interpretation was provided later by Kadanoff (1966). The essence of scaling is that for a temperature near T_c, there is a single relevant length scale, ζ, known as the correlation length. The correlation length represents the maximum size of the fluctuating regions of 'other' phase in the main phase. (As $T \to T_c$ it is this quantity which diverges.) Because the temperature is characterized by a single length scale, a change of length scale is equivalent to a change of temperature. In mathematical terms, this means that the correlation length can be described in terms of a class of functions known as generalized homogeneous functions. Widom and Domb and Hunter suggested that near T_c the thermodynamic potentials can all be described by functions of this form.

The scaling hypothesis predicts the observed power law behaviour in the bulk properties of a critical system. The relevant observables in a magnetic system are the magnetization (M), the static susceptibility ($\chi_{q=0}$), and the correlation length. Their temperature dependence in the critical regime is defined in terms of the dimensionless reduced temperature, t, given by

$$t = \frac{T - T_c}{T_c} \qquad [7.1]$$

In standard notation, these power law functions are written

$$M \propto \begin{cases} (-t)^{\beta} & t < 0 \\ 0 & t > 0 \end{cases}$$

$$\frac{\chi_{q=0}}{\chi_0} \propto \begin{cases} t^{-\gamma} & t > 0 \\ (-t)^{-\gamma'} & t < 0 \end{cases} \qquad \text{where } \chi_0 = \frac{(g\mu_B)^2\, S(S+1)}{3kT} \qquad [7.2]$$

$$\zeta \propto \begin{cases} t^{-\nu} & t > 0 \\ (-t)^{-\nu'} & t < 0 \end{cases}$$

where the quantities β, γ, and ν are known as critical exponents. Scaling does not actually predict the magnitude of the critical exponents. It does, however, predict certain relationships between them such that, within a universality class, any two exponents are sufficient to determine all of the remaining exponents. Exponents must be calculated from microscopic theories. There are very few universality classes for which exact solutions for the critical exponents are available but between these solutions, approximate solutions, and experimental measurements, the exponents associated with a variety of transitions are known. Measurements of critical exponents thus lead to information about the universality class of the system under study.

A more detailed discussion of scaling and universality can be found in Appendix C.

7.2 Critical Behaviour of the UX Compounds

There has been some previous work on the critical behaviour of the ferromagnetic UX compounds, however no clear picture of the transition has emerged. The exponent γ has been measured in UTe (Aldred, 1980) and US (Tillwick, 1976) and found to be 1.3 in both materials. This is in the range of the standard 3-dimensional models (1.24 for the Ising model and 1.38 for the Heisenberg model). The exponent β has been measured in all three compounds and is somewhat anomalous. The neutron scattering measurements of Aldred et al (1980) in UTe yield a value of β of about 0.29 which is somewhat smaller than the exponents of the standard 3-dimensional models ($\beta \approx 0.31$-0.37). du Plessis et al (1982) performed similar measurements on USe and observed a temperature dependence of the magnetization consistent with a power law variation but with an unusually small exponent of 0.24. Magnetization measurements on US (Tillwick, 1976) gave an exponent of about 0.55. However it was suggested by Aldred et al (1980), who attempted a similar measurement on UTe, that this determination may be unreliable because of the rapid variation of the magnetization with magnetic field at low fields. Finally, Bjerrum Moller et al (1979) investigated the spatial correlations in UTe and found an unusually large value of ν at 0.84.

7.3 Critical Scattering in the Paramagnetic Phase

Neutron scattering is a powerful technique with which to examine the behaviour of a magnetic system near its critical point because it is able to probe both the length scale and time scale of the fluctuations which characterize the critical regime. It can provide a direct measure of many of the relevant observables including the magnetization, the (inverse) correlation length and the wave vector and frequency dependent susceptibility. In this section a brief description of the measurement and its interpretation is given.

The observable in a neutron scattering measurement is the scattering function $S(\vec{q},\omega)$. The simplest functional description of $S(\vec{q},\omega)$ in the critical regime is the double Lorentzian form first proposed by Van Hove (1954), which can be expressed as

$$S(\vec{q},\omega) = \frac{1}{\pi}\left(\frac{\chi_{q=0}}{\chi_0}\right) \frac{\kappa_1^2}{\kappa_1^2 + q^2} \frac{\Gamma(q)}{\Gamma^2(q) + \omega^2} \qquad [7.3]$$

It is convenient to introduce the parameter κ_1, the inverse correlation length ($\kappa_1 = 1/\zeta$). The function $\Gamma(q)$ is known as the dynamic width; $\Gamma(q)$ measures the energy scale of the spin fluctuations in the same way that κ_1 measures their (inverse) length scale. A more detailed discussion of the origin of Eq. [7.3] can be found in Appendix D.1.

In order to extract $\chi_{q=0}/\chi_0$ and κ_1 from a neutron measurement, it is not necessary to examine the full q and ω dependence of the scattering. Consider instead the energy integrated form

$$S(\vec{q}) = \int d\omega \, S(\vec{q},\omega) \qquad [7.4]$$

Equation [7.3] reduces to

$$S(\vec{q}) \propto \left(\frac{\chi_{q=0}}{\chi_0}\right) \frac{\kappa_1^2}{\kappa_1^2 + q^2} \qquad [7.5]$$

Thus the critical scattering takes the form of a Lorentzian centred on the ordering wave vector, q = 0 . According to scaling, as $T \to T_c$, the width of the Lorentzian decreases as

$$\kappa_1 \propto t^{\nu} \qquad [7.6]$$

while its coefficient diverges as

$$\frac{\chi_{q=0}}{\chi_0} \propto t^{-\gamma} \ , \qquad [7.7]$$

In principle $S(\vec{q})$ can be determined by measuring $S(\vec{q},\omega)$ with a triple-axis spectrometer and integrating over all ω. It is possible however, to measure $S(\vec{q})$ approximately, but more directly, in a two-axis measurement. By removing the analyzer, scattered neutrons of all energies are detected so that, in essence, the spectrometer performs the energy integration. The approximation involved is discussed more fully in Appendix D.2 but essentially amounts to the restriction that the energy scale of the critical fluctuations must be small compared to the neutron energy. The validity of this approximation is discussed in Sec. 7.11.

7.4 Critical Behaviour in the Ordered Phase

The critical temperature is characterized by the onset of long range magnetic order, and for temperatures below Tc, a magnetic Bragg peak which reflects the ordered moment of the system appears. As shown in Sec. 3.2 (Eq. [3.6]), the intensity of the magnetic Bragg peak, I_M, is proportional to the square of the magnetization and thus provides a direct measure of the critical exponent β, through

$$I_M \propto M^2 \propto (-t)^{2\beta} \qquad [7.8]$$

A detailed study of the critical scattering in the ordered phase is extremely difficult and has not been attempted here. For the purpose of interpreting the measurements however, it is necessary to point out that below T_c, scaling again predicts power law behaviour for the susceptibility and inverse correlation length (Eq. [7.2]). (In fact the susceptibility in the ordered phase is more complex because it has two distinct components, parallel (χ_{zz}) and perpendicular (χ_{xx}) to the magnetization direction. The power law refers to the parallel component). Thus as T falls below T_c, the inverse correlation length increases and the susceptibility decreases: the critical scattering becomes broader and weaker.

7.5 Details of the Experiment

The experiment was performed on the N5 triple axis spectrometer at the NRU reactor, Chalk River. Measurements of S(q) vs q were made in the two axis mode using a Si(331) monochromator at a fixed incident energy of 15 THz. Collimation before and after the sample was 0.2° and 0.5° respectively.

The sample was mounted on an aluminum base in a He cryostat. The temperature was controlled from a Si diode attached to the tail piece of the cryostat and measured from a second diode attached to the sample base. The best temperature stability which could be achieved was 0.005 K but a more typical value is 0.01 K.

The measurements were concentrated around the zone centre (111) which has the largest possible magnetic form factor and (because of the near cancellation of the U and Se scattering lengths) the weakest nuclear scattering. Measurements were made in a number of directions through q=0 as shown in Fig 7.1. (In the remainder of the text, the contours are designated by the following labels: Zeta $\|$(110), Eta$\|$(001), Transverse$\|$(11$\bar{1}$), Perpendicular $\|$(11$\bar{2}$)).

The background was measured in a series of scans at low temperature (100 K), sufficiently far from T_c that there should be no critical scattering contribution to the intensity there. The background was measured along the same trajectory and at the same statistics as the S(q) vs q measurements but over a range that extended out to the zone boundaries. A linear sloping background proved an adequate description. A second set of measurements at a temperature of about 172 K near the zone boundaries (i.e. well away from the critical scattering) are entirely consistent with the low temperature measurements.

7.6 Resolution Correction

In order to extract the intrinsic scattering function from a measurement, it is necessary to correct for the instrumental resolution.

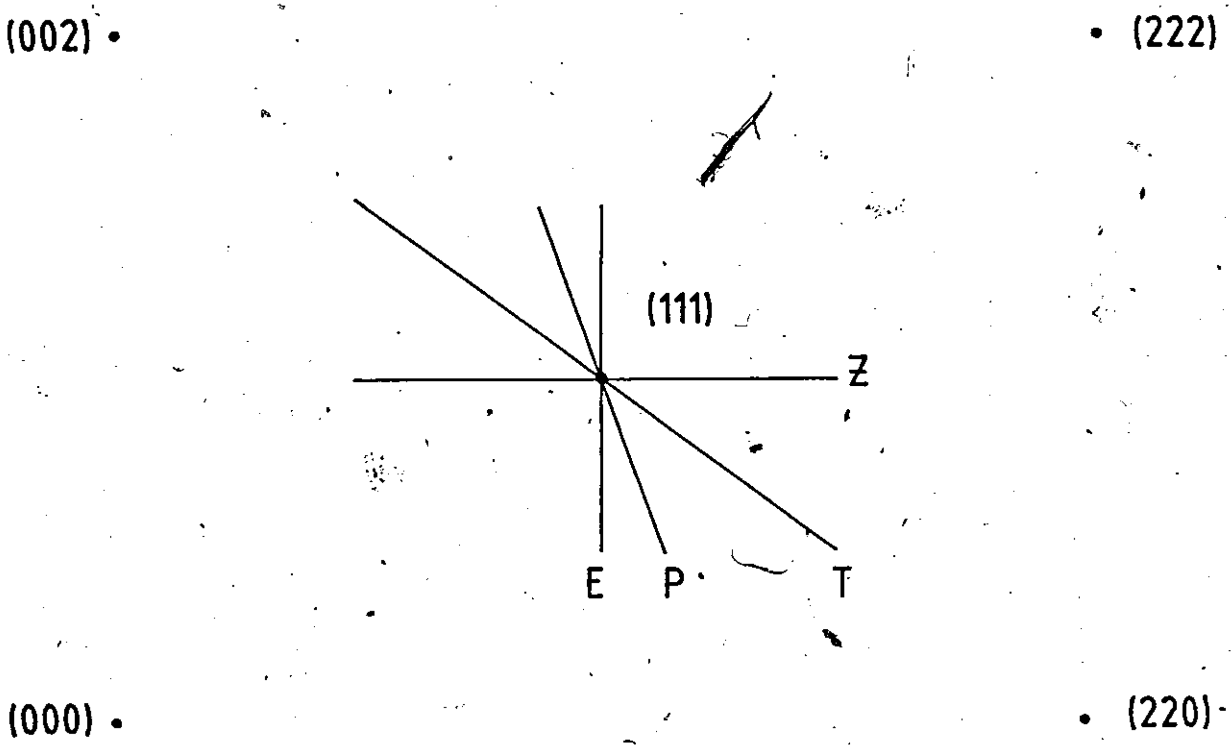

Fig. 7.1 Geometry of the critical scattering measurements. The scans are designated Z, E, T, and P in the text.

The in-plane Q resolution was measured at (111) in a series of scans through the nuclear Bragg peak. (The measurements were made at a temperature of 250 K where the signal is free from magnetic critical scattering). The measured resolution ellipse, defined as the half-height contour of the Bragg peak, is shown in Fig 7.2. The resolution function is calculated from the known angular divergences and monochromator mosaic assuming zero sample mosaic. The latter is then treated as an adjustable parameter which is varied in order to reproduce the measured contour. A mosaic of ≈ 0.13° is required to produce the solid curve.

The dimensions of the resolution ellipse are $0.003 \times 0.03 \times 0.08$ Å^{-1}. The largest axis of the ellipse is the vertical (i.e. out-of-plane) component and must be obtained from the calculated resolution function. In the scattering plane, the ellipse is oriented such that its longer axis is roughly parallel to $\vec{Q}$.

The convolution was performed by summing $S(Q,\omega) \cdot R(Q,\omega)$ across a grid extending out to 3 (Gaussian) standard deviations in each direction of the ellipse. The size of the grid was chosen such that increasing the number of steps further produced no appreciable change in the convoluted result. A typical integration grid was $12 \times 24 \times 60$ steps.

The scattering function, $S(q)$ (Eq. [7.5]), is obtained iteratively. A best guess at $S(q)$ is made, convoluted with the resolution function, and then compared to the measurement. The parameters describing $S(q)$ are then refined and the procedure repeated until the best fit to the data is achieved.

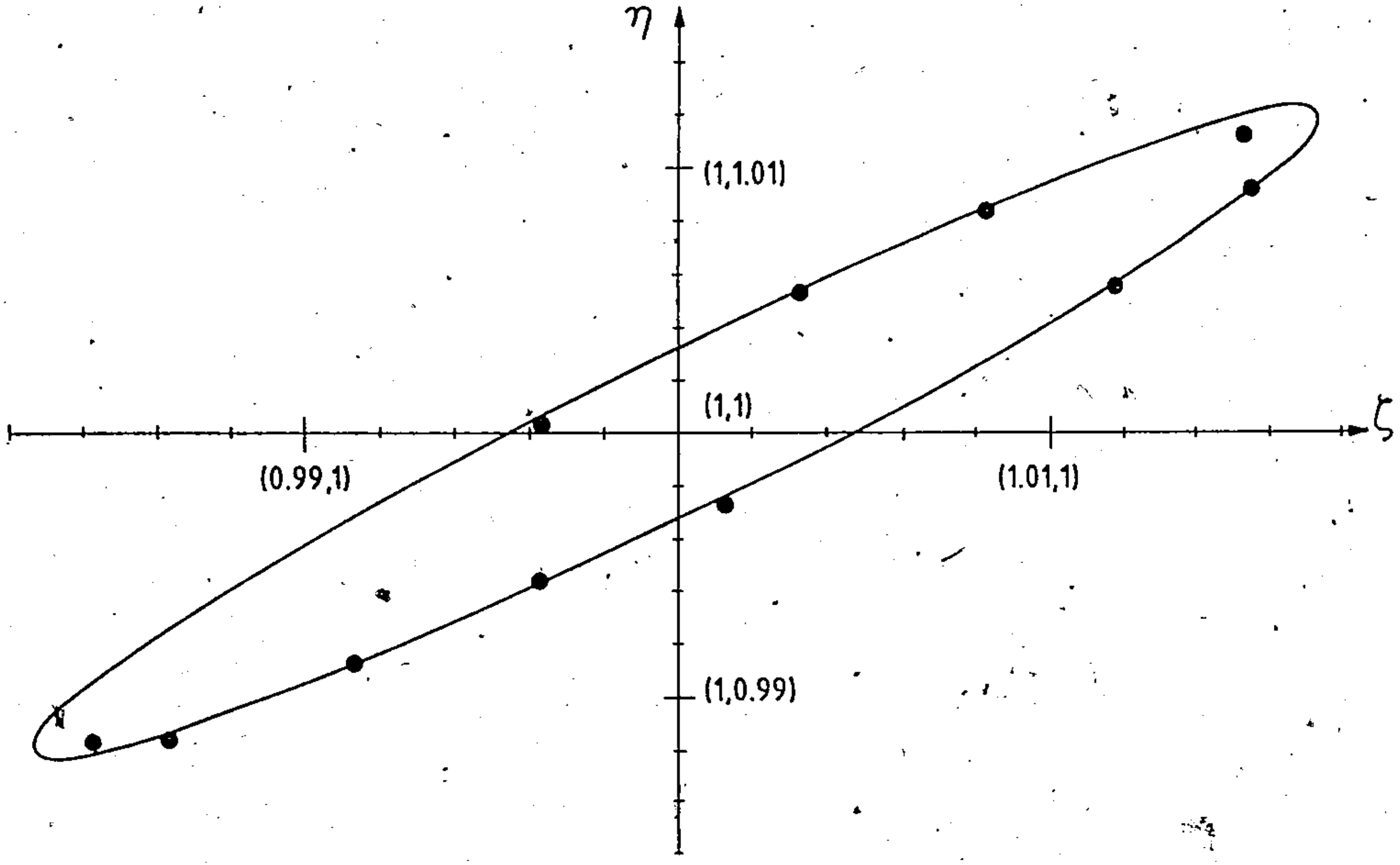

Fig. 7.2 The resolution ellipse in the scattering plane at the (111) Bragg peak position. (The axis is parallel to (110) and the axis to (001)). The points are measured and the solid line is calculated.

7.7 Determination of T_c

Figure 7.3 shows the variation in intensity of the (111) Bragg peak as a function of temperature in the critical regime. The intensity has been corrected for the contribution of the critical scattering, and reflects only the intensity of the resolution limited component of the scattering. The weak temperature independent contribution from the nuclear Bragg peak is shown. The inset expands the temperature range around 176 K where the magnetic component to the scattering appears.

Figure 7.4 shows, in the same temperature range, the intensity of the critical scattering at two points slightly offset from q=0. (Because of the presence and finite extent of the Bragg peak, it is impossible to observe directly the intensity of the critical scattering at that point). The measurement points to a critical temperature in the range 169-172 K.

It is clear from Figs. 7.3 and 7.4 that the onset of long range magnetic order occurs before the critical temperature is reached. These observations are inconsistent with the standard theory of a critical phase transition which sees a maximum in the susceptibility and the onset of long range order simultaneously at T_c. In fact, the behaviour of the order parameter is unusual: in order to describe the initial temperature variation with a power law, the exponent β must be greater than 1. Furthermore, there seems to be a discontinuity in the slope around 170 K, in the temperature range where the critical scat-

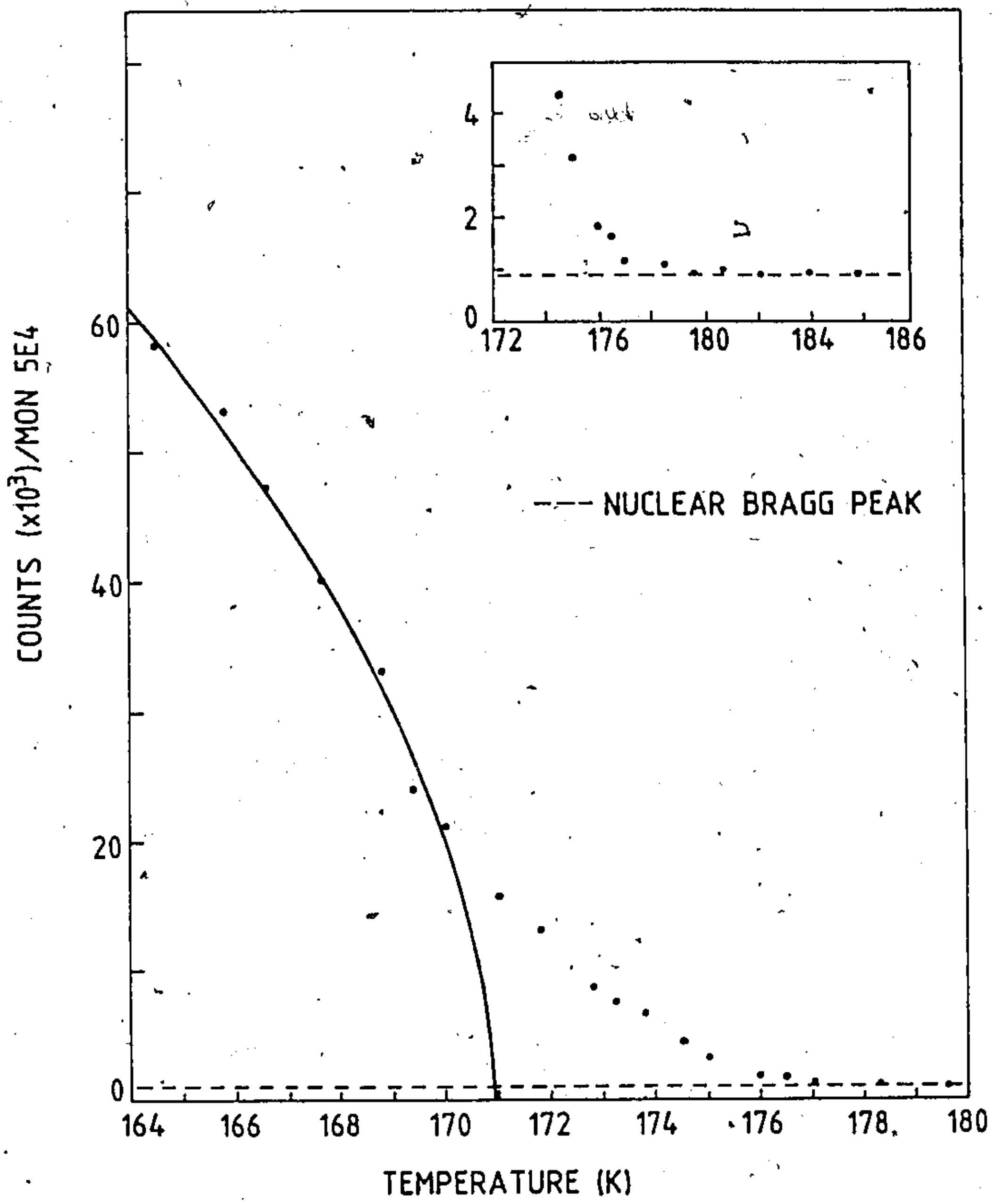

Fig. 7.3 The intensity of the (111) Bragg peak as a function of temperature in the critical regime. The dashed line is the contribution of the nuclear Bragg peak. The inset shows in more detail the onset of the long range magnetic order.

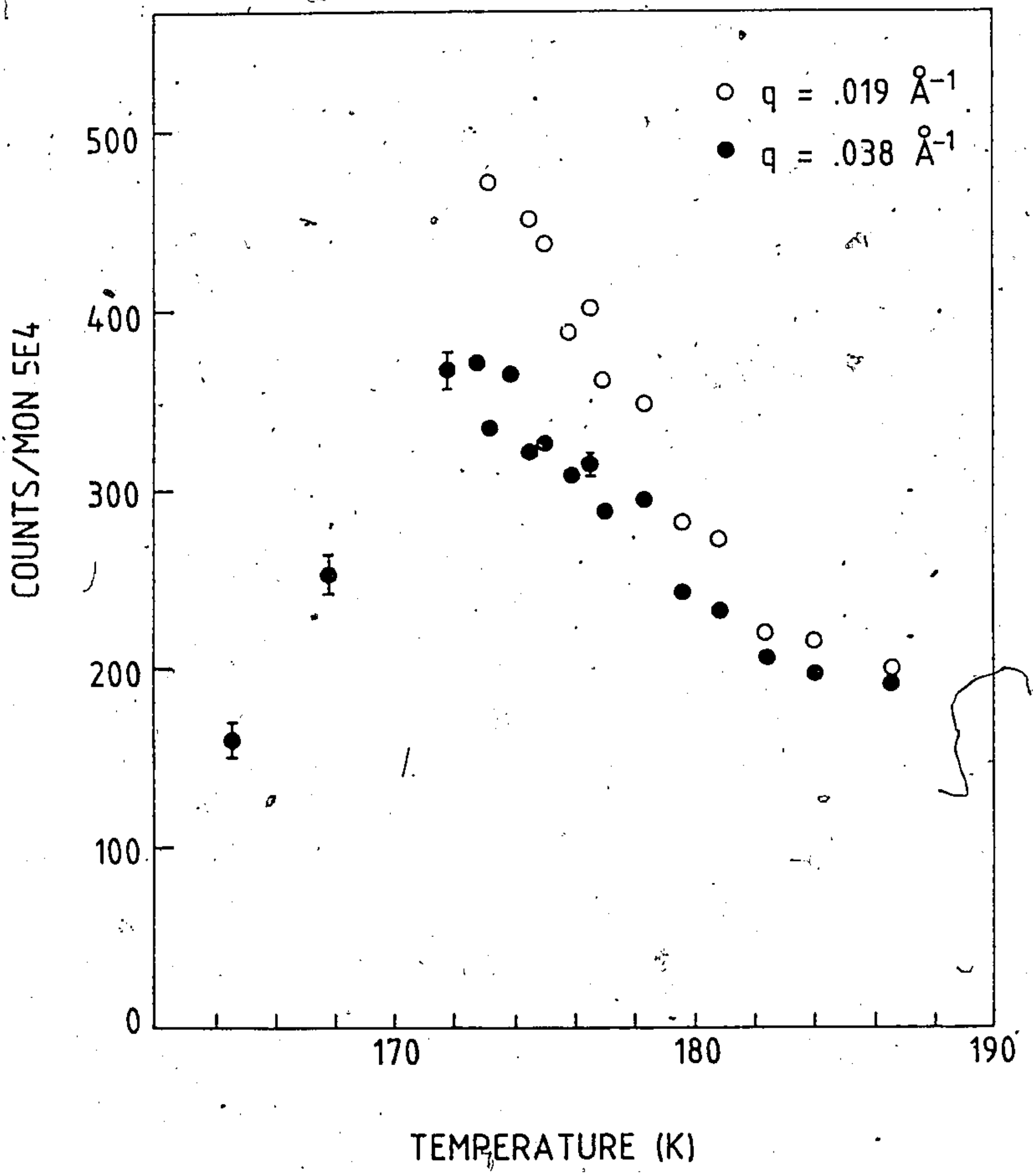

Fig. 7.4 The intensity of the critical scattering in the critical regime. The wave vectors are slightly offset from q=0 in order to avoid the scattering from the Bragg peak.

tering peaks. As will be discussed in Sec. 7.12, it is possible that the initial temperature dependence of the magnetization is a result of magnetostrictive effects. In this case, it might be argued that only the lower temperature points accurately reflect the order parameter of the transition. Rather than fitting to a power law over the entire temperature range, the solid line shows a fit to only the lowest temperature points (<171 K). The fit yields $T_c = 170.9 \pm 0.5$, $\beta = 0.28 \pm 0.05$.

7.8 Isotropic Nature of the Scattering

Figure 7.5 shows $S(q)$, measured in four different directions through the zone centre (111) at a temperature of 179.6 K. The static susceptibility and inverse correlation length which best describe each data set individually are given in table 7.1. Within the uncertainty on the fitted parameters, the correlation length is isotropic. Similar fits at temperatures both higher and lower than 179.6 K, confirm that there is no systematic variation of κ_1 with direction, and that even at the highest temperature (≈195 K), there is no significant anisotropy.

The solid line through the data points is the best fit line obtained by fitting all of the data together (TZEP). The dashed lines are the measured background.

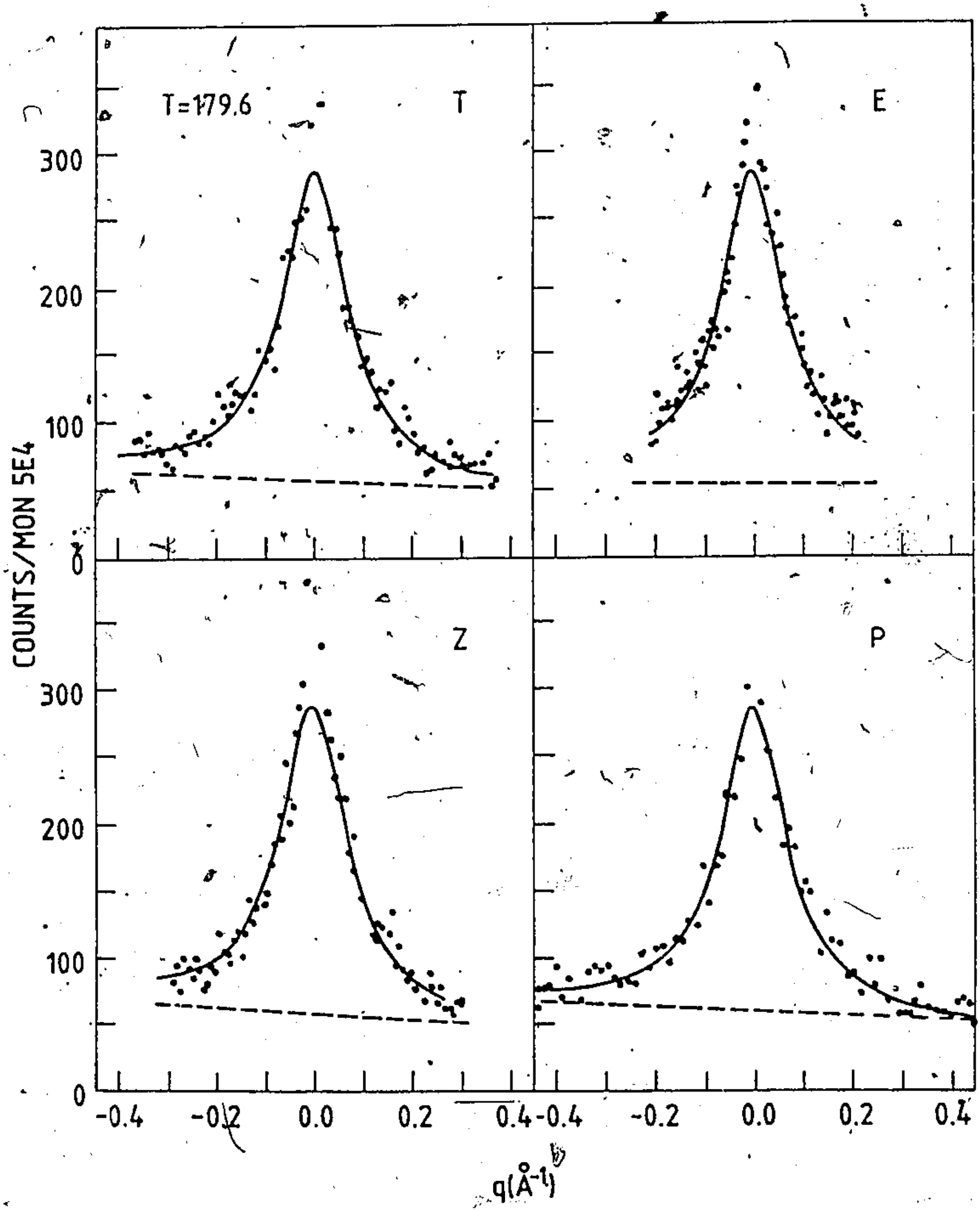

Fig. 7.5 Critical scattering at 179.6 K. The scattering along the four different trajectories through the zone centre (111) is shown. The solid line is the best fit to S(q) convoluted with the spectrometer resolution.

Table 7.1. Static susceptibility and inverse correlation length parameters which best describe the measurements at 179.6 K (see fig. 7.5). The 'TZEP' parameters result from a simultaneous fit to all four data sets.

	$\chi_{q=0}/\chi_0$	κ_1	χ^2
T	32.0 ± 3	0.0646 ± 0.002	0.90
E	31.6 ± 3	0.0656 ± 0.002	1.04
Z	33.4 ± 4	0.0617 ± 0.003	0.90
P	31.0 ± 4	0.0665 ± 0.003	1.12
TZEP	32.3 ± 2	0.0641 ± 0.002	1.02

7.9 Temperature Dependence of the Critical Scattering

The evolution of the critical scattering as a function of temperature is shown in figures 7.6(a) and (b). These correspond to measurements along (111)T. (It should be noted that there is a factor of two difference in the intensity axis scale between figures (a) and (b). It can be seen that as the temperature decreases towards the phase transition, the scattering becomes more strongly peaked around q = 0.

The solid lines are the best fits obtained by using all of the data available at a given temperature. The extracted inverse correlation length and static susceptibility are plotted as a function of temperature in Fig 7.7. (The inverse correlation length is plotted in dimensionless units as $a_{nn}\kappa_1$, where a_{nn} is the nearest neighbour U-U separation.) The closed circles correspond to data taken around the zone centre (111) and the open circles to data taken at the equivalent point (11$\bar{1}$).

The resolution correction at 190 K is negligible (that is, the observed width is the intrinsic width). As κ_1 decreases, the resolution correction becomes quite substantial: at 173 K, the observed

Fig. 7.6 (a), (b)
Evolution of the critical scattering as a function of temperature. The solid lines are the best fits to S(q) convoluted with the spectrometer resolution. Note that there is a factor of two difference in the intensity axis scale between (a) and (b).

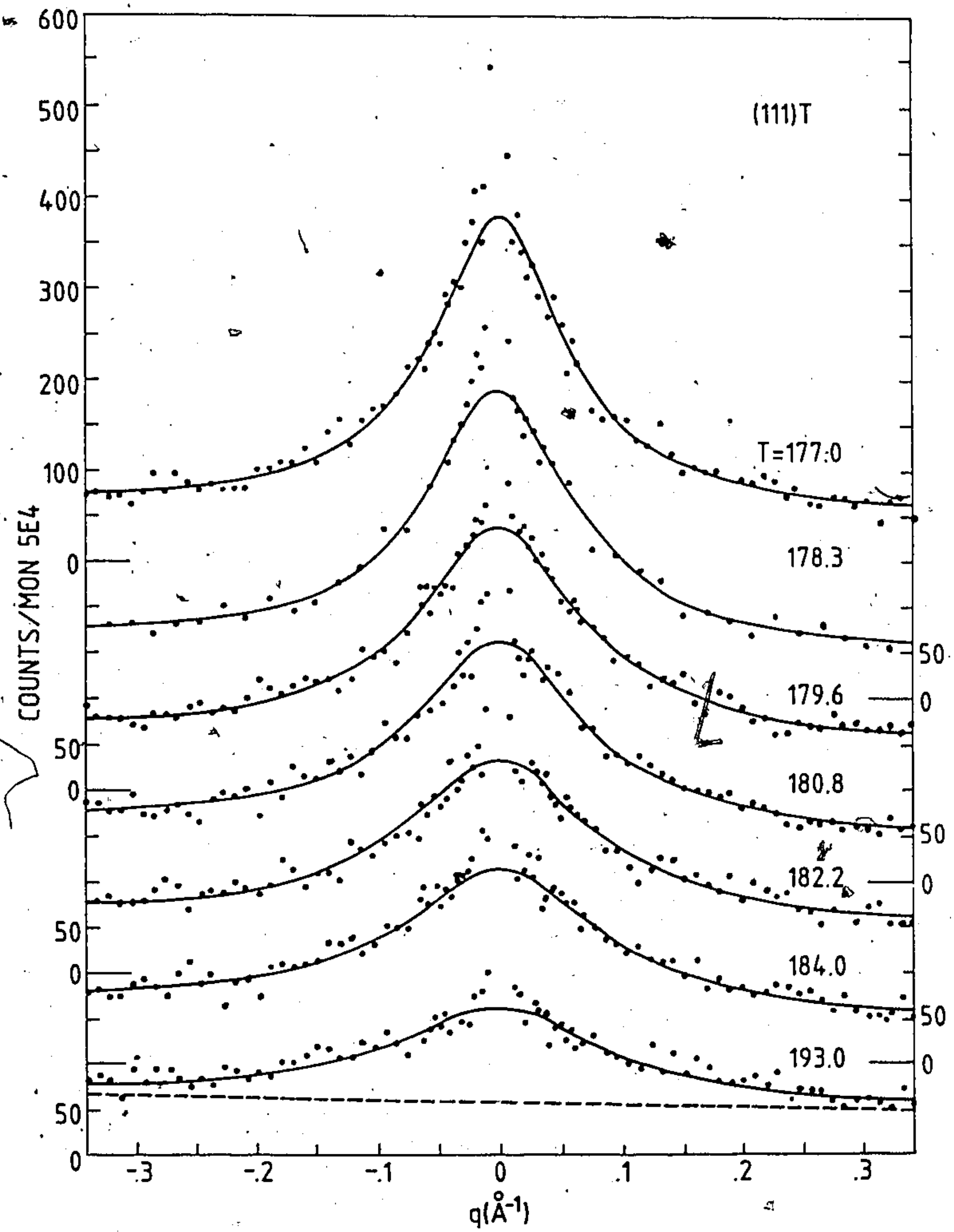
(111)T
COUNTS/MON 5E4
600
500
400
300
200
100
0
50
0
50
0
50
0
T=177.0
178.3
179.6
180.8
182.2
184.0
193.0
50
0
50
0
50
0
-.3
-.2
-.1
0
.1
.2
.3
q(Å^{-1})

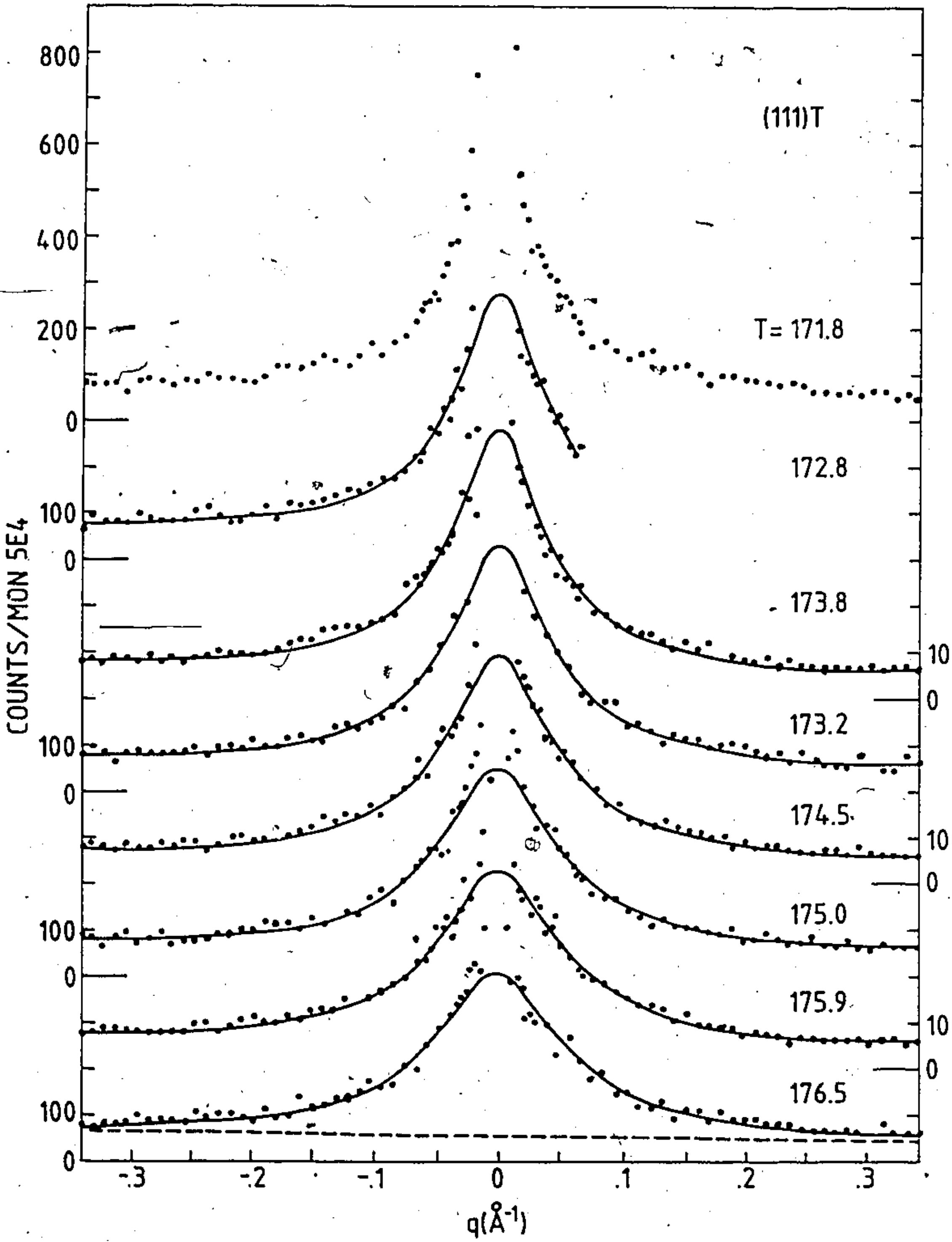
(111)T
T= 171.8
172.8
173.8
173.2
174.5
175.0
175.9
176.5
800
600
400
200
0
100
COUNTS/MON 5E4
-.3
-.2
-.1
0
.1
.2
.3
q(Å^{-1})

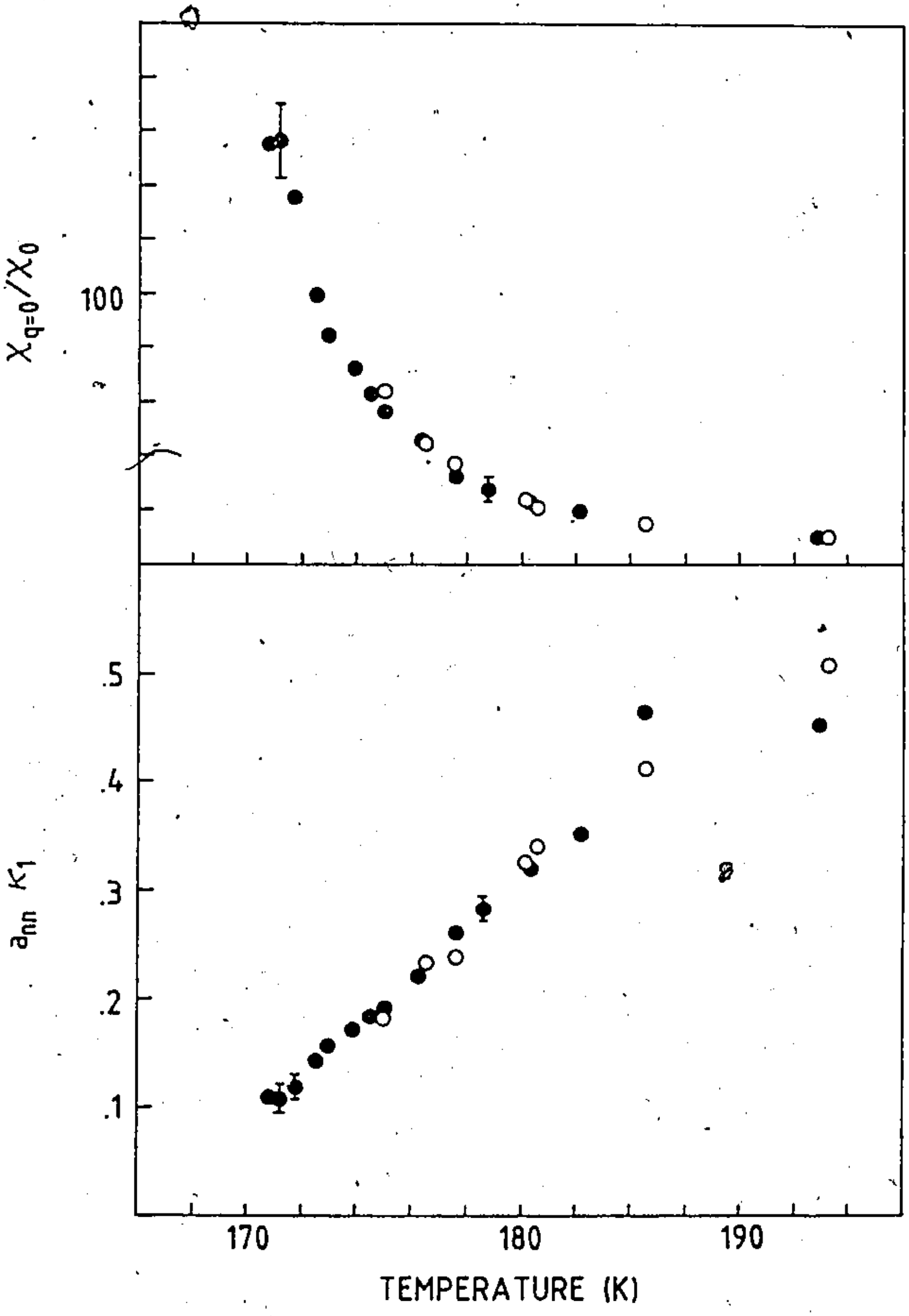

Fig. 7.7 Temperature dependence of the static susceptibility (top panel) and inverse correlation length (lower panel) in the critical regime.

width is approximately 1.8 times the intrinsic width. The relatively larger uncertainties at small t reflect the difficulty in resolving the Bragg peak from the critical scattering there.

7.10 Critical Exponents

The critical exponents are determined by fitting the inverse correlation length and static susceptibility to the power law functions, Eqns. [7.2]. The simplest approach is to allow both T_c and the exponent to vary in the fit. The inverse correlation length data alone yields

$$T_c^{\nu} = 170.5 \pm 0.9 \qquad \nu = 0.73 \pm 0.07$$

while the static susceptibility alone yields

$$T_c^{\gamma} = 169.5 \pm 1.0 \qquad \gamma = 1.57 \pm 0.2$$

In fact, there can be only one critical temperature. There is a strong correlation between fitted critical temperature and exponent so that in order to obtain a consistent description of the measurements, both exponents must be calculated for the same T_c. For example, at fixed critical temperatures of T_c^{ν} and T_c^{γ}, the fitted exponents are:

$$T_c^{\nu} = 170.5 \qquad \nu = 0.73 \pm 0.02 \qquad \gamma = 1.37 \pm 0.03$$

$$T_c^{\gamma} = 169.5 \qquad \nu = 0.81 \pm 0.03 \qquad \gamma = 1.57 \pm 0.03$$

Figures 7.8 and 7.9 are the standard log-log displays of inverse correlation length and static susceptibility as a function of reduced temperature for T_c^{ν} and T_c^{γ}. The solid lines are calculated from the fitted exponents.

From Fig. 7.4 the critical temperature must be in the range 170.5 ± 1.5 K. The lower panel of Fig. 7.10 shows the exponents ν, γ

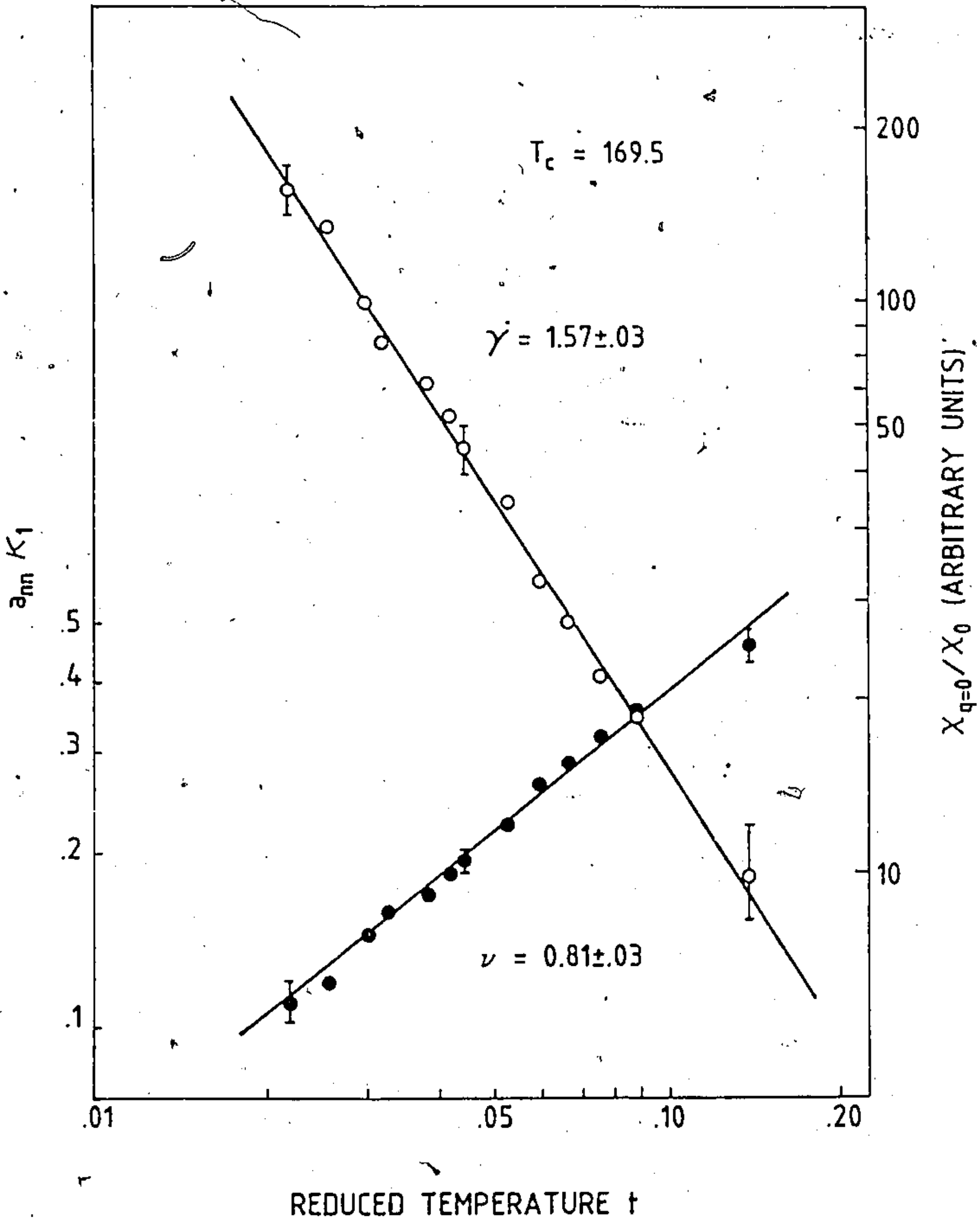

Fig. 7.8 Inverse correlation length and static susceptibility as a function of reduced temperature assuming a critical temperature of 169.5 K. The solid lines are calculated using the fitted exponents (shown).

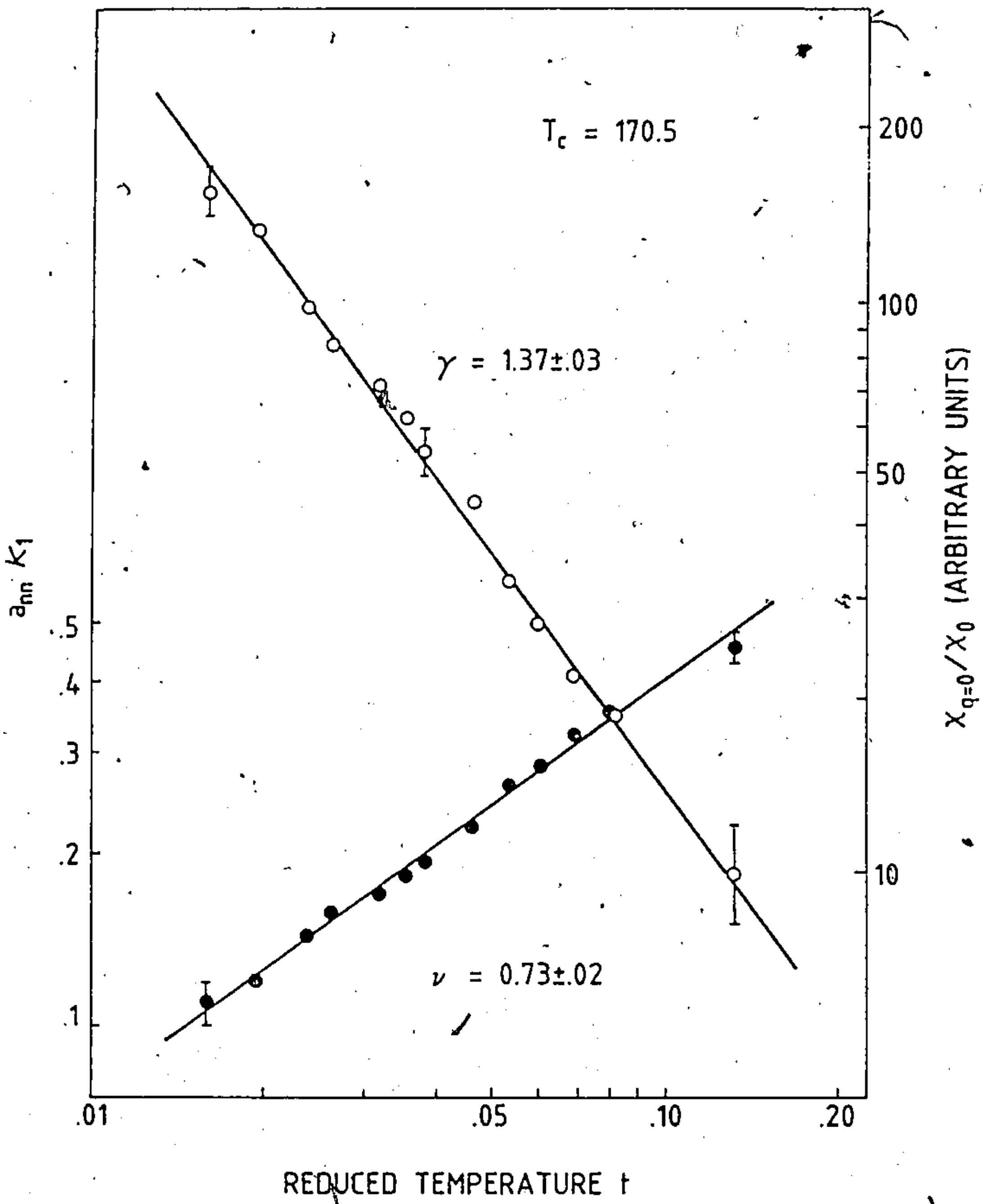

Fig. 7.9 Inverse correlation length and static susceptibility as a function of reduced temperature assuming a critical temperature of 170.5 K. The solid lines are calculated using the fitted exponents (shown).

and β calculated at fixed T_c over the entire range. ('A' and 'B' are two different calculations of the exponent β. 'A' is calculated as in Sec. 7.7, using only the measurements below 171 K: 'B' assumes a distribution of critical temperatures centred on a maximum, T_c. This calculation is discussed more fully in Sec. 7.12). At a given critical temperature the uncertainty on the fitted exponents is quite small (typically 0.02 in ν, 0.04 in γ, and 0.02 in β). Over the range however, the exponents vary approximately linearly with T_c. In the interval $T_c = 170.2 \pm 0.9$, over which the behaviour of the three observables are best described by the power law forms, the critical exponents are $\nu = 0.75 \pm 0.07$ and $\gamma = 1.43 \pm 0.20$, $\beta = 0.22 \pm 0.08$. For comparison, the critical exponents of the standard 3-dimensional Heisenberg model (3d-H) and the 3-dimensional Ising model (3d-I) are shown in Fig. 7.10. The fitted exponents are consistent (within two standard errors) with the Heisenberg model at a critical temperature of 170.6, very near to the critical temperature deduced from the inverse correlation length fit. The exponent β is significantly smaller than the Heisenberg value, but this is in agreement with the measurement of du Plessis (1982). The 3d-I model exponents are more consistent with a critical temperature of 171.3 K. This is a less likely solution because the susceptibility deviates from a power law description at the higher temperatures. It is clear, however, that without a better defined critical temperature, a unique determination of the exponents is not possible.

The top panel of Fig. 7.10 is a comparison to the scaling law

$$\gamma + 2\beta - d\nu = 0 \qquad [7.9]$$

Fig 7.10
Critical exponents ν, γ, and β as a function of critical temperature. (The β curves, 'A' and 'B', are calculated in two different ways. See the text for details.) The critical temperatures obtained from fitting each data set independently are shown as T_c^ν, T_c^γ, and T_c^β. The exponents of the standard three-dimensional Ising and three-dimensional Heisenberg models are shown by the horizontal lines. The top panel is a comparison to the scaling law $\gamma+2\beta-3\nu=0$.

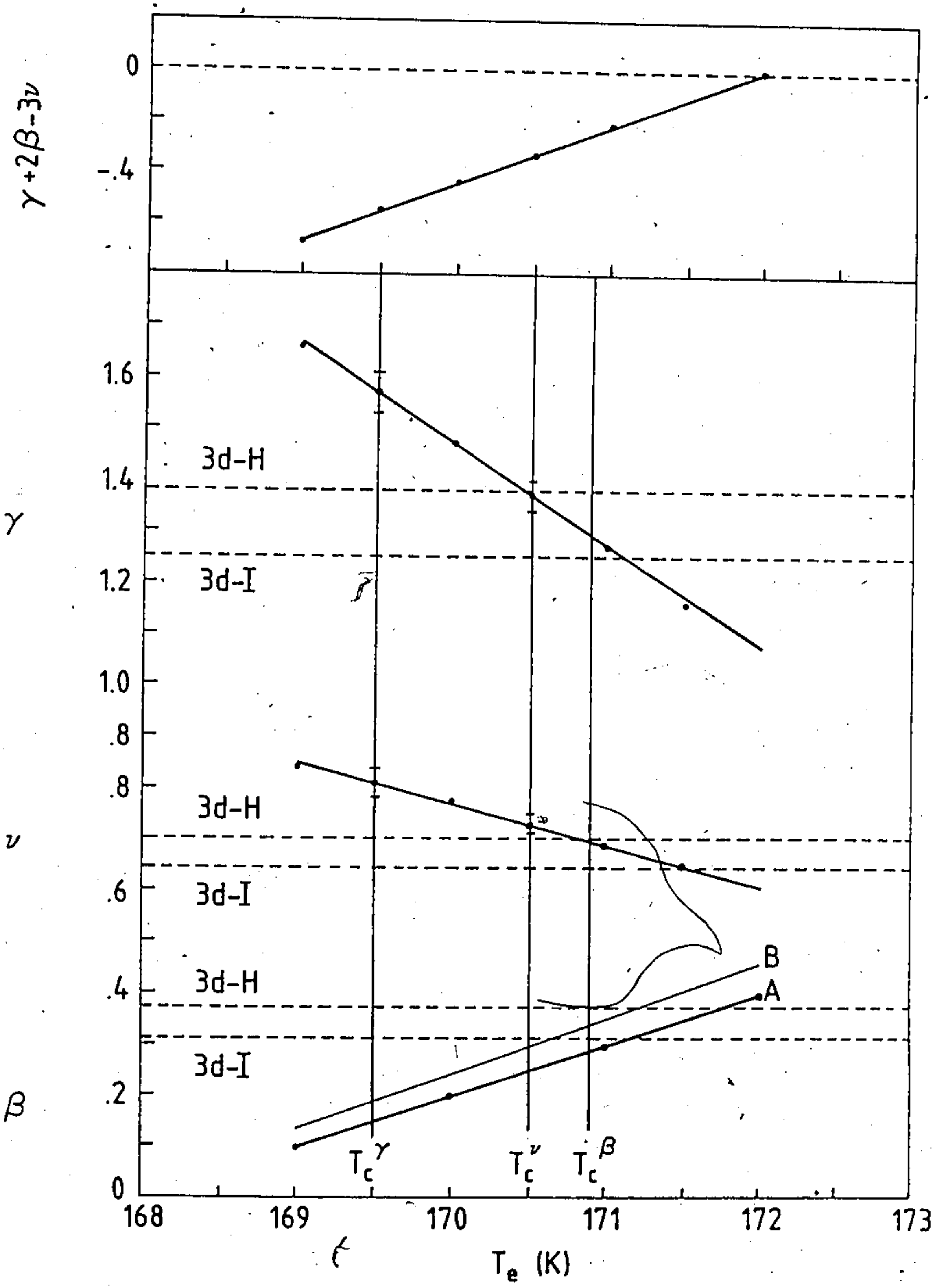

$\gamma+2\beta-3\nu$
0
-.4
γ
1.6
1.4
1.2
1.0
3d-H
3d-I
ν
.8
.8
.6
β
.4
.2
0
B
A
T_c^{γ}
T_c^{ν}
T_c^{β}
168
169
170
171
172
173
T_e (K)

where d is the real space dimensionality of the system, assumed to be $d = 3$. The measured exponents would satisfy this condition only at the upper limit of the temperature range. The scaling laws which include the system dimensionality are known to fail in certain systems for example, VCl_2 (Kadowaki et al, 1987); in this case, as well, $\gamma + 2\beta - 3\nu < 0$.

7.11 The Quasi-Elastic Approximation

In order to estimate the inelasticity of the scattering, a number of coarse triple axis measurements of $S(q,\omega)$ in the paramagnetic phase ($T \approx 182$ K) were performed. A series of constant-Q measurements away from the zone centre (111) along the $(11\bar{1})$ direction are shown in Fig. 7.11. The solid lines are fits to a Lorentzian function convoluted with the triple-axis spectrometer resolution function. The horizontal bars are the calculated intrinsic widths of $S(q,\omega)$.

Parameterizing the q dependence of the dynamic width by a function of the form, Λq^2, it is a simple matter to numerically compare the energy integral at constant q to the energy integral at constant ϕ. The correction factor at any q is never greater than 3%. Because the correction is so small, no attempt was made to include it in the analysis.

7.12 Order Parameter

As pointed out in Sec. 7.7, the behaviour of the order parameter near the phase transition is unusual. It must be emphasized that in Fig. 7.3 only the resolution-limited component of the scattering is plotted. That there is a definite increase in that component around 177 K can be seen quite clearly from Fig. 7.12 which shows two (111)P

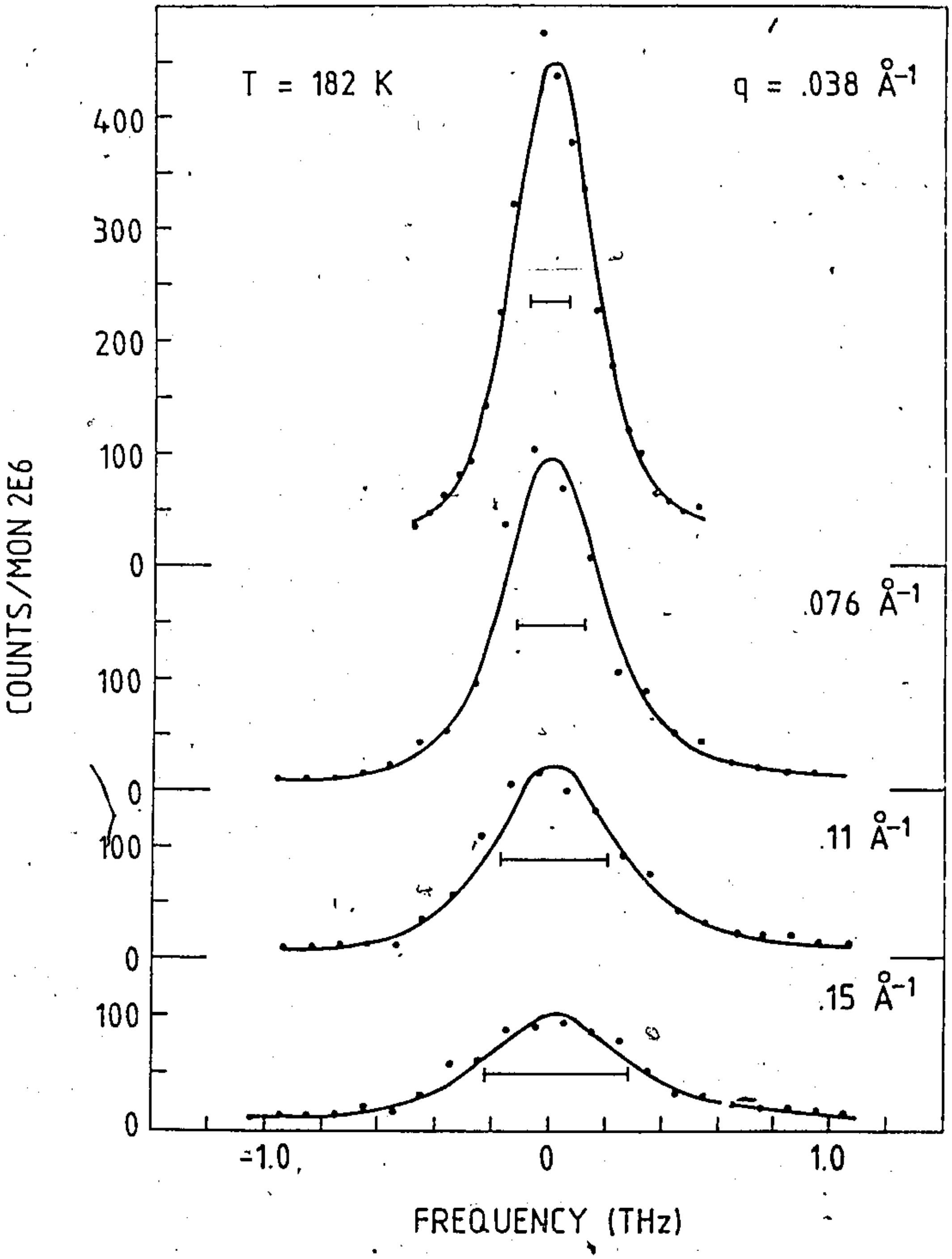

Fig. 7.11 Wave-vector dependence of the inelastic scattering in the paramagnetic phase (T = 182 K). The measurements were made in the (11$\bar{1}$) direction away from the (111) zone centre. The solid lines are fits to the scattering function convoluted with the spectrometer resolution function. The horizontal bars are the determined inelastic widths.

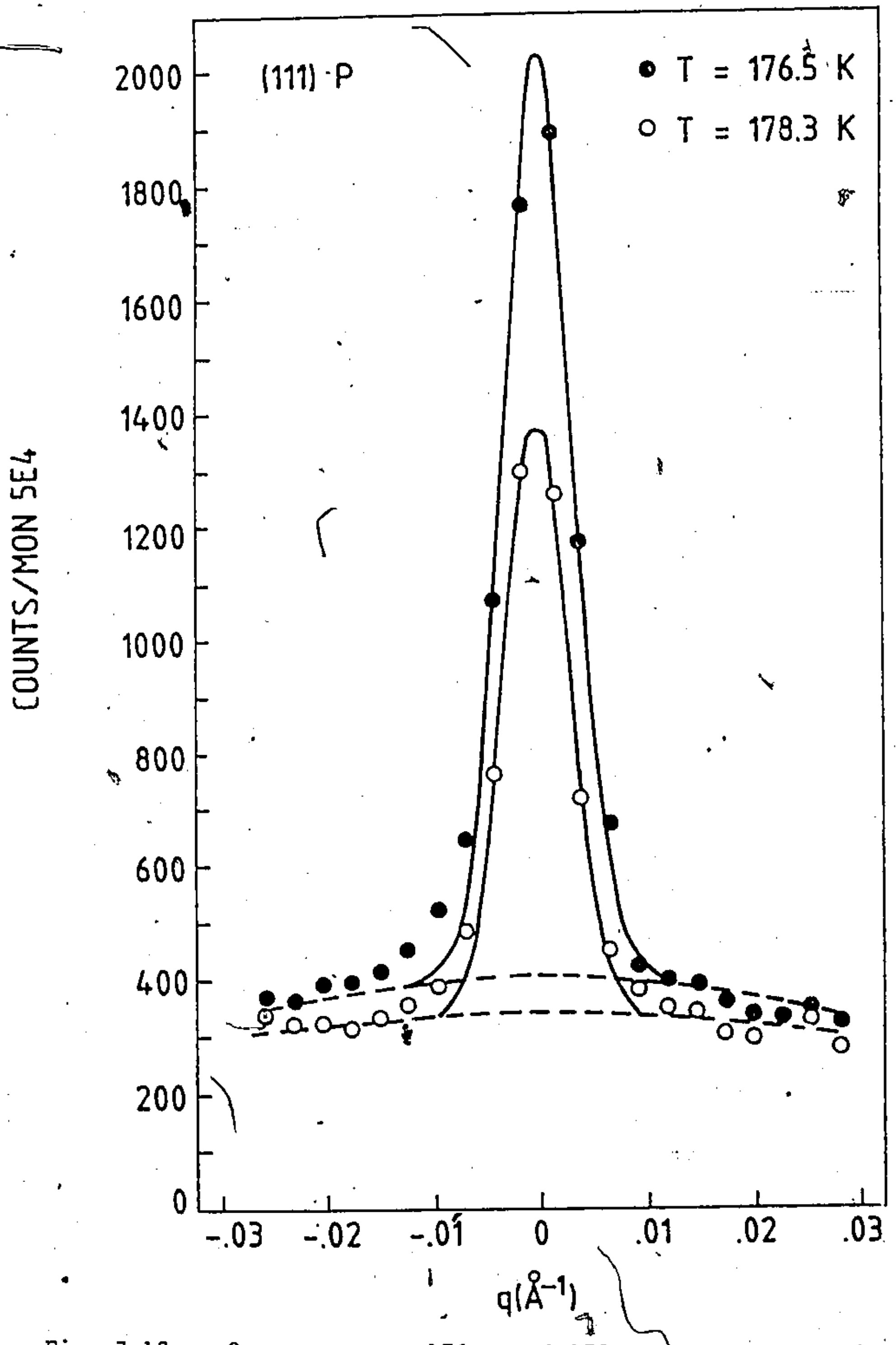

Fig. 7.12 q=0 response at 176 K and 178 K. The dashed lines are from the Lorentzian fits to the critical scattering. There is an increase in the resolution-limited component of the scattering at the lower temperature.

scans at temperatures of 178 K and 176 K. These are fine scans over a very narrow range of q centred on q = 0. At these temperatures it is relatively easy to separate the Bragg component (solid line) from the Lorentzian critical scattering 'background' (dashed line). The difference in intensity at q = 0 can only be described by an additional Bragg (or at least resolution-limited) component to the scattering.

The magnetic phase transition in the chalcogenides is accompanied by a structural distortion suggesting that there are large quadrupolar and magnetoelastic effects at work. There are systems in which magnetic phase transitions are affected by coupling to strains. An extreme example is the phase transition in Cr where completely different transitions are found in strained and unstrained samples. (See, for example, the review by Fawcett, 1988). More recently, Wolf and Huan (1988) have considered the effect of strains on the AF phase transition in DyAlG, and have shown that significant order can be generated in the 'paramagnetic' phase by coupling to internal strains. A static strain in the sample, might act like an external field, pinning the moments and resulting in long range magnetic order before the onset of the critical phase transition. In a naive model, as the critical temperature is approached from below, the order parameter falls in a manner consistent with some exponent β. Near T_c however, the magnetization deviates form the order parameter curve, held up by the coupling to the strain fields.

Similar behaviour has also recently been observed in CeAs (Halg, 1987). CeAs is a cubic (fcc rocksalt) compound with a low temperature type-1 antiferromagnetic ordered phase. Neutron scattering measurements in the critical regime reveal the onset of long range order at a temperature of 8.5 K. However, the short range critical fluctuations persist below this temperature and show a maximum at ≈ 7.8 K. This is thought to arise from a competition between the crystal field effects which favour an antiferromagnetic triple-q structure with a <111> easy axis, and the quadrupolar interaction, which favours a single-q structure with a <001> easy axis. The single-q structure is marginally favoured, but the resulting anisotropy gap is extremely small. In the critical regime this leads to non-linear short-range critical fluctuations away from the <001> ordering direction which suppress the development of the order parameter.

A possibility which is extremely difficult to eliminate is that rather than having a single well-defined transition, there is a distribution of critical temperatures within the bulk of the sample due to stoichiometric changes. If there is a 'distribution of samples' with varying T_c, the contribution to the order parameter at some temperature, T, is a sum over the contribution of each sample whose critical temperature is greater than T. This can be written as

$$M(T) \propto \int_T^\infty dT_c \left(\frac{T_c - T}{T_c}\right)^\beta f(T_c) \qquad [7.10]$$

where $f(T_c)$ is the sample distribution function.

In order to calculate the temperature variation of the order parameter, it is necessary to assume some form for the distribution function. We take for our simple model, a Gaussian distribution of half width σ centred on a temperature T_c^o which represents the critical temperature of the largest fraction of the sample. The measured Bragg peak intensity can then be fitted to Eq. [7.10] by varying T_c^o, σ and β.

An example of a fit for a fixed β is shown in Fig. 7.13. The parameters T_c^o and σ are inset. The exponent β which best reproduces the order parameter for a given T_c^o is plotted in Fig. 7.10 (the 'B' line). β is certainly less than one over the entire range, and more consistent with typical three-dimensional models. However this analysis should not be taken as a quantitative determination of β. The form of the distribution function is unknown and β and T_c^o somewhat sensitive to it. Even for the Gaussian function used here, β and T_c^o are not very well defined: a reasonable fit to the measured points can be produced over the range of T_c. Furthermore, it would be difficult to interpret T_c^o as the critical temperature observed in the critical scattering since the width of the distribution function at T_c^o of 170.5 K is ≈ 5 K.

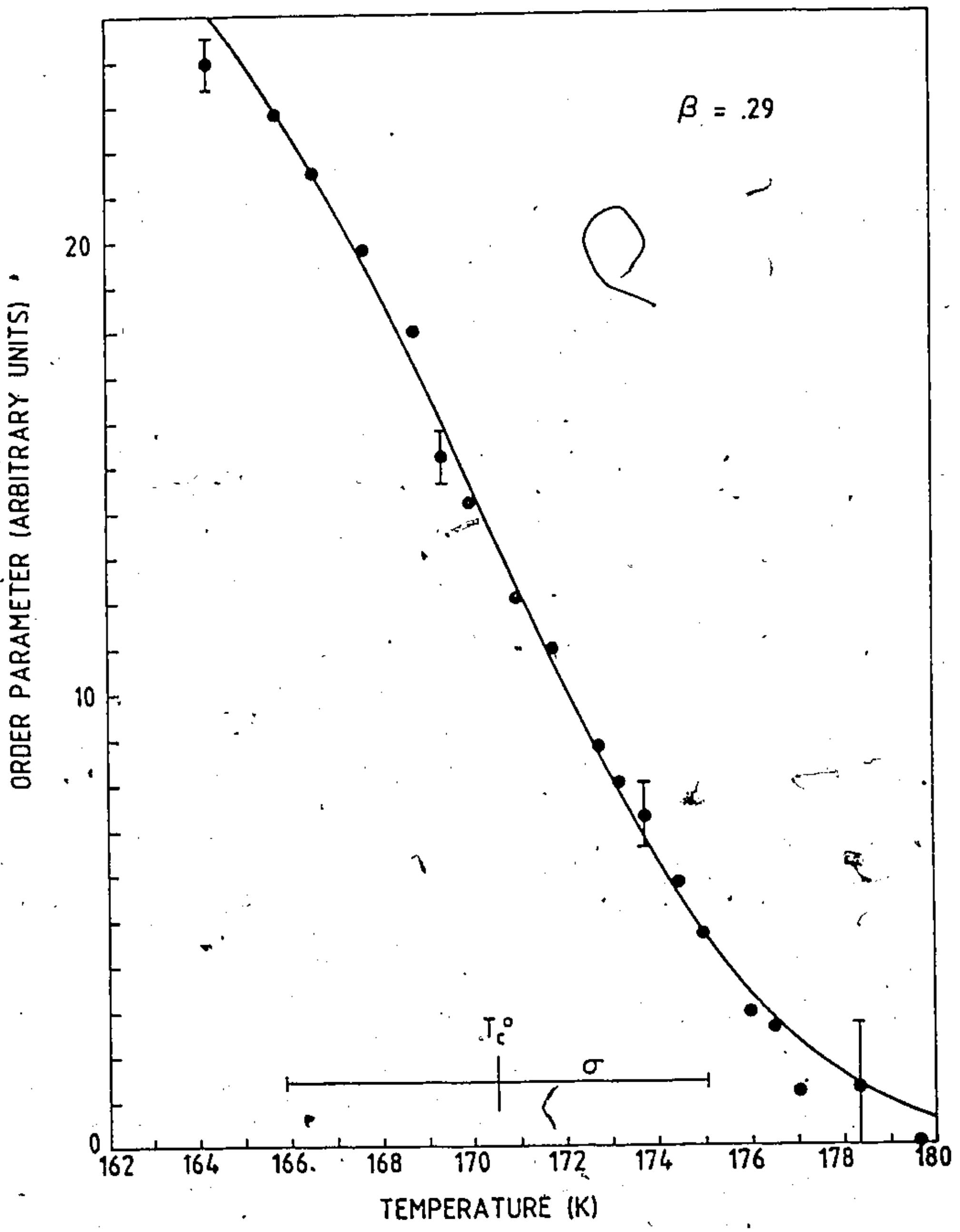

Fig. 7.13 Fit to the order parameter from a model which assumes a distribution of critical temperatures. The distribution function is a Gaussian centred at T_c^o with a half-width σ.

CHAPTER 8: SUMMARY

8.1 Excitations in the Ferromagnetic Phase

Inelastic neutron scattering measurements in the low temperature ferromagnetic phase of USe reveal an unusual magnetic excitation spectrum. Spin-wave-like features are observed at small q, arising from a large zone centre anisotropy gap of 9.4 THz. Even at temperatures well below the ferromagnetic critical temperature, the response is intrinsically broad: at the zone centre, the intrinsic width is estimated to be about 4 THz.

Measurements of the wave-vector dependence of the scattering in the (111) direction show that at small q, the excitations disperse quadratically with a stiffness constant D of 7. THz-$Å^2$. However as q increases beyond a reduced wave vector of about (0.3,0.3,0.3), the relatively well-defined excitation peak observed at small q, broadens into an apparent continuum of scattering. A significant fraction of the spectral weight appears to move to energies >16 THz.

The polarization of the magnetic scattering was measured using a single domain sample. A single domain was created by field-cooling the sample through its ferromagnetic transition temperature. By observing the excitation at equivalent zone centres parallel and (roughly) perpendicular to the magnetization direction, it was determined that there are both longitudinal and transverse components to the scattering. Within the uncertainty of the measurement, the scattering is unpolarized: the measured ratio of χ''_{zz} to χ''_{xx} is very nearly 1:1.

8.2 Local Moment Model

The local moment model of Jackman (1983), which considered the effect of crystal field and exchange interactions on the ground state of the uranium ion, has been extended to include both quadrupolar and magnetoelastic effects. This model is attractive in a number of respects. It provides a simple explanation of the observed reduced moments in that only the moment of the lowest crystal field multiplet is accessible. It incorporates the interaction between the moments and the lattice, manifested in the softening of the c_{44} elastic constant and the rhombohedral distortion at the onset of ferromagnetic order. At the same time, the large quadrupolar interaction provides a mechanism for producing the large anisotropy gap observed in the low temperature magnetic excitation spectrum.

A good description of the UX compounds is obtained, assuming a localized f^3 electronic configuration ($^4I_{9/2}$ Hund's rule ground state) for the uranium ion in the presence of a cubic crystal field, a mean exchange field and a mean quadrupolar field. For the $\Gamma_8^{(2)}$ quartet lowest and well separated in energy from the excited states, this model is capable of reproducing the following magnetic and bulk elastic observables: the Curie-Weiss susceptibility in the paramagnetic phase, the ordered moment, the spin wave anisotropy gap, the behaviour of the c_{44} elastic constant, and the distortion in the ordered phase. The single inconsistency in the model is in the magnitude of the quadrupolar interaction in UTe: the interaction energy measured in the bulk elastic response predicts a gap in the excitation spectrum which is approximately a factor of two larger than measured.

The most obvious inadequacy of a local moment model is in the description of the excitations in the ferromagnetic phase. Such a model can only produce magnetic excitations in the classical sense; well-defined spin waves corresponding to transitions between single-ion levels as modified by inter-ion exchange. In order to describe the intrinsic widths observed in US and USe, it is necessary to introduce some damping mechanism. A simple model of electronic damping resulting from the coupling of the local f-moment to the broader conduction electron response, provides a reasonable description of the observations. It suggests that the progression from well-defined spin waves in UTe to the broad continuum response of US is associated with the broadening and overlap of the electron bands with decreasing U-U separation. It requires, however, an effective bandwidth for the interacting conduction electrons on the scale of the magnetic excitation energies.

The model also fails to predict correctly the polarization of the excitation: in USe, at least, the scattering is found to be unpolarized whereas the model predicts only transverse excitations.

8.3 Critical Scattering

The ferromagnetic phase transition in USe has been studied using neutron scattering techniques. Of the chalcogenides, USe is the most favourable system for a measurement of this type: U and Se have almost the same scattering lengths so that at the (h+k+l) odd Bragg peak positions, the nuclear scattering is extremely weak.

The magnetic critical scattering in the paramagnetic phase has been measured over a decade of reduced temperature. The inverse correlation length and static susceptibility at each temperature have been extracted by fitting $S(\vec{q})$ (convoluted with the spectrometer resolution function) to the standard Lorentzian form. It has proved difficult to extract critical exponents, because of the large uncertainty in the critical temperature. The best estimate of T_c is 170.2 ± 0.9: the critical temperatures deduced independently from the correlation length, static susceptibility, and order parameter data are within a standard deviation. The critical exponents are estimated as $\nu = 0.75 \pm 0.07$, $\gamma = 1.43 \pm 0.2$, and $\beta = 0.22 \pm 0.08$. Of the standard models the 3-dimensional Heisenberg model provides the best description: the exponents ν and γ are within a standard deviation of the Heisenberg predictions and are approximately consistent with a critical temperature of 170.6 K. The exponent β, however, is significantly lower than the Heisenberg prediction. A previous measurement by du Plessis (1982) also showed an anomolously low value of β in USe.

An unusual feature of the phase transition is the apparent onset of long range magnetic order approximately 5 degrees above the critical temperature deduced from the critical scattering. The initial temperature variation of the magnetization is such that, if it were to be described in terms of a power law, the exponent would be greater than one. A possible interpretation of this behaviour is that it is strain-induced ordering, brought about by the moment-quadrupole coupling.

BIBLIOGRAPHY

Aldred A.T., DuPlessis P de V, Lander G.H.
J. Magn. Magn. Mat. 20 (1980) 236

Bacon G., "Neutron Diffraction", third ed., Oxford University Press (1975)

Baer Y., Physica 102B (1980) 104

Bjerrum Moller H., Nielsen M., "Instrumentation for Neutron Inelastic Scattering Research". IAEA, Vienna (1970)

Bjerrum Moller H., Lander G.H., Vogt O., J. de Phys. 40 (1979) C4-28

Bleaney B., Stevens K.W.H., Rept. Prog. Phys. 16 (1953) 108

Brooks M.S.S., Glotzel D., Physica 102B (1980) 51

Busch G., Vogt O., J. Less-Common Met. 62 (1978) 335

Buyers W.J.L., Holden T.M., Perreault A., Phys. Rev. B 11 (1975) 266

Buyers W.J.L., Murray A.F., Holden T.M., Svensson E.C., du Plessis P. de V., Lander G.H., Vogt O., Physica 102B (1980) 291

Buyers W.J.L., Holden T.M., "Handbook of the Physics and Chemistry of the Actinides". Eds A.J. Freeman and G.H. Lander, Elsevier Science Publishers (1985)

Chechernikov V.I., Pechennikov A.V., Yarembash E.I., Martynova L.F., Slavyanskikh V.K., JETP 26 (1968) 328

Cooke J.F., Davis H.L., AIP Conf. Proc. 10 (1973) 1218

Cooper B.R., Siemann D., Yang P., Thayamballi P., Banarjea A., "Handbook of the Physics and Chemistry of the Actinides". Eds A.J. Freeman and G.H. Lander, Elsevier Science Publishers (1985)

Cooper M.J., Nathans R., Acta Cryst 23 (1967) 357

Coqblin B., J. de Phys. 32 (1971) C1-599

Cowley R.A., Dolling G. Phys. Rev. 167 (1968) 464

Cox D.E., Shirane G., Shapiro S.M., Aeppli G., Fisk Z, Smith J.L, Kjems J., Ott H.R., Phys. Rev. B 33 (1986) 3614

Curry N.A., Proc. Phys. Soc. 86 (1965) 1193

Domb C., Hunter D.L., Proc. Phys. Soc. 86 (1965) 1147

du Plessis P. de V., Tillwick D.L., J. Appl. Phys. 50(3) (1979) 1834

du Plessis P. de V., van Doorn C.F., Grobler N.J.S., van Delden D.C., J. Phys. C 15 (1982) 1525

du Plessis P. de V., J. Magn. Magn. Mat., 54-57 (1986) 537

Erbudak M., Keller J., Z. Physik B, 32 (1979) 281

Erbudak M., Greuter F., Meier F., Reihl B., Vogt O., Keller J., J. Appl. Phys. 50(3) (1979) 2099

Fawcett E., Rev. Mod. Phys. 60 (1988) 209

Fedro A.J., Sinha S., "Valence Fluctuations in Solids", eds. L.M. Falicov, W. Hanke, M.B. Maple, North Holland Publishing Co. (1981)

Fisher M.E., "Critical Phenomena, Lecture Notes in Physics ", Springer-Verlag, Berlin (1982)

Frazer C., Shirane G., Cox D.E., Olsen C.E., Phys. Rev. 140 A (1965) 1449

Gilat G., Nicklow R.M., Phys. Rev. 143 (1966) 487

Greuter F., Hauser E., Oelhafen P., Guntherodt H.J., Riehl B., Vogt O., Physica 102B (1980) 117

Halg B., Furrer A., Kjems J.K., Phys. Rev. Lett. 59 (1987) 1034

Hill H.H., "Plutonium 1970 and Other Actinides". Ed. W.N. Miner, The Metallurgical Society of the AIME, New York (1970)

Holden T.M., Buyers W.J.L., Svensson E.C., Lander G.H. Phys. Rev. B 30 (1984) 114

Hu G., Cooper B.R., J. Appl. Phys., 63(8) (1988) 3826

Hutchings M.T., "Solid State Physics". Eds F. Seitz and D. Turnbull, Academic Press, New York (1964)

Izuyama T., Kim D.J., Kubo R., J. Phys. Soc. Japan 18 (1963) 1025

Jackman J.A., Ph.D. Thesis (University of Guelph) 1983

Jackman J.A., Holden T.M., W.J.L. Buyers, DuPlessis P de V, Vogt O., Genossar J., Phys. Rev. B 33 (1986) 7144

Kadanoff L.P., Physics 2 (1966) 263

Kadowaki H., Ubokoshi K., Hirakawa K., Martinez J., Shirane G., J. Phys. Soc. Japan 56 (1987) 4027

Kittel C., "Phonons in Perfect Lattices and Lattices with Point Imperfections". Ed R.W.H. Stevenson, Oliver and Boyd, Edinburgh (1966)

Lander G.H., Faber J., Freeman A.J., Desclaux J.P., Phys. Rev. B 13 (1976) 1177

Lea K.R., Leask M.J.M., Wolf W.P., J. Phys. Chem. Solid, 23 (1962) 1381

Maekawa S., Takahashi S., Kashiba S., Tachiki M., J. Phys. Soc. Japan 54 (1985) 1955

Marples J.A.C., J. Phys. Chem. Solids, 31 (1970) 2431

Marshall W., Lovesey S.W., "Theory of Thermal Neutron Scattering", Oxford University Press, London (1971)

Mook H.A., Nicklow R.M., Thompson E.D., Wilkinson M.K., J. Appl. Phys. 40 (1969) 1450

Morin P., Rouchy J., du Tremolet de Lacheisserie E., Phys. Rev. B 16 (1977) 3182

Morin P., Schmitt D., Vettier C., Rossat-Mignod J., J. Phys F 10 (1980) 1575

Norton P.R., Tapping R.L., Creber D.K., Buyers W.J.L., Phys. Rev. B 21(6) (1980) 2572

Nuenschwander J., Vogt O., Voit E., Wachter P., Physica, 144 B&C (1986) 66

Nye J.F., "Physical Properties of Crystals", Oxford University Press, New York (1985)

Ott H.R., Rudigier H., Fisk Z., Smith J.L., Phys. Rev. Lett. 50 (1983) 1595

Ott H.R., Rudigier H., Delsing P., Fisk Z., Phys. Rev. Lett. 52 (1984) 1551

"Phase Transitions and Critical Phenomena" Vol. 3 Eds C.Domb, M.S. Green, Academic Press, London (1974)

"Phase Transitions and Critical Phenomena" Vol. 6 Eds C. Domb, M.S. Green, Academic Press, London (1976)

Pop I., Coldea M., Niculescu V., Czech. J. Phys. B 24 (1974) 1398

Riehl B., Martensson N., Vogt O., J. Appl. Phys. 53(3) (1982) 2008

Rudigier H., Ott H.R., Vogt O., Phys. Rev. B 32 (1985) 4584

Schneider W., Laubschat C., Phys. Rev. B 23 (1981) 997

Shoenes J., Phys. Rep. 66 (1980) 187

Sivardiere J., J. Magn. Magn. Mat. 1 (1975) 23

Stevens K.W.H., Proc. Phys. Soc. (London) A65 (1952) 209

Stewart G.R., Fisk Z., [illegible]re M.S., Phys. Rev. B 30 (1984a) 482

Stewart G.R., Fisk Z., Willis O., Smith J.L., Phys. Rev. Lett. 52 (1984b) 679

Takahashi Y., Westrum Jr. E.F., J. Phys. Chem. 69 (1965) 3618

Tillwick D.L., du Plessis P. de V., J. Magn. Magn Mat. 3 (1976) 319

Van Hove L., Phys. Rev. 95 (1954) 1374

Vogt O., Physica 102 B (1980) 206

Wedgwood F.A., Kuznietz M., J. Phys. C 5 (1972) 3012

Wedgwood F.A., J. Phys. C 5 (1972) 2427

Westrum Jr. E.F., Walters R.R., Flotlow H.E., Osborne D.W., J. Chem. Phys. 48 (1968) 155

Widom B., J. Phys. Chem. 43 (1965) 3898

Wolf W.P., Huan C.H.A., J. Appl. Phys. 63(8) (1988) 3904

APPENDIX A: HAMILTONIAN OF THE LOCALIZED MODEL

A.1 Elastic Energy

This discussion is only intended to establish the notation used in the text. Complete treatments of the elastic response can be found in Nye (1985) or Kittel (1966).

The effect of applying a strain is to move a point in the crystal from a position $\vec{r}$ to a position $\vec{r}\,'$. $\vec{r}$ is related to $\vec{r}\,'$ through the strain matrix, E, by

$$\vec{r}\,' = E\vec{r} \qquad [A.1]$$

where

$$E = \begin{pmatrix} e_{xx} & \varepsilon_{xy} & \varepsilon_{xz} \\ \varepsilon_{yx} & e_{yy} & \varepsilon_{yz} \\ \varepsilon_{zx} & \varepsilon_{zy} & e_{zz} \end{pmatrix} \qquad [A.2]$$

The components of the strain tensor are most easily interpreted by considering the effect of the strain on the cubic basis vectors $\{\hat{x}, \hat{y}, \hat{z}\}$. In the strained matrix

$$\{\hat{x}, \hat{y}, \hat{z}\} \rightarrow \{\vec{x}\,' \ \vec{y}\,' \ \vec{z}\,'\}$$

where the primed vectors are defined by Eq. [A.1]. The strained vector $\vec{x}\,'$, for example, is given by

$$\vec{x}\,' = (1 + e_{xx})\,\hat{x} + \varepsilon_{xy}\,\hat{y} + \varepsilon_{xz}\,\hat{z} \qquad [A.3]$$

where to first order

$$\vec{x}\,' \cdot \vec{y}\,' = \varepsilon_{xy} + \varepsilon_{yx} \qquad [A.4]$$

For the symmetrized strain, $e_{xy} = \frac{1}{2}(\varepsilon_{xy}+\varepsilon_{yx})$, this simply reduces to

$$e_{xy} = \frac{1}{2}\,\vec{x}\,' \cdot \vec{y}\,' \qquad [A.5]$$

It is convenient to define the strain components

$$\varepsilon_0 = e_{xx} + e_{yy} + e_{zz}$$
$$\varepsilon_1 = 2e_{zz} - e_{xx} - e_{yy} \qquad [A.6]$$
$$\varepsilon_2 = e_{xx} - e_{yy}$$

With these definitions, the elastic strain energy is given by

$$E_{EL} = \frac{1}{2}\left(\frac{c_{11} + 2c_{12}}{3}\right)\varepsilon_o^2 + (c_{11} - c_{12})(\varepsilon_1^2 + \varepsilon_2^2) + 2c_{44}(e_{xy}^2 + e_{yz}^2 + e_{zx}^2) \qquad [A.7]$$

where c_{11}, c_{12}, and c_{44} are the elastic stiffness constants defined in the usual way (see, for example, Kittel 1966).

A.2 Quadrupole Operators

The convention of Morin et al (1977) has been used in defining the quadrupole operators. With respect to a (001) z axis:

$$O_2^0 = 2(S^z)^2 - (S^x)^2 - (S^y)^2$$
$$O_2^2 = (S^x)^2 - (S^y)^2 \qquad [A.8]$$
$$P_{ij} = \frac{1}{2}(S^iS^j + S^jS^i) \qquad \text{where } i,j = x,y,z.$$

A.3 The Reduced Hamiltonian

The most general form of the Hamiltonian is

$$H = H_{CF} + H_{EX} + H_Q + H_{ME} + E_{EL} \qquad [A.9]$$

where the individual contributions are described in Sec. 6.2. In this appendix, the simplifying approximations which lead to the reduced form, Eq. [6.7], are described.

(i) Mean Field Approximation

The Heisenberg Hamiltonian can be rewritten in the form

$$H = -\sum_{ij} J_{ij}(\vec{S}_i - \langle\vec{S}\rangle) \cdot (\vec{S}_j - \langle\vec{S}\rangle) + 2J\sum_i \langle\vec{S}\rangle \cdot \vec{S}_i - \sum_i J\langle\vec{S}_i\rangle^2 \qquad [A.10]$$

where $\langle\vec{S}\rangle$ is the average value of the spin and

$$J = \sum_{ij} J_{ij} \qquad [A.11]$$

where only nearest neighbour interactions are assumed. The first term, which involves fluctuations away from the average value of $\langle\vec{S}\rangle$ is neglected in the mean field treatment so that the single-ion Hamiltonian becomes

$$H_{EX}^{MF} = 2J\langle\vec{S}\rangle \cdot \vec{S} - J\langle\vec{S}\rangle^2 \qquad [A.12]$$

The mean field quadrupolar interaction Hamiltonian is obtained in the same way.

(ii) Rhombohedral Strain

The Hamiltonian is much simplified if only the strains that have the symmetry of the distortion in the ordered phase are included. The symmetry of a rhombohedral strain is such that

$$\begin{aligned} \varepsilon_1 &= \varepsilon_2 = 0 \\ e_{xy} &= e_{yz} = e_{zx} \end{aligned} \qquad [A.13]$$

When a stress is applied, the system can lower its free energy by distorting. The response of the system is determined by minimizing the free energy with respect to each component of the strain. It can be shown that only certain of the quadrupole operators enter the

Hamiltonian for a strain of the required symmetry. For the Hamiltonian, H, with eigenvectors $|m\rangle$ and eigenvalues E_m, the free energy is given by

$$F = -\, kT\ LN(Z) \qquad [A.14]$$

where Z is the partition function $Z = \sum_m e^{-\beta E_m}$. The only terms in the Hamiltonian which contain strains are H_{ME} and E_{EL}, and for simplicity these are written

$$H_{ME} = \sum_j B_j \varepsilon_j O_j$$
$$E_{EL} = \sum_j c_j \varepsilon_j^2 \qquad [A.15]$$

where ε_j is a strain, B_j and C_j are the corresponding magneto-elastic and elastic coefficients (including relevant numerical constants) and O_j is the associated quadrupole operator.

Taking the derivative of F with respect to a particular strain component, ε,

$$\frac{dF}{d\varepsilon} = 2c\varepsilon - B\langle O\rangle \qquad [A.16]$$

F is minimized when

$$\langle O\rangle = \frac{2c}{B}\varepsilon \qquad [A.17]$$

i.e. the expectation value of the quadrupole operator is proportional to its associated strain. Then, from Eq. [A.13]

$$\langle \bar{O}_2^0\rangle = \langle O_2^2\rangle = 0$$
$$\langle P_{xy}\rangle = \langle P_{yz}\rangle = \langle P_{zx}\rangle \qquad [A.18]$$

Omitting the terms in $\langle O_2^0\rangle$ and $\langle O_2^2\rangle$, replacing $\langle P_{ij}\rangle$ with $\langle P\rangle$ and e_{ij} with e, the terms H_{ME}, H_Q and E_{EL} are reduced to

$$H_{ME} = -\frac{B_5}{2}\, e\,(P_{xy} + P_{yz} + P_{zx})$$

$$H_Q^{MF} = -\frac{K_2}{4}\left[2\langle P\rangle (P_{xy} + P_{yz} + P_{zx}) - 3\langle P\rangle^2\right] \qquad [A.19]$$

$$E_{EL} = 6c_{44}e^2$$

(iii) Rotation to <111> Axis

A further simplification can be made by changing coordinate frames. The distortion is symmetric about the <111> direction, and it is the easy axis for the magnetization. It is then convenient to redefine <111> as the z-axis. Because the exchange Hamiltonian is not tied to the lattice, it is invariant under the rotation. The remaining terms, however, must all be transformed. The necessary transformations are:

$$P_{xy} + P_{yz} + P_{zx} \rightarrow O_2^{0\prime}$$

$$\langle P\rangle \rightarrow \frac{1}{3}\langle O_2^{0\prime}\rangle \qquad [A.20]$$

$$e \rightarrow \frac{1}{\sqrt{3}}\,\varepsilon_1'$$

where primes denote operators (and strain components) in the <111> frame.

Finally, the cubic crystal field Hamiltonian for a 3-fold z-axis is given by Hutchings (1964) as

$$H_{CF} = -\frac{2}{3}B_4(O_4^0 - 20\sqrt{2}\,O_4^3) + \frac{16}{9}(O_6^0 + \frac{35}{4}O_6^3 + \frac{77}{8}O_6^6) \qquad [A.21]$$

The complete Hamiltonian has the form

$$H^{MF} = H_{CF} - 2J\langle S^z\rangle S^z + J\langle S^z\rangle^2$$

$$- \left(\frac{\sqrt{3}}{6}B_5\varepsilon_1' + \frac{1}{6}K_2\langle O_2^{0\prime}\rangle\right)O_2^{0\prime} + \frac{1}{12}K_2\langle O_2^{0\prime}\rangle^2 + 2c_{44}(\varepsilon_1')^2 \qquad [A.22]$$

In the text, the primed notation is dropped and all operators are understood to be with respect to the <111> direction. For convenience, the parameters B_5, K_2 and ε_1 will be referred to as B, K and ε.

A.4 Distortion in the Ordered Phase

The cubic structure is naturally defined in terms of the basis vectors $\{\hat{x},\hat{y},\hat{z}\}$ parallel to the cube edges. The rhombohedral structure in the ordered phase is more conveniently described by a set of orthogonal vectors $\{\hat{x}',\hat{y}',\hat{z}'\}$ which have z along the threefold symmetric (111) axis. With respect to the cubic basis, these are

$$\hat{x}' = \frac{1}{\sqrt{6}}(\bar{1},\ \bar{1},\ 2)$$

$$\hat{y}' = \frac{1}{\sqrt{2}}(1,\ \bar{1},\ 0) \qquad [A.23]$$

$$\hat{z}' = \frac{1}{\sqrt{3}}(1,\ 1,\ 1)$$

The primitive vectors of a general rhombohedron (with respect to $\{\hat{x}',\hat{y}',\hat{z}'\}$ are then given by

$$\vec{a}_1 = a_o(-p,\ 0,\ q)$$

$$\vec{a}_2 = a_o(\frac{p}{2},\ \frac{\sqrt{3}}{2}p,\ q) \qquad [A.24]$$

$$\vec{a}_3 = a_o(\frac{p}{2},\ \frac{-\sqrt{3}}{2}p,\ q)$$

with the constraint that $p^2 + q^2 = 1$. In a cubic structure $q^2 = 2/3$ and the primitive vectors correspond to the face centres.

The magnitude of the rhombohedral distortion in the ordered phase is commonly expressed in terms of the angles Δ_{90} or Δ_{60}. In a cubic crystal, the angle between the basis vectors is 90° and the angle between adjacent face centres, 60°. The angles Δ_{90} and Δ_{60} are the corrections to the cubic angles which result from the distortion.

The angle Δ_{60} is defined by

$$\cos(60 + \Delta_{60}) = \hat{a}_i \cdot \hat{a}_j \qquad [A.25]$$

In the limit of Δ_{60} small, this reduces to

$$\Delta_{60} = \frac{1}{\sqrt{3}}\,(2 - 3q^2) \qquad [A.26]$$

The angle Δ_{90} is defined by

$$\cos(90 + \Delta_{90}) = \hat{A}_i \cdot \hat{A}_j \qquad [A.27]$$

where the vectors $\hat{A}_i$ would correspond to $\{\hat{x},\hat{y},\hat{z}\}$ in the cubic frame (eg. $\vec{A} = \vec{a}_1 + \vec{a}_2 - \vec{a}_3$). In the limit of Δ_{90} small, this reduces to

$$\Delta_{90} = \frac{\sqrt{3}}{4-3q^2}\,\Delta_{60} \simeq \frac{\sqrt{3}}{2}\,\Delta_{60} \qquad [A.28]$$

(taking $q^2 \simeq 2/3$).

The transverse strain component, e_{ij} ($i \neq j$), is defined as (Eq. [A.5])

$$e_{ij} \simeq \frac{1}{2}\,\hat{A}_i \cdot \hat{A}_j \qquad [A.29]$$

From Eqs. [A.27] and [A.28]

$$e_{ij} \simeq -\frac{\sqrt{3}}{4}\,\Delta_{60} \qquad [A.30]$$

The strain in the ordered phase, ε (ε_1' in Eq. [A.20]), is then

$$\varepsilon \simeq -\frac{3}{4}\,\Delta_{60} \qquad [A.31]$$

From Eq. [A.17], ε is related to the quadrupole moment $\langle O_2^0 \rangle$ by

$$\varepsilon = \frac{\sqrt{3}}{24} \frac{B}{c_{44}} \langle O_2^0 \rangle \qquad [A.32]$$

Replacing ε by Δ_{60} and B by K_{ME} (as defined in Sec. 6.5)

$$\Delta_{60} = \frac{2}{3} \surd \frac{K_{ME}}{c_{44}} \langle O_2^0 \rangle \qquad [A.33]$$

APPENDIX B: MAGNETIC EXCITATIONS IN THE LOCALIZED MODEL

B.1 Spin Waves in the Ordered Phase

A general formalism for calculating the spin wave excitation spectrum of a system with both crystal field and exchange interactions was developed by Buyers, Holden and Perrault (1975). The Hamiltonian

$$H = H_{CF} + \sum_{ij} J_{ij} \vec{S}_i \cdot \vec{S}_j \qquad [B.1]$$

can be divided into two parts: a single-ion part

$$H_{SI} = H_{CF} + 2 \sum_{i} \left(\sum_{i} J_{ij} \right) \langle S^z \rangle S_i^z \qquad [B.2]$$

and an inter-ion part

$$H_I = \frac{1}{2} \sum_{ij} J_{ij} (S_i^+ S_j^- + S_i^- S_j^+) + \sum_{ij} J_{ij} S_i^z (S_j^z - 2 \langle S^z \rangle) \qquad [B.3]$$

The single-ion Hamiltonian, diagonalized in the ground state S-multiplet, produces a new set of basis states, $|m\rangle$, consistent with the symmetry of the crystal field, and the presence of a mean exchange field. (In the calculation in Chapter 6 there is also a contribution to H_{SI} from the quadrupolar field). The excitation spectrum consists of fluctuations between these basis states.

The dynamic susceptibility is obtained by finding the equation of motion, governed by the inter-ion Hamiltonian, of the relevant response functions, in this case

$$G_{ij}^{\alpha\beta}(t) = - i\theta(t) \langle [S_i^{\alpha}(t), S_j^{\beta}(0)] \rangle \qquad [B.4]$$

The details of the derivation can be found in Buyers (1975); the Fourier transformed result is simply quoted here

$$\begin{aligned} G^{\alpha\beta}(\vec{q},\omega) = {} & g^{\alpha\beta}(\omega) + g^{\alpha+}(\omega) J_{\vec{q}} G^{-\beta}(\vec{q},\omega) + g^{\alpha-}(\omega) J_{\vec{q}} G^{+\beta}(\vec{q},\omega) \\ & + 2g^{zz}(\omega) J_{\vec{q}} G^{z\beta}(\vec{q},\omega) \end{aligned} \qquad [B.5]$$

where $J_{\vec{q}}$ is the Fourier transform of the exchange constant

$$J_{\vec{q}} = \frac{1}{N} \sum_{i} J_{ij}\, e^{i\vec{q}\cdot(\vec{r}_i - \vec{r}_j)} \qquad [B.6]$$

and $g^{\alpha\beta}(\omega)$ is the single-ion susceptibility

$$g^{\alpha\beta}(\omega) = \sum_{mn} \langle m|S^{\alpha}|n\rangle \langle n|S^{\beta}|m\rangle \frac{f_m - f_n}{\omega - (\omega_n - \omega_m)} \qquad [B.7]$$

where f_m is the Boltzmann population factor of the state $|m\rangle$ with energy ω_m. In cubic symmetry, only certain of the matrix elements are non-zero, specifically g^{+-}, g^{-+}, and g^{zz}. The transverse and longitudinal parts of the response are then decoupled in Eq. [B.5] yielding

$$G^{+-}(\vec{q},\omega) = \frac{g^{+-}(\omega)}{1 - J_{\vec{q}}\, g^{+-}(\omega)} \qquad G^{-+}(\vec{q},\omega) = \frac{g^{-+}(\omega)}{1 - J_{\vec{q}}\, g^{-+}(\omega)} \qquad [B.8]$$

and

$$G^{zz}(\vec{q},\omega) = \frac{g^{zz}(\omega)}{1 - 2J_{\vec{q}}\, g^{zz}(\omega)} \qquad [B.9]$$

The dynamic response is obtained in the usual way, by letting $\omega \rightarrow \omega + i\eta$ (where η is an infinitesimal quantity), and solving for the imaginary part of the response function. In the absence of inter-ion exchange (i.e. $J = 0$) the response function reduces to $g(\omega)$, and the solutions are a series of δ-functions at energies corresponding to transitions between single-ion levels. The effect of the exchange coupling is to renormalize the excitation energies: the solutions correspond to the poles of $G(\vec{q},\omega)$ rather than $g(\omega)$. The spin wave energies are given by

$$1 - J_{\vec{q}}\, g^{+-}(\omega) = 0$$

$$1 - J_{\vec{q}}\, g^{-+}(\omega) = 0 \qquad [B.10]$$

$$1 - 2J_{\vec{q}}\, g^{zz}(\omega) = 0 \quad .$$

In an fcc lattice, assuming nearest neighbour interactions only, the wave-vector dependent exchange constant for $\vec{q} = (\zeta,\zeta,\zeta)$ is

$$J_{\vec{q}} = 6J(1 + \cos 2\pi\zeta) \quad . \qquad [B.11]$$

At the zone boundary ($\zeta = 0.5$) $J_{\vec{q}} = 0$. The spin wave excitation energies are the transition energies among the single-ion levels.

B.2 Static Susceptibility

The static susceptibility is obtained from the longitudinal response function $G^{zz}(\vec{q},\omega)$ (Eq. [B.9]) in the limit of $q \rightarrow 0$ and $\omega \rightarrow 0$, i.e.

$$G^{zz} = \frac{g^{zz}}{1 - 2J_0 g^{zz}} \qquad [B.12]$$

where, in this case,

$$g^{zz} = \sum_{mn} \left|\langle m|S^z|n\rangle\right|^2 \frac{f_m - f_n}{\omega_m - \omega_n} \qquad [B.13]$$

In the text, g^{zz} is referred to as the single-ion susceptibility, χ_0.

APPENDIX C: SCALING AND UNIVERSALITY

C.1 Generalized Homogeneous Functions and the Scaling Hypothesis

The static scaling hypothesis, first formulated by Widom (1965) and Domb and Hunter (1965), is that the thermodynamic potentials can be described by generalized homogeneous functions near the critical temperature. The term generalized homogeneous function is applied to any function, f(x), which satisfies the condition

$$f(\lambda^{1/a}x) = \lambda f(x) \qquad [C.1]$$

for any values of the constants λ and a. A thorough review of the properties of homogeneous functions is given by Stanley (1971). For the purpose of this discussion, it will suffice to point out the following feature: since the condition, Eq. [C.1], is true for all λ and a, then it must be true, in particular, for

$$\lambda^{1/a} = \frac{1}{x} \qquad [C.2]$$

In this case, Eq. [C.1] can be rewritten as

$$f(x) = x^{-a}f(1) \qquad [C.3]$$

i.e. f(x) varies as a power law in x.

The extension of the definition to a generalized homogeneous function of more than one variable is straightforward:

$$f(\lambda^{a}x,\lambda^{b}y) = \lambda f(x,y) \qquad [C.4]$$

for all values of λ, a, and b

The usefulness of this hypothesis is that it immediately leads to predictions about the behaviour of the observables, such as the magnetization, the susceptibility and the specific heat, near the critical temperature. To see this, we write the free energy, G, as a function of the relevant external variables; the temperature (which will be defined here in terms of the reduced temperature, t) and the applied magnetic field, H. From Eq. [C.4], G(t,H) satisfies

$$G(\lambda^a t, \lambda^b H) = \lambda G(t,H) \qquad [C.5]$$

Now, for example, the magnetization, M, is defined by

$$M = \lim_{H\to 0} \frac{dG}{dH} \qquad [C.6]$$

Taking the derivative and applying the limit to Eq. [C.6], means that

$$M(\lambda^a t,0) = \lambda^{1-b} M(t,0) \qquad [C.7]$$

i.e. M is a homogeneous function. Applying the argument used to obtain Eq. [C.3], M(t,0) can be expressed as

$$M(t,0) = (-t)^{\frac{1-b}{a}} \; M(-1,0) \qquad [C.8]$$

The magnetization can be described by a power law, with an exponent, β, given by

$$\beta = \frac{1-b}{a} \qquad [C.9]$$

In fact similar arguments can be applied to any thermodynamic variable derived from G(t,H). It is important to realize that all of the exponents that come out of this formalism are defined in terms of only two parameters, a and b. The significance of this is that the critical exponents can not all be independent: any two exponents are sufficient to define all the rest. This fact leads to relationships among the exponents known as the scaling laws. An example is the well known equation relating the exponents of the specific heat (α), magnetization (β) and susceptibility (γ).

$$\alpha + 2\beta + \gamma = 2 \qquad [C.10]$$

Although it has no rigorous justification, in practice the scaling hypothesis seems to hold. The formulation of scaling due to Kadanoff (1966), though again not a rigorous proof, provides a physical sense of what is embodied in the mathematical form of the scaling hypothesis.

C.2 Scaling

It will be recalled that in the critical regime, there are large fluctuating regions and that the extent of these regions is characterized by the correlation length, ζ. The correlation length may be expressed in dimensionless units by referencing it to some fundamental length scale, r, in the physical system. r might be, for example, some interatomic spacing, a. The dimensionless correlation length is then ζ/r, or in this case ζ/a.

Suppose now that the system length scale is redefined by taking $r = 2a$. The correlation length in absolute units is, of course, unaffected. In terms of the dimensionless quantity however, the correlation length has apparently been reduced by a factor of two, or stated another way, the temperature $|t|$ has apparently increased. Thus redefining the length scale is equivalent to changing the temperature.

In order to make a mathematical statement of the argument, associate with the length scale, $r = a$, a reduced temperature, t, and with the length scale, $r = 2a$, a reduced temperature $\tilde{t}$. Then

$$\frac{1}{2}\,\zeta(t) = \zeta(\tilde{t}) \qquad [C.11]$$

More generally, if the length scale is changed by some factor, ℓ,

$$\frac{1}{\ell}\,\zeta(t) = \zeta(\tilde{t}) \qquad [C.12]$$

In order to carry the argument any further, it is necessary to define a relationship between t and $\tilde{t}$. The simplest possible assumption is that t and $\tilde{t}$ are related linearly. It is also reasonable, since the change in temperature results from a change in scale, that the coefficient in the transformation is a function of ℓ, i.e.

$$\tilde{t} = f(\ell)t \qquad [C.13]$$

In particular, if the coefficient has the form

$$f(\ell) = \ell^{y} \qquad [C.14]$$

where y is a constant, then the correlation length is a homogeneous function, according to the definition of Eq. [C.1], i.e.

$$\zeta(t) = \ell\zeta(\tilde{t})$$

$$\zeta(\ell^{-y}\tilde{t}) = \ell\zeta(\tilde{t}) \qquad [C.15]$$

The result is that the function ζ can be described by a power law with critical exponent y (Eq. [C.3]) i.e.

$$\zeta(t) \propto t^{y} \qquad [C.16]$$

The basic premise of the scaling formulation is that the thermodynamic variables such as the free energy, G, can be described in terms of generalized homogeneous functions. The argument proceeds in much the same way as it does for the correlation length. Let the reference length for the physical system be some interatomic distance, $r = a$, and associate with a cell, of volume a^3, the free energy G_c. Now if the reference scale is changed, from a to ℓa, the volume of the cell is increased by a factor of ℓ^3. Because the free energy is extrinsic, the free energy of the renormalized cell, G_r, scales with the volume, i.e.

$$G_r = \ell^3 G_c \qquad [C.17]$$

As before, the change in scale can be associated with a change in temperature. Let t be the temperature describing the orginal system, and $\tilde{t}$, the temperature of the renormalized system. Equation [C.17] becomes

$$G(\tilde{t}) = \ell^3 G(t) \qquad [C.18]$$

and by the arguments used previously, G(t) is a generalized homogeneous function.

In fact, the entire scaling argument is somewhat more subtle in this case because it relies on the assumption that G_r and G_c have the same functional form. The implications of this can be understood by considering a magnetic system on a microscopic level. Ultimately the form of G is determined by the Hamiltonian of the microscopic spin system, for example

$$H \propto J \sum_{ij} \vec{S}_i \cdot \vec{S}_j \qquad [C.19]$$

where $\vec{S}_i$ is the spin on site i and J is the interaction between spins on different sites. Whether the form of G can be retained under a scale transformation will depend on how the Hamiltonian renormalizes. Suppose that when the cell size is renormalized from a^3, which contains a single site with spin S (for example), to a size $(\ell a)^3$, which contains many sites, the Hamiltonian can be rewritten in terms of and effective spin $\tilde{S}$ of the new cell, and and effective exchange $\tilde{J}$ between the new cells. In this way the parameters are renormalized but the form of the Hamiltonian is retained, ie.

$$H \rightarrow \tilde{J} \sum_{ij} \tilde{\vec{S}}_i \cdot \tilde{\vec{S}}_j \qquad [C.20]$$

C.3 Universality

Although the scaling formulation yields relationships among the critical exponents, it does not give any information about the magnitudes of the exponents. These must be obtained from direct calculations on model systems. The actual techniques applied to these problems are beyond the scope of this discussion. (Reviews can be found in Phase Transitions and Critical Phenomena Volumes 3 and 6, and Fisher, 1982). There are, in fact, very few models which can be solved exactly and it is for this reason that the concept of universality is important. Universality is another hypothesis which states that the critical behaviour (in particular the critical exponents) of a system depends only on three things:

(i) the real space dimensionality of the system
(ii) the dimensionality of the order parameter (in the case of a magnetic system, the magnetization)
(iii) the range of the interactions

These define a system's 'universality class'. If the critical exponents can be determined for any member of the universality class then they are determined for all members of that class.

APPENDIX D: CRITICAL NEUTRON SCATTERING

D.1 The Scattering Function

The scattering function, $S(\vec{q},\omega)$, is given by

$$S(\vec{q},\omega) = \frac{1}{\pi}\frac{\hbar}{(g\mu_B)^2}\sum_\alpha (1-\hat{Q}_\alpha^2)\frac{1}{(1-e^{-\beta\hbar\omega})}\chi''_\alpha(\vec{q},\omega) \qquad [D.1]$$

In the paramagnetic phase where there is no distinction between transverse and longitudinal susceptibility, this reduces to

$$S(\vec{q},\omega) = \frac{2}{\pi}\frac{\hbar}{(g\mu_B)^2}\frac{1}{(1-e^{-\beta\hbar\omega})}\chi''(\vec{q},\omega) \qquad [D.2]$$

Near T_c, it is expected that the inelastic spectrum will consist of low energy fluctuations which satisfy $h\omega \ll kT$. In this limit the detailed balance factor can be expanded in $h\omega/kT$, and to first order

$$S(\vec{q},\omega) = \frac{2}{\pi}\frac{1}{(g\mu_B)^2}kT\,\frac{\chi''(\vec{q},\omega)}{\omega} \qquad [D.3]$$

In a two-axis neutron scattering measurement the relevant function is $S(\vec{q})$ where

$$S(\vec{q}) = \int d\omega\, S(\vec{q},\omega) \qquad [D.4]$$

According to the Kramers-Kronig relation which relates the real and imaginary parts of the susceptibility

$$\chi(\vec{q}) = \frac{1}{\pi}\int d\omega\,\frac{\chi''(\vec{q},\omega)}{\omega} \qquad [D.5]$$

so that $S(\vec{q})$ may be rewritten as

$$S(\vec{q}) = \frac{2}{(g\mu_B)^2}kT\,\chi(\vec{q}) \qquad [D.6]$$

It is convenient to rewrite $S(\vec{q})$ in the form

$$S(\vec{q}) = \frac{2}{3} S(S+1) \frac{\chi(\vec{q})}{\chi_0} \qquad [D.7]$$

where χ_0 is the susceptibility of the non-interacting system, defined by

$$\chi_0 = \frac{(g\mu_B)^2 \, S(S+1)}{3kT} \qquad [D.8]$$

The form of $\chi(\vec{q})$ in the critical regime was first formulated, in the context of magnetic scattering, by Van Hove (1954). He adopted the Ornstein-Zernike description of the real space correlations, assuming that near the critical temperature, the (real space) static spin correlation function decays over some characteristic (inverse) length scale κ_1, as

$$\langle \vec{S}_0 \cdot \vec{S}_r \rangle \propto \frac{e^{-\kappa_1 r}}{r} \qquad [D.9]$$

He further assumed that the equation governing the decay of the time correlation of the magnetization could be treated by diffusion theory, leading to a form for the dynamic correlation function

$$\langle \vec{S}_q(0) \cdot \vec{S}_q(t) \rangle \propto e^{-\Gamma(q)t} \qquad [D.10]$$

The exponential variation of the correlation function in real space and time lead to Lorentzian dependences in the Fourier transformed function and thus to the Van Hove form of $S(\vec{q},\omega)$ where S is the spin of the ion, and r_1 is the temperature dependent range parameter which, from Eq. [D.7], can be defined by

$$\frac{\chi_{q=0}}{\chi_0} = \frac{1}{r_1^2 \kappa_1^2} \qquad [D.12]$$

The function $\Gamma(\vec{q})$ is the wave-vector dependent dynamic width which for a Heisenberg ferromagnet, varies as

$$\Gamma(q) = \Lambda q^2 \qquad [D.13]$$

where Λ is the (temperature dependent) diffusion constant.

D.2 The Quasi Elastic Approximation

The two-axis technique measures $S(\vec{q})$ only approximately. The difficulty is that, in the two-axis geometry, $\vec{q}$ and ω cannot be determined independently. If the nominal wave vector of the measurement is $\vec{q}_0$, then a neutron scattered elastically, (ω=0), will have wave vector $\vec{q}_0$. However a scattered neutron with finite energy, $\Delta\omega$, has a wave vector $\vec{q}_0 + \Delta\vec{q}$. Rather than integrating $S(\vec{q},\omega)$ at constant $\vec{q}$, the two-axis measurement performs the integration along some path in $\vec{q}$ and $\vec{\omega}$ at constant scattering angle, ϕ.

Strictly speaking, $S(\vec{q}) = S(\phi)$ only in the limit where the scattering is completely elastic. However, it is clear that if the scattering is quasi-elastic with some very small energy width, then $\Delta\omega$ is never far from ω=0, and q never far from $\vec{q}_0$. $S(\phi)$ is than a good measure of $S(\vec{q})$ if this quasi-elastic approximation is valid. This is expected to be the case near to a phase transition because of critical slowing down.

It is trivial to show that the spread in the scattered neutron energy, $\Delta E'$, is related to the spread in (the magnitude of) the scattered neutron wave vector, $\Delta k'$, by

$$\Delta k' = \frac{1}{\hbar} \sqrt{\frac{m}{2E'}}\, \Delta E' \qquad [D.14]$$

E' is determined by the energy scale of the fluctuations near the phase transition but the spread in wave vector can be restricted by choosing $E' \gg \Delta E'$.

If the energy dependence of the scattering function is known, it is possible to include a correction for the inelasticity. The correction factor, $C(\vec{q})$, is defined as the ratio of of the energy integral of $S(\vec{q},\omega)$ at constant, ϕ, to the energy integral at constant $\vec{q}$, i.e.

$$C(\vec{q}_o) = \frac{\int_{k'} d\omega\, S(\vec{q},\omega)}{S(\vec{q}_o)} \qquad [D.15]$$

The measured intensity at $\vec{q}_0$, $I(\vec{q}_0)$, is than given by

$$I(\vec{q}_o) = C(\vec{q}_o)\, S(\vec{q}_o) \qquad [D.16]$$